

Fabrication and Physics of CdTe Devices by Sputtering

Annual Technical Report for the Period

March 1, 2005 to May 31, 2006

(Deliverable D.1.7)

Contract No. RXL-5-44205-01

Alvin Compaan, principal investigator

Victor Karpov, co-principal investigator

Robert Collins, co-principal investigator

Dean Giolando, co-investigator

NREL technical monitor: Ken Zweibel

Department of Physics and Astronomy

The University of Toledo

Toledo, OH 43606

Summary

There are three focus areas in this subcontract: understanding key aspects of CdTe device physics, increasing the deposition rate of CdTe magnetron sputtering, and investigating the limits of reducing the thickness of CdTe layers to below 0.5 microns, with special focus on voltage and fill factor.

Our efforts on device physics have primarily involved modeling of CdS/CdTe based PV junctions, modeling and verification of device shunting instability, observation and studying the nature of spatial and temporal fluctuations of micro (AFM) currents through CdTe junctions, further studying of piezo-PV coupling, XAFS XES structural chemistry study of CdCl₂ treated CdS films, spectral ellipsometry study of surface morphology in the course of structure growth, as well as etching, film structure and device parameters vs. magnetron deposition rate, and device parameters for CdTe thickness below 1 micron. During the first year of this award, we have

- Developed numerical and analytical (field reversal) models explaining all the major facts pertaining to CdTe/CdS device operations,
- Developed a quantitative description of shunting instability in thin film PV through the mechanism of dielectric breakdown and verified it experimentally,
- Experimentally observed gigantic spatial and temporal fluctuations of micro AFM current and proposed their interpretation based on defect motility in CdTe films,
- Developed a new (bending) technique of piezo-PV characterization and observed increase in the open circuit voltage of devices on flexible substrates subject to certain bending; also, observed the piezo-PV coupling in CIGS based materials,
- Through XAFS and XES techniques, established the nature of Cu binding in CdS (primarily with S atoms), and effect of substantial compression of certain atomic bonds upon Cu diffusion in CdS,
- Established that increase in the magnetron deposition rate by the factor of 2.5 does not hamper the cell performance when the postdeposition treatment is properly optimized

- Experimentally established the relationship between the CdTe film thickness and device efficiency in the range of 2.5 - 0.45 micron, in particular demonstrated high efficiency devices of thickness below 1 micron.

Table of Contents

Summary	i
List of Figures	v
List of Tables	viii
1 Introduction	1
1.1 Background	1
1.2 Objectives of this subcontract	1
1.3 Technical approach	2
2 Key Aspects of CdTe Device Physics	3
2.1 Overview	3
2.2 Physical model of CdS-based thin-film photovoltaic junctions	3
2.3 Thin-film Shunting Breakdown	10
2.3.1 Introduction	10
2.3.2 Dielectric breakdown in thin films	10
2.3.3 Dielectric breakdown in thin film PV	17
2.3.4 Conclusions	19
2.4 Spatial and Temporal Current Fluctuations in Polycrystalline Schottky Barriers	19
2.4.1 Introduction	19
2.4.2 Experimental Results for MSM structures	20
2.4.3 Theoretical Interpretation	27
2.4.4 Fitting the data	34
2.4.5 Temporal fluctuations	35
2.4.6 Conclusion	36
2.5 Piezo-photovoltaic effect in thin-film CdS-based solar cells	37
2.5.1 Introduction	37
2.5.2 Experimental	38
2.5.3 Results and discussion	40
2.5.4 Conclusions	43
2.6 Synchrotron X-ray Absorption Fine Structure (XAFS) and X-ray Emission Spectroscopy (XES) Studies on Copper-diffused CdS	45

References (Section 2)	51
3 Deposition rate of CdTe magnetron sputtering	56
3.1 Overview	56
3.2 Deposition rate vs. sputtering gas pressure	56
3.3 Conclusions	60
4 Thin CdTe devices	61
4.1 Overview	61
4.2 Device fabrication and J-V analysis	61
4.3 SEM studies of CdTe devices with varying absorber thickness	64
References (Section 4)	65
5 Real Time Spectroscopic Ellipsometry (RTSE) of CdTe Materials and Solar Cells	67
5.1 Overview	67
5.2 Experimental Details	69
5.3 Results and Discussion: RTSE Studies of CdTe Deposition	69
5.4 Results and Discussion: RTSE Studies Comparing CdS and CdTe Deposition	86
5.5 Results and Discussion: Studies of Post-Deposition Treatments	93
5.6 Summary	99
References (Section 5)	104
6 Publications	105
6.1 Refereed papers published or in press (3/1/05 - 5/31/06)	105
6.2 Poster or oral presentations published on CDROM and the NREL Web site	106
7 Project personnel	108
7.1 Research professors	108
7.2 Postdoctoral Associate	108
7.3 Graduate Students (with Principal Advisor)	108
7.4 Technical Assistants	109

List of Figures

2.1	AMPS generated light and dark J-V characteristics for two different	4
2.2	Phenomenological model of CdS based thin-film PV	6
2.3	AMPS simulated (a) vs. analytical (b) J-V characteristics for the same . . .	9
2.4	(a) Sketch of a MOS field transistor structure	11
2.5	Free energy of the dielectric with a local N-defect	12
2.6	Sketch of a defect shunting pathway and its equivalent	18
2.7	Variations in I-V characteristics across the sample	20
2.8	Macro (a) and micro (b) I-V curves for a thickest	22
2.9	Same as in Fig. 2.8 for a thinnest structure	22
2.10	Temporal current fluctuations for the case of AFM (a)	23
2.11	Current-voltage characteristics of Cr-CdTe-Cr structure	24
2.12	Sketch of the physical structure (a) and band diagrams	25
2.13	(a) The macroscopic current-voltage characteristic for a finished	26
2.14	A fan of 'abnormal' spot micro I-V curves	27
2.15	Sketch of the electric field distribution and corresponding	29
2.16	Sketch of hole hopping transport through two barriers	30
2.17	Different cases of defect assisted tunneling	32
2.18	Theoretical fits of the measured current-voltage	35
2.19	Modulus of rupture (MOR) type of bending set-up	39
2.20	Bending setup for solar cells on flexible molybdenum substrates.	39
2.21	Changes in V_{oc} and J_{sc} as a function of stress in CdS film	41
2.22	J-V curves for a cell on glass measured with increasing pressure	41
2.23	Changes in V_{oc} as a function of applied pressure	42
2.24	Changes in J_{sc} as a function of applied pressure	43
2.25	J-V curves for a flexible cell showing decreasing PV parameters	44
2.26	Qualitative analysis on $\chi(R)$ of Cu-diffused as-grown CdS film	46
2.27	Qualitative analysis on $\chi(R)$ of Cu-diffused, chloride-treated CdS film	46
2.28	Theoretical FEFF fitting to the $\chi(R)$ functions of the copper-diffused	48
2.29	a) Sulfur $L_{2,3}$ XES spectra of CdS reference, $CdCl_2$ treated CdS	49
2.30	Atomic structure of hexagonal CdS, space group	50

3.31	Nucleation and growth kinetics for CdTe films grown at different pressures.	56
3.32	Average CdTe deposition rate and the corresponding highest	57
3.33	In-plane AFM images and corresponding cross sections	58
3.34	Transmittance of CdTe films grown at different pressures.	60
3.35	Film thickness map measured by DEKTAK profilometer.	61
4.36	Line of sight transmission data of samples (Tec7/CdS/CdTe)	63
4.37	Graphical representation of the J-V parameters for the best cells.	65
4.38	SEM micrographs of Tec7/CdS/CdTe surface before and after	66
5.39	Schematic of deposition system and associated instrumentation	70
5.40	Evolution of the surface roughness layer thickness versus the bulk	71
5.41	The nucleation and coalescence stages of CdTe deposition	72
5.42	Parameters that describe the clustering in the initial stages of CdTe	73
5.43	Surface roughness layer thickness at the end of CdTe film deposition	74
5.44	Stepwise depth profiles in the relative void volume fraction for five	76
5.45	Optical model used to simulate the film structure for the CdTe film	77
5.46	Effective deposition rate as a function of deposition temperature	78
5.47	Deposition rate versus time obtained by two different ways	79
5.48	The room temperature dielectric functions of single crystal CdTe	80
5.49	The room temperature dielectric functions of single crystal CdTe	81
5.50	Substrate temperature calibration obtained by measuring the shifts	82
5.51	Second derivative of the dielectric functions for the CdTe film	83
5.52	The E_0 critical point energy plotted as a function of true temperature	84
5.53	Room temperature (15°C) E_0 band gap for CdTe films obtained	85
5.54	Room temperature dielectric functions of CdTe films deposited on c-Si	86
5.55	Resonance energies E_n (upper) and widths Γ_n (lower)	87
5.56	Surface roughness layer thickness versus bulk layer thickness	89
5.57	Surface roughness layer thickness at the end of the deposition	90
5.58	Step-wise depth profile in the void volume fraction for a CdS film	91
5.59	Relative void volume fraction variations with substrate temperature	92
5.60	Room temperature dielectric functions of magnetron sputtered CdS	93
5.61	Room temperature dielectric functions ϵ of magnetron sputtered CdS	94
5.62	Room temperature dielectric functions of magnetron sputtered CdS	95

5.63	Room temperature dielectric functions ε of magnetron sputtered CdS	96
5.64	Step-wise depth profile in the width of the band gap critical point	97
5.65	Best fit analytical models of the room temperature dielectric	98
5.66	Critical point energies (top) and widths (bottom) as functions of CdTe . . .	99
5.67	Relative void volume fractions as functions of CdTe bulk layer	100
5.68	Best fit analytical models to the room temperature dielectric	101

List of Tables

2.1	Theoretical FEFF fitting parameters to the CdS with and without prior chloride treatment. Note: $dR = R_{fit} - R_{ref}$ is the path-lengths shift relative to the reference.	47
3.2	Average CdTe deposition rate and corresponding highest cell efficiency at different pressures.	57
4.3	Variation in post-deposition treatment parameters for devices of varying CdTe thickness. Numbers in the parenthesis in the first column are the sample ID's. Less Cu was used with thinner CdTe, but fluctuations occurred due to slow response of evaporator boat temperature.	62
4.4	Average J-V parameters for devices with different CdTe layer thickness. . . .	63
4.5	Best cell performance for each CdTe thickness.	64
4.6	Grain size distribution for samples with different thickness of CdTe before and after CdCl ₂ treatment.	66

1. INTRODUCTION

1.1. Background

The purpose of this subcontract, as part of the R&D Partners, Solar Cell Optimizer Category is to 1) understand the mechanisms driving CdTe device performance and degradation; 2) experiment with raising the deposition rate of sputtered CdTe to make it more attractive economically; 3) investigate the limits of thickness reduction of CdTe using sputtering to reduce Te shortage issues and add to the economic attractiveness of the sputtering method; and 4) to support workforce development through the education and training of undergraduate, graduate, and postdoctoral students in the PV area.

This annual report covers the first year NREL thin-film partnership subcontract with the University of Toledo which has three task areas: 1) understanding key aspects of CdTe device physics, 2) increasing the deposition rate of CdTe magnetron sputtering, 3) investigation of the limits of reducing the thickness of CdTe layers to below 0.5 microns, with special focus on voltage and fill factor.

1.2. Objectives of this subcontract

The primary objectives of this research by this subcontractor as an R&D partner is to address fundamental issues especially related to:

- enhancing the total-area, thin-film cell efficiency through magnetron sputtering,
- improving the understanding of nonuniformities and their impact on device and module performance through novel experiments and modeling,
- improving the understanding of the materials and devices through the use of photoluminescence (PL), Hall, Raman, absorption, scanning electron microscopy (SEM) with energy dispersive x-ray spectroscopy (EDS), and X-ray absorption fine structure (XAFS),
- identifying materials and structural issues that can lead to improved cell stability, including buffer and interfacial layers and novel back contacts,

- identifying novel device structures to find pathways for reducing the utilization of CdTe, and
- strengthening the thin-film PV infrastructure through education and training of undergraduate and graduate students as well as postdoctoral associates.

1.3. Technical approach

The scope of work under this subcontract is divided into three primary efforts which are reflected in the three following Sections. The first effort is focused on the understanding of the key aspects of CdTe device physics. The second effort is focused on increasing the deposition rate of CdTe magnetron sputtering. We seek to find a range of rf sputtering deposition parameters which allow faster device fabrication without sacrificing the performance. The third effort is focused on the thinning down the absorber and investigation of the limits of reducing the thickness of CdTe layers to below 0.5 microns, with special focus on voltage and fill factor.

2. KEY ASPECTS OF CDTE DEVICE PHYSICS

2.1. Overview

The empirical approach of trial and error is not suitable anymore for achievement higher device efficiency and improved stability, as it requires very tedious and time-consuming experiments. Understanding the main physical principles governing CdTe/CdS solar cells becomes increasingly important in order to focus fabrication activities in potentially promising directions.

Our CdTe device physics effort is mainly devoted to development of a simple physical model of CdS-based thin-film photovoltaic junctions, including the major types that utilize the CdTe and Cu(In,Ga)Se₂ absorber layers.

The thin-film physics aspects of CdTe based devices led us to the introduction of a new type of phase transition in thin films under external or built-in electric field. In the course of transition, the electrostatic energy ($\propto E^2$) discharges into structural defects. This may lead to the dielectric film breakdown or Schottky barrier suppression in semiconductor film junctions.

We also concentrate on studying a flow of electric current through metal-semiconductor junctions of a type used in thin-film PV for back contacts. To concentrate on one type of junction, we have used the symmetric metal-semiconductor-metal (MSM) structures of rf-sputtered CdTe layer sandwiched between two metal contacts (either Cr or Ni). Along with the conventional measurements, the current-sensing contact mode AFM was employed to measure the current-voltage characteristics and temporal current variations under fixed voltage.

In addition we discuss new results on piezo-photovoltaic coupling in CdS-based thin film devices.

In what follows we describe our latest findings not covered in this year's quarterly reports.

2.2. Physical model of CdS-based thin-film photovoltaic junctions

The technology of polycrystalline thin-film photovoltaics (PV) has reached a degree of maturity allowing its industrial scale-up and market development.^{1,2} However, understanding of these device operations remains insufficient and lacks explanations of many important

facts. For example, two major types of thin-film PV based on CdTe and Cu(In,Ga)Se₂ (CIGS) absorbers, use a thin layer of CdS, whose role remains puzzling. In particular, it causes a substantial blue light absorption ($\hbar\omega > 2.4$ eV) without any contribution to the carrier collection. This contradiction, while commonly recognized, does not have a good explanation. Several other controversial observations are listed below. This lack of physical understanding leaves the technology with rather inefficient trial-and-error approaches.

Here we present a physical model that at least semi-quantitatively explains all the significant facts related to CdS-based thin-film PV, allows for a closed analytical solution (verified numerically), and predicts different possibilities in device manufacturing.

As a brief introduction, we note that the prevailing model of CdS-based PV has been a p-n junction with CdS layer as the n-type component. The model parameters include layer thicknesses, band offsets (between CdS, CdTe, and contact metals), doping concentrations, and some others specified by the existing software packages, such as AMPS.^{3,4} The current-voltage (J-V) curve fitting is considered a major test for this type of modeling.

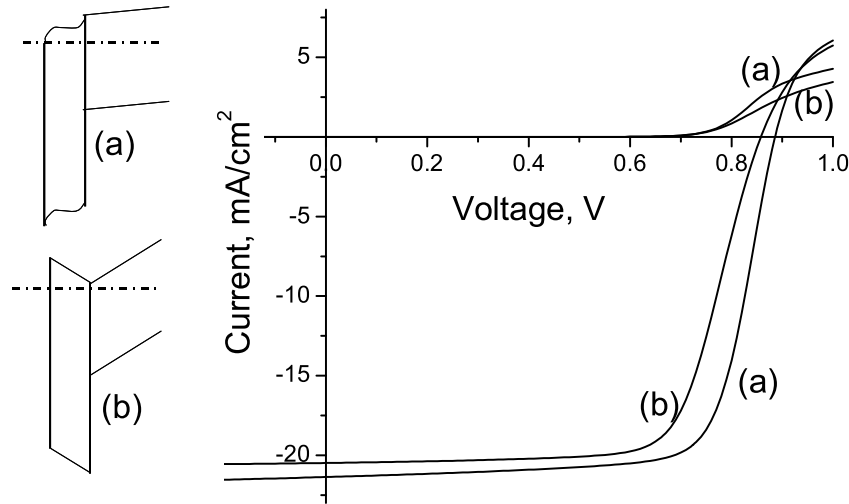


Figure 2.1: AMPS generated light and dark J-V characteristics for two different device models: the standard p-n junction (a), and model presented in this work (b). For case (a) we used the device parameters suggested in Ref. 3 including the back barrier, but without the buffer layer and deep defects in CdS. For the case (b) the reversed electric field was additionally introduced by creating two heavily doped (10^{18} cm⁻³) interfacial layers and decreasing the carrier concentration in CdS to $2 \cdot 10^{16}$ cm⁻³.

However JV modeling as such appears not conclusive enough, since reasonable fits can be obtained with different models (Fig. 2.1). This is not surprising: the diode-type JVs naturally occur with any barrier dominated electron transport. As a result different structures with multiple fitting parameters (and often with more than one barrier) can provide comparable fits. Other indicative observations are needed to verify the device model.

A list of such indicative observations below limits model choice to that of Fig. 2.2. (1) The pressure dependent PV performance attributable to the piezo parameters of CdS⁵ suggests a strong electric field in the depleted CdS layer. The energetically favorable CdS electric dipole orientation requires that this field be opposing the average device field. (2) The 'reach-through' band bending in CdTe caused by a buffer layer on the other side of CdS^{6,7} suggests the metal-insulator-semiconductor (MIS) nature of the device with an insulating CdS. (3) Pointing at the same is that using more conductive CdS does not improve the device. To the contrary, a rather insulating chemical bath deposited CdS is used in high quality PV.² (4) Buffer layers of certain morphology (for example, sputtered) strongly increase the device open-circuit voltage (V_{oc}) while other chemically and electrically equivalent layers (such as chemical vapor deposited) do not cause this effect.^{6,7} This points at the role of interfacial morphology and possibly its related internal stress acting through the piezo-effect.⁵ (5) Absence of carrier collection from CdS² may suggest the electric field reversal in CdS relative to that in CdTe or CIGS layers (consistent with the above item (1)); (6) Pointing at the same is the negative quantum efficiency, $QE < 0$ observed under the blue illumination for devices with thick CdS.⁸ (7) Light and dark JV crossover pointing at CdS related photoconductivity,⁹ and light JV rollover in the fourth quadrant.²

The diagram in Fig. 2.2 is consistent with all of the above observations. Its unique feature is the electric field reversal and "gull wing" singularity in the conduction band implying positive interfacial charges (due to the piezo-effect or defect states, or both). Following Ref. 3 we do not assume any significant band offset between the CdS and its tangent layers; however, adding a moderate offset does not change the model predictions. Also, we do not specify the band bending curvature; the depletion widths remain arbitrary within the requirement that they are greater than the corresponding layer thicknesses. Unlike the examples in Fig. 2.1, our model neglects the back field effects (rightmost part of the diagram).

In this framework, the lack of carrier collection from CdS is due to the field reversal, and

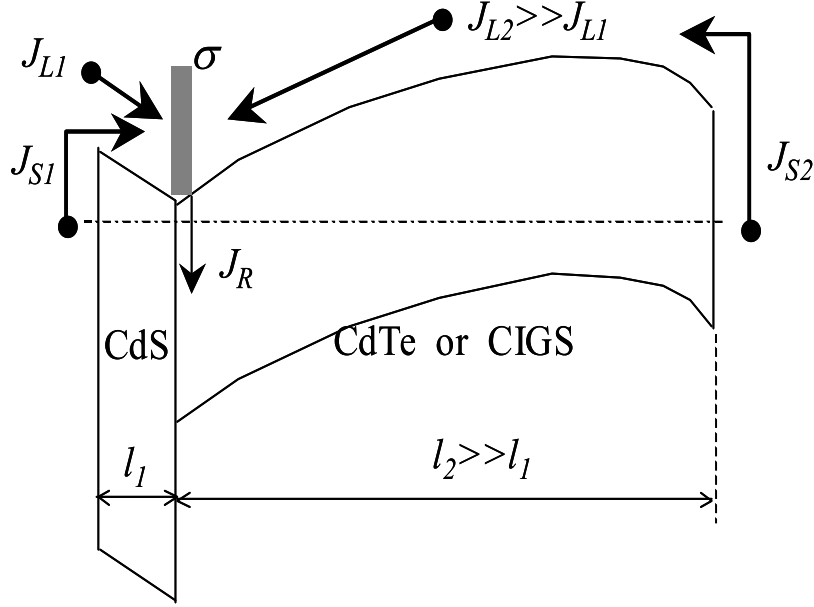


Figure 2.2: Phenomenological model of CdS based thin-film PV. σ represents the two-dimensional electron charge density. J_{L1} , J_{L2} are the component 1 and 2 photocurrents, J_{s1} and J_{s2} are the corresponding saturation currents. J_R is the recombination current.

the corresponding barrier in Fig. 2.2 is consistent with the CdS depletion.¹⁰ Under illumination or forward bias, the electrons accumulated in the "gull wing" region will generate the electric field, flattening the singularity and suppressing the barrier. Hence, the electric current increase leading to the dark and light JV crossing, qualitatively similar to the CdS photoconductivity. On the other hand, the CdS barrier will limit forward current causing J(V) flattening (rollover) in the forward bias region.

The model of Fig. 2.2 allows for a closed form analytical solution. In addition to the parameters presented in Fig. 2.2, we introduce the layer dielectric permittivities (ϵ_1 and ϵ_2), the electron potential barriers (V_{B1} and V_{B2}) measured from the conduction band singularity to the maximum electron energy in the layer 1 and 2 respectively, and the barriers (W_1 and W_2), measured from the contact Fermi energy to the same maximum; hence the saturation currents, $J_{s1(2)} = J_{s1(2)}^0 \exp(-W_{1(2)}/kT)$. Each of the two components is described by its standard diode characteristic $J_{1(2)} = J_{s1(2)}[\exp(qV_{1(2)}/kT) - 1] - J_{L1(2)}$ with the open circuit

voltage¹¹

$$V_{oc1(2)} = \frac{kT}{q} \ln \left(1 + J_{L1(2)}/J_{s1(2)} \right) \quad (2.1)$$

The CdS barrier is relatively low, $W_1 \ll W_2$ and $J_{s1} \gg J_{s2}$. The photocurrent ratio can be estimated as $J_{L1}/J_{L2} \sim 0.15$ for a thick (up to 0.2 micron) CdS and is smaller for thin CdS.

The electric current continuity requires that $J = J_1(V_1) = J_2(V_2) + J_R$ where J_R is the recombination current, V_1 and V_2 are the electric potential differences across the layers, $V_1 + V_2 = V$. The electric potential distribution is found from the electrostatic problem, which simplifies because the electron density is exponentially high in the proximity of "gull wing" singularity and can be approximated by a self-consistent two-dimensional charge density σ ; hence, the electric potential linear in coordinate. In this approximation, $J_R = \gamma\sigma$ where γ accounts for the interfacial defect properties. The equilibrium value $\sigma = \sigma_0$ remains the model parameter.

The problem is further simplified by noting that the recombination is relatively inefficient in device quality structures (say, $J_R \lesssim 0.1J_{L2}$) and can be treated as perturbation. Namely, σ will be found neglecting the recombination and then substituted into $J_R = \gamma\sigma$.

The partial currents can be written in the form

$$J_{1(2)} = \pm J_{s1(2)} \left[1 - \frac{\sigma}{\sigma_0} \exp \left(-\frac{\Delta V_{B1(2)}}{kT} \right) \right] \pm J_{L1(2)}, \quad (2.2)$$

with (+) corresponding to the component 1. The barrier change is expressed through the standard electrostatics,

$$\Delta V_{B1(2)} = \pm \frac{Vl}{l_{2(1)}} - \frac{4\pi\sigma ql}{\epsilon}, \quad \epsilon = \frac{\epsilon_1\epsilon_2}{\epsilon_1 + \epsilon_2}, \quad l = \frac{l_1l_2}{l_1 + l_2}. \quad (2.3)$$

Substituting this into $J_1 = J_2$ determines the electron charge density σ ,

$$\begin{aligned} \frac{\sigma}{\sigma_0} \exp \left(4\pi q \frac{\sigma l}{kT\epsilon} \right) = \\ \frac{J_{s1} + J_{s2} + J_{L1} + J_{L2}}{J_{s2} \exp(qVl/kTl_1) + J_{s1} \exp(-qVl/kTl_2)}. \end{aligned} \quad (2.4)$$

Substituting Eqs. (2.3) and (2.4) into Eq. (2.2) yields the integral J-V characteristics

$$J = J_{s1} + J_{L1} - \frac{J_{s1} + J_{s2} + J_{L1} + J_{L2}}{1 + (J_{s2}/J_{s1}) \exp(qV/kT)} - J_R \quad (2.5)$$

with $J_R = \gamma\sigma$ and σ from Eq. (2.4). The characteristic in Eq. (2.5) is mathematically quite different from that of the standard diode leading to a number of predictions, which we list in the approximation $J_R = 0$ next.

The system open circuit voltage and short-circuit current are

$$V_{oc} = V_{oc2} - V_{oc1} \quad \text{and} \quad J_{sc} = \frac{J_{L2}J_{s1} - J_{L1}J_{s2}}{J_{s1} + J_{s2}}. \quad (2.6)$$

Because $J_{s2}/J_{s1} \ll 1$, the lack of carrier collection from CdS is predicted ($J_{sc} \approx J_{L2}$). On the other hand, for a blue light illumination fully absorbed in CdS ($J_{L2} = 0$) we predict $J_{sc} = -J_{L1}$, hence QE < 0.

The dark to light J-V crossing takes place at

$$V_X = V_{oc} + \frac{kT}{q} \left[\exp\left(-\frac{qV_{oc1}}{kT}\right) + \exp\left(-\frac{qV_{oc2}}{kT}\right) \right], \quad (2.7)$$

slightly above V_{oc} , consistent with the observations. In addition, Eq. (2.5) predicts a JV rollover more profound at low temperatures, which is indeed many times observed and attributed mostly to the back contact effects¹².

The slopes dV/dJ at $V = 0$ and $V = V_{oc}$ give the short-circuit ('shunt') and open-circuit ('series') resistances

$$R_{sc} = \frac{kT}{q} \frac{(\sqrt{J_{s2}/J_{s1}} + \sqrt{J_{s1}/J_{s2}})^2}{J_{s1} + J_{s2} + J_{L1} + J_{L2}}, \quad (2.8)$$

$$R_{oc} = \frac{kT}{q} \frac{J_{s1} + J_{s2} + J_{L1} + J_{L2}}{(J_{s1} + J_{L1})(J_{s2} + J_{L2})}. \quad (2.9)$$

Assuming, for example, the typical² $J_{L1} \sim 0.1J_{L2} \sim 2 \text{ mA/cm}^2$ and $J_{s2} \ll J_{s1} \lesssim J_{L1}$ yields $R_{oc} \approx (kT)/(qJ_{L1}) \sim 10\Omega$, in the ballpark of the observed series resistances for CIGS¹³ and CdTe¹⁴ based PV. This estimate changes when the alternative inequality $J_{L1} \ll J_{s1}$ takes place. In addition, the measured resistances can be affected by factors beyond the present model, such as the back field¹² and nonuniformity¹⁵. Defect assisted tunneling (hopping) transport through the CdS barrier would also have a noticeable effect on the above predictions. Nevertheless, Eqs. (2.5) - (2.8) call upon experimental verifications including the temperature, light intensity and spectral dependencies.

Consider briefly the recombination effects. Eq. (2.4) predicts that σ and thus J_R is a maximum at

$$V_R = \frac{kT}{q} \ln\left(\frac{J_{s1}l_1}{J_{s2}l_2}\right) \approx V_{oc} - \frac{kT}{q} \ln\left(\frac{J_{L2}l_2}{J_{L1}l_1}\right). \quad (2.10)$$

Assuming the typical $J_{L1}l_1/J_{L2}l_2 \lesssim 0.01$, one can estimate $V_R \approx V_{oc} - 0.06 \text{ eV}$. For realistic $l_1/l_2 \lesssim 0.1$, it follows from Eq. (2.4) that $J(R)$ drops sharply when $V > V_R$, while it decreases rather slowly for $V < V_R$. In other words, the recombination has almost no effect on J-V curve when $V > V_R$, while it decreases $|J|$ almost uniformly when $V < V_R$.

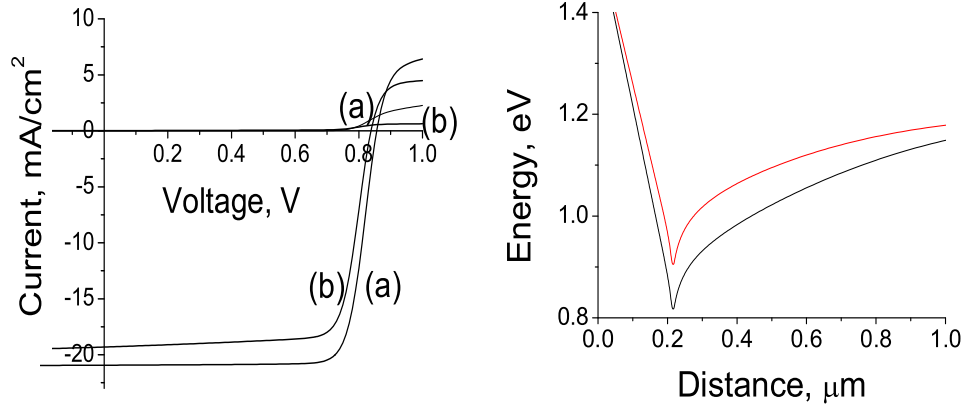


Figure 2.3: Left: AMPS simulated (a) vs. analytical (b) J-V characteristics for the same band diagram. Right: The proximity of conduction band singularity simulated by AMPS for the forward bias of 1 V in the dark and 1.5 AM light. [The "cusp" artifact is due to the artificial doped layer]. In this modeling the back barrier effects and recombination were eliminated; hence, JV crossing and rollover are due to the CdS barrier. Nevertheless, the device parameters $V_{oc} = 0.81$ eV, $J_{sc} = 20$ mA/cm², fill factor of 72%, and efficiency 12.8% appear realistic for CdTe PV.

We verified our findings with numerical AMPS simulations. Two artificial narrow layers (10% of CdS thickness) containing high concentrations (10^{18} cm⁻³) of shallow donors and acceptors were added on the opposite sides of the original CdS to model the built-in reversal electric field in CdS. In the spirit of this model, we did not include the buffer layer, back field, and any recombination centers. As is seen from Fig. 2.3, the analytical and numerically simulated curves are reasonably close. The observed deviations appear legitimate, since our analytical result does not account for the carrier diffusion.

Overall, our model emphasizes interfacial properties, such as the interfacial morphology, related compression, and charges. In the terms of practical implications, they can be altered by tuning the deposition regimes, creating doping-induced stresses, and applying proper interfacial treatments (layers).

In conclusion, we have proposed a physical model that explains a variety of facts for CdS based photovoltaics. This model is solved analytically. The predicted properties differ considerably from that of the standard p-n junction and call upon further experimental

verifications.

2.3. Thin-film Shunting Breakdown

2.3.1. Introduction

Modern thin-film devices, such as PV junctions and MOS transistors operate under substantial electric field E , either external or built-in. This section introduces a new phase transition scenario where the stored field energy $E^2\epsilon/8\pi$ discharges into defects thus turning the system into a lower field phase; we call this E^2 phase transition. Three more specific phenomena are related to it. One is the well known dielectric breakdown, of great practical significance for ultrathin oxides of integrated circuits.^{16–19} Two others are field induced compensation of semiconductors and Schottky barrier suppression in thin-film junctions.

Starting from seminal work,^{20,21} a variety of field-induced structural transformation phenomena has been observed including electrical switching and dielectric breakdown, field-induced doping²² and crystallization,²³ writing micro-structures with STM and SEM tips,^{24,25} and metastable shunt formation.²⁶ In spite of a longstanding phase transition folklore, no framework has been established to relate those phenomena to the standard phase transition theory. Here we show that the field-induced structural transformations possess, indeed, the standard first-order phase transition kinetics of either nucleation or spinodal decomposition type.

2.3.2. Dielectric breakdown in thin films

We start with the case of dielectric breakdown in a MOS structure illustrated in Fig. 2.4(a). It is characterized by two length scales, oxide thickness (L) and gate linear size $l \gg L$, in the ranges of respectively nanometers and microns in the modern devices. According to our scenario, the transition develops through a local fluctuation in cross-dielectric ("shunting") resistance. Similar to a capacitor shunt, this lowers the field strength and stored energy. Such a "shunting" path can be related to a local fluctuation in concentration of defects facilitating electron tunnelling through the dielectric shown in Fig. 2.4(b). It is described as a cylinder region of length L and diameter d containing a certain number of defects N .

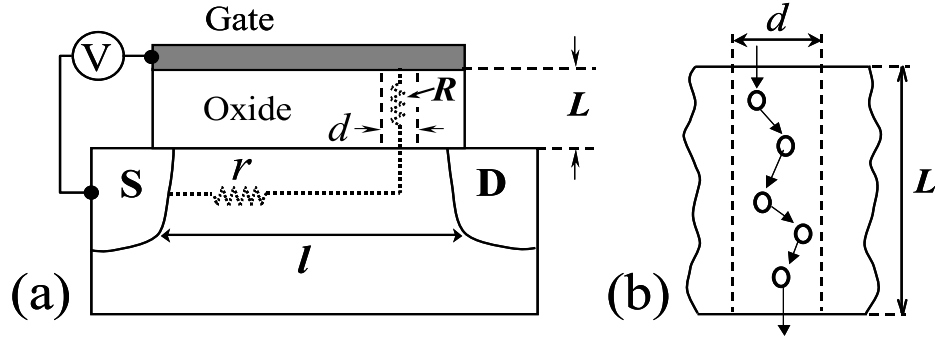


Figure 2.4: (a) Sketch of a MOS field transistor structure (side view) with source (S), drain (D), gate electrode, and a "shunting" path; not to scale. Dotted line resistors represent the equivalent circuit. (b) "Shunting" path provided by N-step defect assisted tunnelling through the oxide layer with $N=4$ defects.

Shunt Nucleation

Following the standard approach, the probability of a shunting path fluctuation is proportional to $\exp(-W_B/kT)$. The minimum work (energy barrier) $W_B = \min[\delta W_E + \delta W_d]$ needed to form the path, compromises between the energy gain δW_E in the stored field energy, and the energy δW_d lost to create the required fluctuation in defect concentration. As specified next, this minimum corresponds to the critical path analogous to the critical embryo in the first-order phase transition theory. To estimate δW_E we note that a local finite resistance R causes a small change $u = Vr/(r + R) \approx Vr/R$ in the electric potential across the dielectric where r is the electrode resistance (for example, the semiconductor resistance between the "shunt" and the source region in Fig 2.4). For a device of area $A \sim l^2$ the corresponding gain in the stored field energy can be estimated as

$$\delta W_E \approx -\frac{ArV^2\epsilon}{8\pi LR} \quad (2.11)$$

to within a numerical multiplier of the order of one that depends on the device geometry. We show next that the gain δW_E can be significant enough to trigger a local structural transformation that lowers R .

For a channel of N defects confined into cylindrical region of diameter $d \ll L$ [Fig 2.4(b)], the effective inter-center distance becomes $L/(N + 1)$. Hence, the tunnelling resistance

$$R = R_0 \exp \left[\frac{2L}{(N + 1)a} \right], \quad (2.12)$$

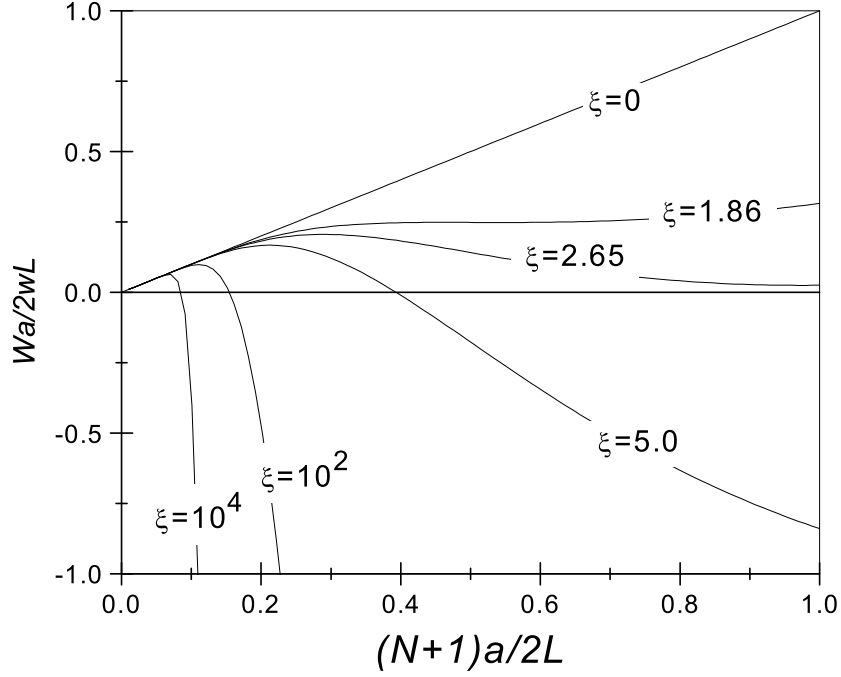


Figure 2.5: Free energy of the dielectric with a local N-defect path for different values of the governing parameter ξ .

where a is the electron localization radius and we assume $L/a \gg 1$. R_0 generally depends on the tunnelling mechanism. It can be roughly estimated as $R_0 \sim U/q^2\nu$, where U (~ 1 eV) is the tunnelling barrier and ν ($\sim 10^{13} \text{ s}^{-1}$) is the preexponential in the the probability of the inter-center tunnelling. A possible dependence $R_0(N)$ can be neglected compared to the much stronger exponential dependence in Eq. (2.12).

The channel cross-section area

$$d^2 \sim La/N \quad (2.13)$$

can be derived from the condition that all the points in that area are within the distance of $(L/N) + a$ from the nearest defect and thus provide comparable probabilities of tunnelling. Indeed, separating two centers by d in the lateral direction increases the inter-center distance by $\Delta = d^2 N/2L$ compared to $L/N \gg d$ for the two neighboring centers at the cylinder axis; Eq. (2.13) follows from $\Delta \sim a$.

From Eqs. (2.11) and (2.12), we observe indeed that δW_E exponentially increases with N and thus it is energetically favorable for the system to generate defects. The opposing trend results from the energy loss $\delta W_d = Nw$ required to create N defects. Adding δW_E and δW_d and introducing the dimensionless variable $x = (N+1)a/2L$ gives the total energy change

$$W(x) = \frac{2Lw}{a} \left[-\xi \exp\left(-\frac{1}{x}\right) + x \right] - w \quad (2.14)$$

with

$$\xi = \frac{AarV^2\varepsilon}{16\pi R_0wL^2} \equiv \left(\frac{V}{V_0} \right)^2. \quad (2.15)$$

This description is restricted to the domain $x \lesssim 1$ where the concept of defect assisted tunnelling remains valid.

$W(x)$ has a shape typical of the first-order phase transitions (Fig. 2.5). A new metastable phase of large N appears when the governing parameter ξ grows through its critical value $\xi_{c1} \approx 1.86$. It becomes stable as ξ further increases above $\xi_{c2} \approx 2.73$. Hence, the breakdown becomes energetically favorable when $V > V_c \equiv \xi_{c2}V_0$.

In terms of the first-order phase transition kinetics, the energy barrier in Fig. 2.5 describes a homogeneous nucleation. For practically important $\xi \gg 1$ (see below) Eq. (2.14) gives the critical embryo barrier

$$W_B \equiv \max[W(x)] = 2Lw/a \ln(\xi \ln \xi). \quad (2.16)$$

The embryo represents a cylindrical region with the number of defects and diameter given respectively by

$$N_B \approx 2L/[a \ln(\xi \ln \xi)] \quad \text{and} \quad d \approx \sqrt{La/N_B}. \quad (2.17)$$

For numerical estimates we use the typical solid state parameters $\varepsilon \sim 10$, $w \sim 1$ eV and $a \sim 3$ Å. Also we put $R_0 \sim \hbar/q^2x \sim 10^3$ KΩ, $r \sim 1$ KΩ, $L/l \sim 10^{-3}$, and $L/a \sim 30$ in the range of modern MOS parameters. This gives $\xi \sim 10^{13}$, $N_B \sim 1$, $W_B \sim 1$ eV, and $d \sim 1$ nm. The estimate of $N_B \sim 1$ falls beyond the domain $N \gg 1$ of the underlying theory applicability. Yet, as an order-of-magnitude guide, it predicts a single defect midway a modern micro MOS capacitor to give rise to a shunting path.

Critical voltage and nucleation time

Based on the above estimates, the characteristic voltage V_0 (and thus the critical voltage V_c) turns out to be surprisingly small,

$$V_0 = \sqrt{\frac{16\pi R_0 w L^2}{a A r \varepsilon}} \sim 3 \cdot 10^{-5} \sqrt{\frac{R_0}{r} \frac{L}{l}} \sim 1 \text{mV}. \quad (2.18)$$

Thus, MOS thin dielectrics are predicted to be thermodynamically unstable under voltages in the microvolt range. The physical nature of such a low instability threshold is that a shunting entity affects a relatively large device area and thus significantly decreases the system energy even when the electric bias is small.

However, because the latter instability is of thermodynamic nature, it takes extremely long time to evolve. The underlying reason is that the transition barriers $W_B \equiv \max[W(x)] \approx 0.25(2wL/a)$ corresponding to low voltages are high (see Fig. 2.5). Indeed, given the typical $w/kT \gtrsim 30$, and $L/a \gtrsim 10$, it follows that $W_B/kT \gtrsim 100$ where kT is the thermal energy. This gives the transition time

$$t_{BD} \sim \nu^{-1} \exp(W_B/kT) \quad (2.19)$$

that exceeds any conceivable experimental time.

On the other hand, the observed breakdown voltages are in the range of $V \gg V_0$. They correspond to very large $\xi \gg 1$ (say, $V \gtrsim 1 \text{ V}$, $\xi \sim 10^{13}$), low transition barriers in Eq. (2.16), and the time to breakdown short enough to fit the data. For example, substituting $\xi \sim 10^{13}$ and $2Lw/akT \sim 10^3$ gives $t_{BD} \sim 1 \text{ s}$.

The characteristic defect generation time is typically much longer than the experimental time over which the external bias grows from zero to a finite value. Hence, the electric field appears as a sudden perturbation and the system finds itself in a metastable state (similar, for example, to an overheated liquid). Its stable state is reached through the critical embryo nucleation, which in the diagram of Fig. 2.5 can be viewed as stochastic oscillations on the left-hand side of the barrier $W(x)$ where each move corresponds to a single defect creation or annihilation. This predicts oscillations in the pre-breakdown tunnelling current V/R where R is described in Eq. (2.12). The oscillations are expected to be especially strong in the proximity of the barrier maximum where the dependence $W(x)$ flattens out.

Following nucleation is the embryo growth stage, which, in Fig. 2.5, corresponds to a trajectory descending along the right-hand-side of the barrier $W(x)$. This later stage kinetics can be quite complex including acceleration due to Joule heat liberation, thermally

activated hopping between the defects, contributions from hot electrons coming from the metal, etc. These features fall beyond the present framework limited to introducing the concept of breakdown as a phase transition and describing its nucleation stage.

Heterogeneous shunt nucleation

In reality, heterogeneous nucleation of conductive paths can dominate the breakdown kinetics in non-crystalline thin-film dielectrics. This brings about nucleation features characteristic of random systems.³⁰ A simplified description below accounts for fluctuations in the preexisting defect concentration.

Fluctuation δN in the number of preexisting defects reduces the nucleation barrier by $w\delta N$. The "optimum" conductive path combines a finite probability $p(\delta N) \equiv \exp[-S(\delta N)]$ of such a fluctuation with its relatively high effect on nucleation rate proportional to $\exp(w\delta N/kT)$. This corresponds to the maximum of the combined exponent $-S(\delta N) + w\delta N/kT$. In the Gaussian approximation, $S = \delta N^2/2\bar{N}$, where \bar{N} is the average number of defects in the critical embryo before breakdown. According to section on Shunt nucleation, the latter can be estimated as $\bar{N} = \bar{n}Ld^2$ with \bar{n} being the average defect concentration. This yields $\delta N_{opt} = w\bar{N}/kT$. As a result, the time to breakdown $t_{BD}(T)$ shortens by the factor of

$$\exp[S(\delta N_{opt})] = \exp[-w^2\bar{N}/(kT)^2] \ll 1, \quad (2.20)$$

as compared to the case of homogeneous nucleation. Eq. (2.20) predicts parabolic Arrhenius plot for shunt nucleation rate. The latter tendencies remain when the fluctuation statistics is not Gaussian.

For numerical estimates we use d from Eq. (2.17), $w/kT \sim 30$, $L \sim 3$ nm, $a \sim 3$ Å, and $\ln \xi \sim 30$. With these parameters the heterogeneous nucleation becomes important [i. e. $S(\delta N_{opt}) > 1$] when $\bar{n} > 10^{17}$ cm⁻³, the latter being well in the range of structural defect concentrations in thin oxide materials.¹¹

Concluding remarks on shunt nucleation

Three comments are in order regarding the above consideration. First, the concept of conductive defect path has been known in the literature on dielectric breakdown^{16,17} and described in the terms of percolation theory. On the other hand, a related problem of transversal hopping conductivity in amorphous thin films has long been studied^{28,29} and untypical defect chains (pinholes) were found to be most efficient, even though they are much

less likely than those of the percolation cluster. Eq. (2.12) follows the latter approach. Note, however, that in Ref. 28,29 the problem was to find the most efficient conductive path in a frozen disorder, as opposed to the path created under applied bias in the present framework.

Secondly, the importance of stored field energy has been recognized in the scenario of an independent conductive path formation followed by the electric discharge.³³ To the contrary, the approach here predicts a transition where the ability to form a conductive path is strongly affected by the electric field.

Thirdly, the physical meaning of l is the linear size of the region where a point perturbation affects the electric potential. It coincides with the device lateral dimension (illustrated in Fig. 2.4) when the lateral conductivity is Ohmic. However, if one of the electrodes is a semiconductor, then l becomes voltage-dependent and can be much smaller than the device size.¹⁵ The breakdown will then result in formation of multiple conductive pathes.

Fourthly, we would like to emphasize a peculiar nature of the shunt nucleation transition, which combines the standard first-order transition kinetics with the fact that its final state dissipates energy. The latter feature may resemble that of the charge-density-wave depinning transition (related once to the dielectric breakdown in Mott insulators³¹). Yet, the analogy with the true first-order phase transitions remains, based on the above free energy consideration. The dissipation appears here as a concomitant *local* effect that can be made arbitrarily small by properly choosing the system parameters. In particular, it is straightforward to verify that the energy $V^2 t_{BD}/R$ dissipated during the nucleation time becomes much less than the electrostatic energy when $Lw/aT \ll (\ln \xi)^2$.

Lastly, the above theory does not implicitly address the microscopic nature of defects involved in shunting, and represents rather a phenomenological approach in the terms of defect generation energy w and electron localization radius a . If the latter parameters are field dependent (which is possible for some micro-structures,³²) then the results of this consideration will correspondingly change.

The above predictions are qualitatively consistent with the dielectric breakdown facts, such as t_{BD} dependence on L , l , and T (including curved Arrhenius plots), its stochastic nature, pre-breakdown current oscillations, and observations of single and multiple breakdown spots (see^{16–19,33,34} and references therein). As applied to oxides and other systems, such as reverse biased p-n or Schottky junctions, our consideration predicts shunting of *non-ohmic* nature. Observation of such shunting has been a longstanding folklore and to the best of

our knowledge was never systematically addressed.

We finally mention some additional predictions. They concern shunting by mobile impurities and edge effects.

Conductive paths across the film can be formed by mobile impurity atoms. This phenomenon can be described by the above theory where the role of defect generation energy is played by the corresponding minimum work (per atom) needed to form the path. The latter is expressed through the entropy part of the system free energy,

$$w = kT \ln(N_B/\bar{N}) \quad (2.21)$$

with N_B from Eq. (2.17) and \bar{N} is defined previous sub-section. Because of $W_B \propto kT$, this mechanism results in the temperature independent exponential of t_{BD} in Eq. (2.19), while the preexponential ν^{-1} will represent the thermally activated diffusion time. The dependence $w(\bar{N})$ from Eq. (2.21) will lead to t_{BD} strongly nonlinear in impurity concentration, which can be used to identify this mechanism.

It is typical that defects and impurity atoms accumulate towards device edges. As incorporated into the above theory this predicts shunting to be stronger in the edge region, which is consistent with the recent observations on thin-film photovoltaics.³⁵

2.3.3. Dielectric breakdown in thin film PV

The PV device stability can be hampered by the appearance of shunting-like pathways. As described in the above, a very efficient chemistry independent mechanism of shunt generation is based on decreasing the system capacitive energy $W = CU^2/2$ through the shunt related decrease in local voltage U .

A shunt of resistance $R \gg \rho$ decreases the device potential by approximately $\delta U = U\rho/R \ll U$ in the neighborhood of area L^2 where L is given by

$$L \sim \sqrt{kT/eJ_L\rho} \quad (2.22)$$

where ρ is the electrode sheet resistance; typically $L \sim 1-10$ mm. For a cylindrical capacitor of area πL^2 and thickness l , the corresponding change in stored energy is (see Fig. 2.6)

$$\delta W = 2W \frac{\rho}{R} \quad \text{with} \quad W = \frac{\varepsilon L^2 U^2}{4l}. \quad (2.23)$$

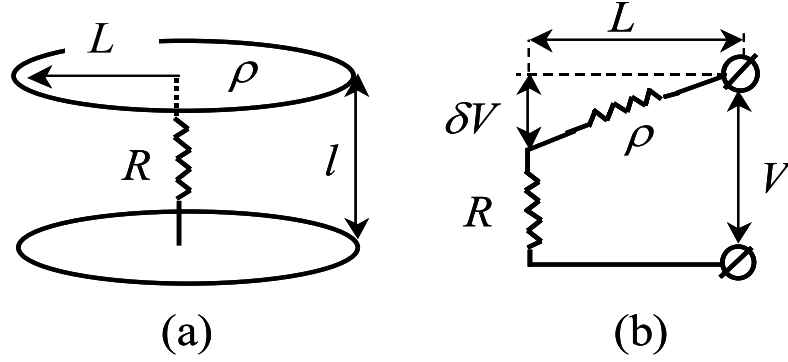


Figure 2.6: Sketch of a defect shunting pathway and its equivalent electric circuit in thin film PV.

It is surprisingly large even for relatively highly resistive shunts due to a very large capacitive energy W . Assuming for numerical estimates $U \sim V_{oc} \sim 1$ V, $l = 1$ μm , $L = 3$ mm, and $\varepsilon = 10$ gives $W \sim 10$ GeV.

The above energy is more than enough to generate a desired number of defects shunting through the device. Indeed, the energy needed to generate N defects is $W_D = wN$ where w is typically of the order of several eV. Even assuming $w = 10$ eV leaves the possibility of creating $W/w \sim 10^9$ defects forming a path of diameter ~ 0.1 μm across 1 μm thick film.

Because the number of defects in a conductive pathway is proportional to device thickness, and the energy $W \propto L^2/l$, the ratio W/W_D describing the possibility of creating a shunt is dominated by the dimensionless parameter

$$\alpha = \left(\frac{L}{l}\right)^2 \gg 1. \quad (2.24)$$

We find it important to point out that α of the ultra-thin PV (say for $L \sim 1$ mm, $l \sim 1$ μm) is of the same order of magnitude as that of the ultrathin oxides in the modern integrated circuits ($L \sim 1$ μm , $l \sim 1$ nm). In the latter case, shunting and dielectric breakdown phenomena are known indeed as a major technology bottleneck and a subject to numerous studies as described in the above. Based on this analogy, it is natural to predict that the dielectric breakdown instability will become a major degradation mode in the future ultra-thin PV, calling upon adequate remedies. Also, based on the latter analogy, the above results of a more quantitative analysis of the dielectric breakdown in ultra-thin oxides must be relevant for ultrathin PV.

2.3.4. *Conclusions*

In conclusion, we have introduced a new type of phase transitions in thin dielectric or semiconductor films where the stored electrostatic energy discharges into structural defects. Depending on its particular realization, the transition kinetics may be either of nucleation or spinodal decomposition type. Our theory describes the dielectric breakdown in ultrathin oxides of integrated circuits and predicts two other phenomena of practical importance: field-induced compensation and Schottky barrier suppression in semiconductor thin films.

2.4. **Spatial and Temporal Current Fluctuations in Polycrystalline Schottky Barriers**

2.4.1. *Introduction*

Applying a metal contact on a semiconductor device results in a Schottky barrier which affects current collection. This phenomenon known as the back barrier or back surface field can affect all major photovoltaics (PV), such as CdTe, silicon, and CuIn(Ga)Se (CIGS)².

Due to the lack of crystallinity, the electronic transport through the back barrier in thin-film can be laterally nonuniform. Even for the case of crystal-based structures, it has been long realized that the barrier transport is inherently nonuniform. The model of laterally fluctuating barrier height V_B was put forward by Tung⁴⁰ and verified in subsequent work (see⁴¹ and references therein). Independently, it was pointed out that in amorphous thin films⁴², Schottky barriers,⁴³ and STM current⁴⁴ defect assisted tunneling can dominate the transport, which then becomes strongly non-uniform with small area patches responsible for the total current flux. Some photovoltaic implications of the back barrier transport nonuniformity were addressed in Ref. 45.

This work is aimed at the experimental study of current transport through microscopically nonuniform Schottky barrier and relating it to the macroscopic barrier parameters. We show that local current through a polycrystalline Schottky barrier strongly varies between different local spots and exhibits large temporal fluctuations at any given location. These strong spatial and temporal variations average out into much smaller yet practically important fluctuations of the device macroscopic parameters.

2.4.2. Experimental Results for MSM structures

Studying the electron transport through back contact in a complete PV device is hampered by the presence of the main junction. To screen against this factor we conducted our experiments on sandwich structures of metal-semiconductor-metal (MSM) deposited on glass substrate that represent two identical barriers. In reality these barriers can be slightly different due to subsequent depositions of semiconductor and top metal layers on the bottom metal contact.

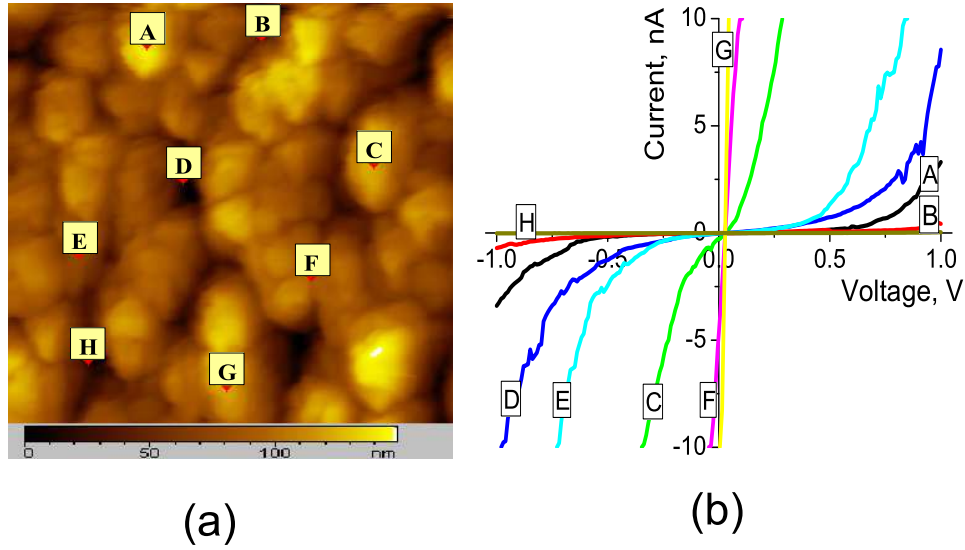


Figure 2.7: Variations in I-V characteristics across the sample (CdTe layer thickness $1.8 \mu\text{m}$). AFM surface scan (a) shows locations where I-V curves (b) were taken.

Cr-CdTe-Cr structures

We used a set of sputtered Cr-CdTe-Cr structures with Cr thickness of about $0.2 \mu\text{m}$ (sheet resistance $\sim 30\Omega/\square$), CdTe thickness of $0.4, 0.7, 1.3$, and $1.8 \mu\text{m}$ and contact area of 1.4 cm^2 . Based on the work function difference, the Schottky barrier between Cr and CdTe is estimated as 0.8 eV , with the depletion width of about $10 \mu\text{m}$; hence all of our structures are fully depleted.

We implemented in parallel microscopic (using AFM with conductive Pt-coated sensor as a probe) and conventional macroscopic (2-point configuration) setups for the current-voltage (I-V) characterization and that of current vs. time $I(t)$ under fixed voltage and

contact location. In both cases bias was applied between the bottom and the top metal contacts.

The microscopic characterization was conducted on Molecular Imaging PicoPlus AFM⁴⁶ in contact current-sensing mode. Following 1 by 1 μm surface scan, we measured local I-V characteristics through the structure at several locations. All samples exhibited strong spot-to-spot variations in I-V not correlated to the topographical features (Fig. 2.7).

Moreover, strong temporal I-V variations between highly conducting and highly resistive states were observed, when measured consequently at the same place for a relatively longer time, say 10 to 1000 seconds, depending on location. We investigated several possible reasons of such behavior. First, the observed AFM tip drift rate of $\sim 0.04 \text{ \AA/sec}$ was too low to explain such strong variations, given the typical tip end diameter of $\sim 100 \text{ \AA}$. Next, we have checked the influence of oxide layer barrier between the tip and its underlying metal as another potential source of the AFM I-V nonlinearity and instability. More specifically, we have verified that when both contacts are attached to a top metal layer during AFM I-V measurement, I-V curves appear linear, much less resistive, and much less noisier. Lastly, conducting the experiment in environmental chamber filled with dry nitrogen, we ruled out the possible effect of moisture. Therefore, the observed I-V reflected the transversal current conduction through the MSM structure.

Typical micro and macro I-V curves are shown side by side in Figs. 2.8 and 2.9 for the thickest and thinnest structures. The former clearly showed the diode type characteristics at both the macro and micro (AFM) levels, while the latter appeared almost linear in both scales. Another difference between samples of different CdTe layer thickness was the applied voltage range in AFM measurements. In order to keep current within instrumental compliance of $\pm 10 \text{ nA}$, we had to follow systematic trend in voltage ranges of 1V, 0.4V, 0.1V, and 0.05V for the CdTe layer thickness of 1.8, 1.3, 0.7, and 0.4 μm respectively.

We emphasize a broadly dispersed character of the micro I-V's taken sequentially. For example, the micro I-V slopes at the origin varied roughly between 0.2 nA/V and 180 nA/V showing only small correlation with the structure thickness, namely thinner structures showed mostly linear IV curves with some locations of diode-like shaped characteristics. From this point of view, the AFM data in Figs. 2.8b and 2.9b are somewhat misrepresentative as restricted to specific spots; other locations showed other randomly varying patterns.

While the macro I-V's are clearly asymmetric (reflecting asymmetry between the two

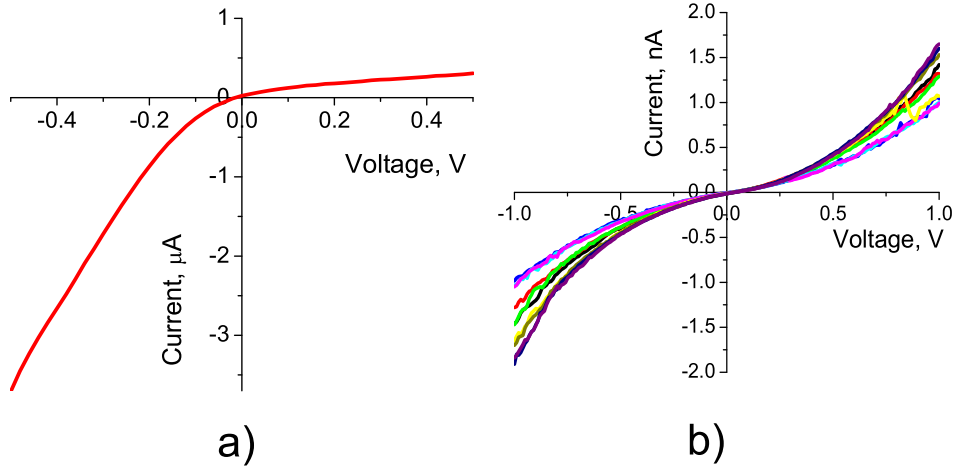


Figure 2.8: Macro (a) and micro (b) I-V curves for a thickest structure, $d=1.8 \mu\text{m}$. A fan of micro I-V curves corresponds to sequential reading taken one after another with a sweep time of 2 seconds.

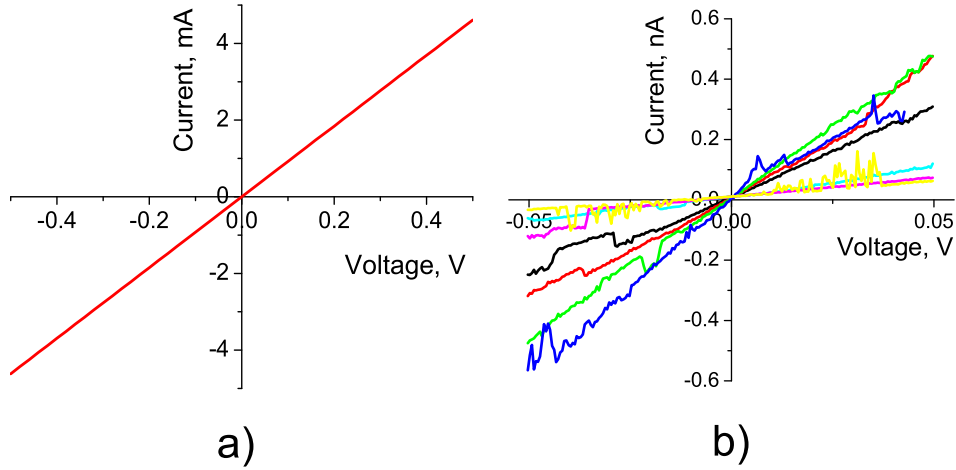


Figure 2.9: Same as in Fig. 2.8 for a thinnest structure of $d = 0.4 \mu\text{m}$. Note the almost linear micro I-V curves and much narrower sweep range as compared to Fig. 2.8.

junctions), the micro I-V's are practically symmetric. A possible cause is that the macro-current is collected from a large area and is sensitive to shunting effects due to localized damage that occurred in the bottom metal contact while undergoing subsequent sputtering of CdTe.

Another typical observation was that nominally identical structures (deposited simultaneously on the same substrate) showed significantly different macro I-V curves. For example,

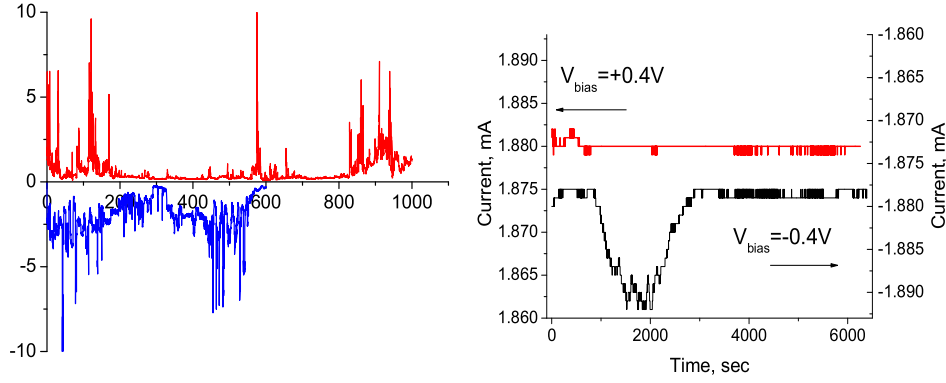


Figure 2.10: Temporal current fluctuations for the case of AFM (a) and conventional probe (b) measurements. CdTe layer thickness $d=1.3\text{ }\mu\text{m}$.

a 'sister' structure to that of Fig. 2.8a, had a linear I-V characteristic. We note that for many large and intermediate thickness samples the macro I-V curves appeared linear, while the micro I-V showed the diode characteristics. This again indicates that the conventional I-V curves are often determined by the existing shunts, while the AFM I-V characterization is not sensitive to remote shunts and reflects the nature of local conductivity in the vicinity of the AFM tip.

We would like to stress the very fact of the AFM current not spreading over the contacting metal, unlike the current generated by the conventional multi-meter probe. We have confirmed this observation with other structures that were chemically different. This fact appears rather counterintuitive and calls upon proper theoretical analysis; its practical implications may be important if this technique used as a mapping tool for characterization of shunted structures.

To analyze the temporal current fluctuations we have tracked the AFM and the conventional macroscopic current as a function of time under fixed bias and probe location. Shown in Fig. 2.10 are the typical results indicating that the microscopic fluctuations are relatively large (exceeding the average current) while the macroscopic current fluctuates much weaker.

Another observed feature of the micro-current temporal fluctuations was that the samples occasionally switched to highly resistive (insulating) state in which no current above the noise level ($\sim 0.02\text{ nA}$) was observed. Typically, after some time (up to several minutes,

generally unpredictable) they returned to a conductive state corresponding to the current fluctuations of the type shown in Fig. 2.10. On the other hand, at some instances, the local AFM currents briefly switched into extremely conductive (shunting) regime (at instrument compliance level of 10 nA), lasting several seconds and then returning back to the fluctuating pattern of Fig. 2.10.

We have performed the Fourier transformation of the observed current fluctuations: for both the AFM and conventional probe currents the noise spectra fall in the domain of what is typically considered the flicker noise⁵²: $f(\omega) \sim \omega^{-\alpha}$ with α varying roughly between 0.6 and 1.1 for different locations on the sample.

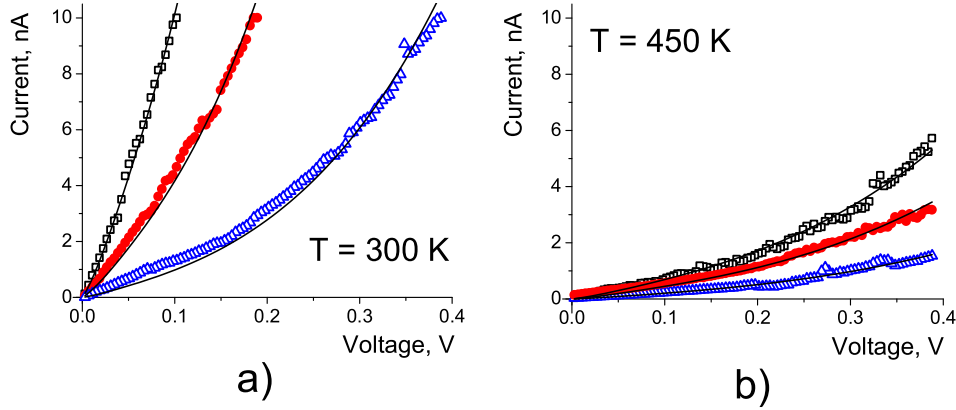


Figure 2.11: Current-voltage characteristics of Cr-CdTe-Cr structure of thickness of $1.3 \mu\text{m}$ at two different temperatures.

Additionally, we have performed the AFM current-voltage characterization under higher temperatures ranging from roughly 300K to 450K. This was achieved by using the Molecular Imaging high temperature stage coupled with Lakeshore temperature controller. The main observation was that the current decreases with temperature in absolute value while retaining the functional shape of I-V characteristics as is illustrated in Fig. 2.11.

Ni-CdTe-Ni structures

Both the top and the bottom Ni contacts were deposited by dc magnetron sputtering at room temperature and deposition pressure of 5 mtorr. The deposition rate of 500 Å/min resulted in a thickness of nearly 1000 Å in two minutes for both the top and bottom metal contacts. The deposition of CdTe on the bottom Ni contact was carried out at the same time as that of Cr. Thus we had four MSM structures of Ni-CdTe-Ni with thicknesses 0.4,

0.7, 1.3 and 1.8 μm , which are the same as that for Cr-CdTe-Cr structures. No annealing step was involved in the fabrication of these MSM structures.

For the Ni-CdTe-Ni structures we have repeated all the experiments described in the preceding subsection: no difference between the cases of Cr-CdTe-Cr and Ni-CdTe-Ni devices was found. Therefore, we omit here the data corresponding to the Ni-CdTe-Ni structures.

Current fluctuations in solar cells

We have studied finished CdTe/CdS solar cells of the standard superstrate configuration² made by rf sputter deposition. The cell structure and band diagram are sketched in Fig. 2.12. The thickness of the CdS and CdTe layers were 0.13 and 2.03 microns respectively. Cells were finished with 30 Å of Cu followed by 200 Å of Au as back contact. Diffusion of Cu into CdTe was carried out by heating the sample in air at 150 °C for 45 minutes. More detail for this cell recipe can be found in Ref. 51.

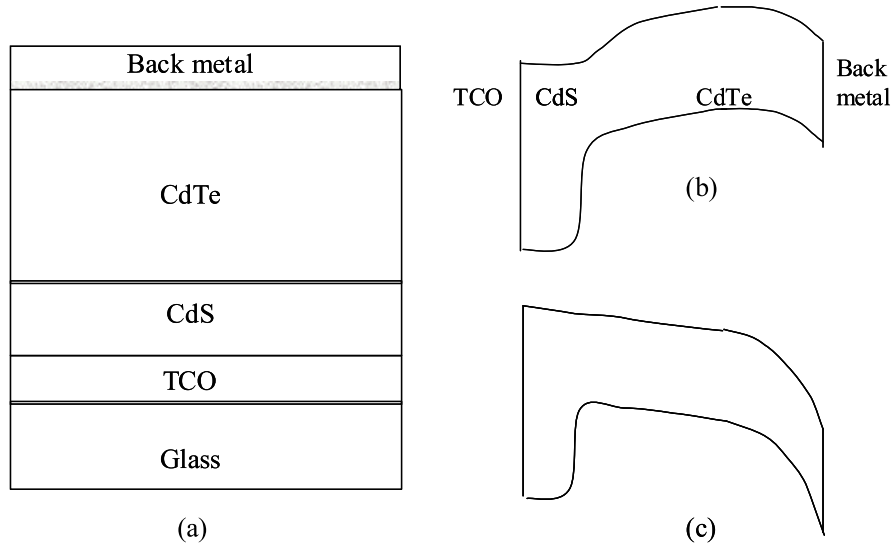


Figure 2.12: Sketch of the physical structure (a) and band diagrams of the CdTe based solar cell under zero (b) and strong forward (c) bias. TCO stands for the transparent conductive oxide

Compared with the MSM structures described earlier, the main difference was that the AFM current fluctuations (both temporal and spatial) typically showed up only under considerable forward bias as illustrated in Fig. 2.13. The fluctuations were suppressed under both moderate forward and reverse bias in the absolute majority of the AFM tip locations.

The forward current fluctuations exhibited the same type of flicker noise characteristics as described for the MSM structures.

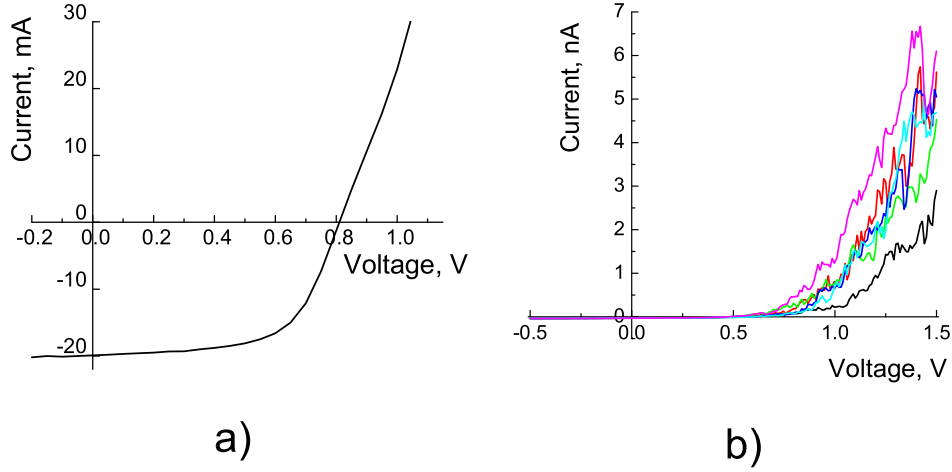


Figure 2.13: (a) The macroscopic current-voltage characteristic for a finished CdTe/CdS cell corresponding to the typical photovoltaic cell parameters and efficiency of 10%. (b) A fan of typical micro I-V curves of the same cell corresponds to sequential reading taken one after another with a sweep time of 2 seconds.

Generally speaking, the observed behavior is consistent with the band diagram of Fig. 2.12 that predicts much stronger back barrier under forward bias. Therefore, we believe that the typical forward current fluctuations in a solar cell reflects the changes occurring in the barrier height at the CdTe/back contact interface. From this perspective, the absence of fluctuations in reverse current tells that the main junction barrier transport is generally much less chaotic.

However, we were able to find several 'abnormal' local spots exhibiting strong current fluctuations under reverse bias too (Fig. 2.14). These spots can be attributed to the local regions of 'abnormally' strong back barrier. It is known indeed that the back barrier strength in CdTe based solar cells depends on the doping level and the cell surface states, both of which can fluctuate in the lateral directions resulting in local spots of 'abnormally' high back barrier⁴⁵.

Summary of experimental observations

We find it appropriate to reduce the above described observations to a summary more

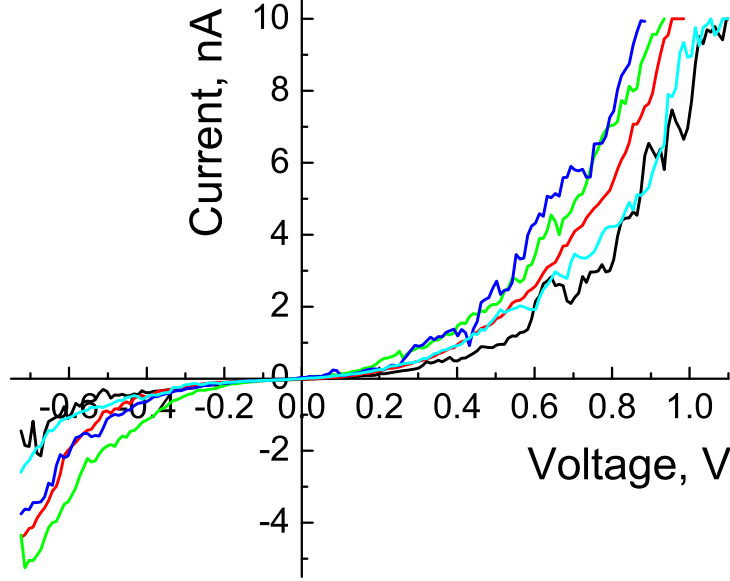


Figure 2.14: A fan of 'abnormal' spot micro I-V curves for a finished CdTe/CdS cell corresponds to sequential reading taken one after another with a sweep time of 2 seconds.

convenient for a theoretical analysis. (1) For the case of MSM structures, the AFM measured micro-current exhibits strong spatial and temporal fluctuations. (2) These fluctuations significantly average out when measured with the conventional multi-meter probe. (3) The AFM current voltage characteristics are super-linear and generally flatten with temperature (in the interval of 300K to 475K); they chaotically change from sweep to sweep. (3) At some instances the AFM current went beyond the setup compliance switching to either insulating or extremely conductive states. (4) For finished solar cells under forward bias, the AFM current behavior is similar to that of MSM structures, but is much less chaotic under reverse bias. (5) We did not observe significant differences between structures with different metals applied as contacts, implying similar barrier heights, similar to results in [53]. (6) Last, but not the least, overall, our experiments show the possibility of the AFM micro-current mapping in the presence of metal contacts and remote shunts.

2.4.3. Theoretical Interpretation

The observed strong spatial and temporal fluctuations suggest that the micro-current is determined by the local conductivity near the AFM tip without spreading over the entire

metal contacts. This implies a highly localized electric field distribution illustrated in Fig. 2.15. However counterintuitive, such a distribution inevitably follows from the above established possibility of AFM current mapping in the presence of metal contacts and macroscopic shunts established in this work.

On the contrary, the macroscopic currents seem to spread over the entire metal contact in accordance with the common sense expectations. This takes place when the probe dimension is large enough, in particular, for the case of a conventional meter probe, which can sense a remotely located shunt and, in general, provide information about macroscopic sample resistance.

At this time, we are not able to theoretically estimate the linear dimensions of the high-field region in Fig. 2.15. A plausible guess is that, having no other characteristic linear scales, the film thickness L remains the only one applicable to that region characteristic diameter. Neither can we quantitatively relate the suggested localized electric field distribution to the fact that it only takes place when the probe (AFM tip) dimension is small, say in the range of several nanometers. The above challenging question remains to be addressed.

In terms of the device band diagram, our interpretation is based on Fig. 2.16 where the two Schottky barriers are more or less symmetric. The observed current variations suggest a transport mechanism exponentially sensitive to local material structure. The barrier activation and tunneling (including their combinations) are conceivable mechanisms discussed in this section.

Applied bias voltage V across the structure is depicted in Fig. 2.16, by the symmetric downward ($-V/2$) and upward ($V/2$) shifts of the Fermi levels in the left and right metal contacts respectively. These shifts do not change the barrier heights for the metal electrons that are determined by the material work functions. The entire system can be sought of as an equivalent circuit of two Schottky barriers of the opposite polarities. It is then straightforward to see that purely activated transport cannot explain the observed super-linear current-voltage characteristics of Figs. 2.7, 2.8 for such an equivalent circuit.

To the contrary, tunneling offers a natural explanation for the observed super-linear IVs. Under small biases, tunneling can take place in combination with activation, in the course of which a hole increases its energy from the metal Fermi level to the top of the semiconductor valence band. This activation energy gradually decreases with the bias and eventually vanishes when the Fermi level E_{F1} in Fig. 2.16 moves below the top of the semiconductor

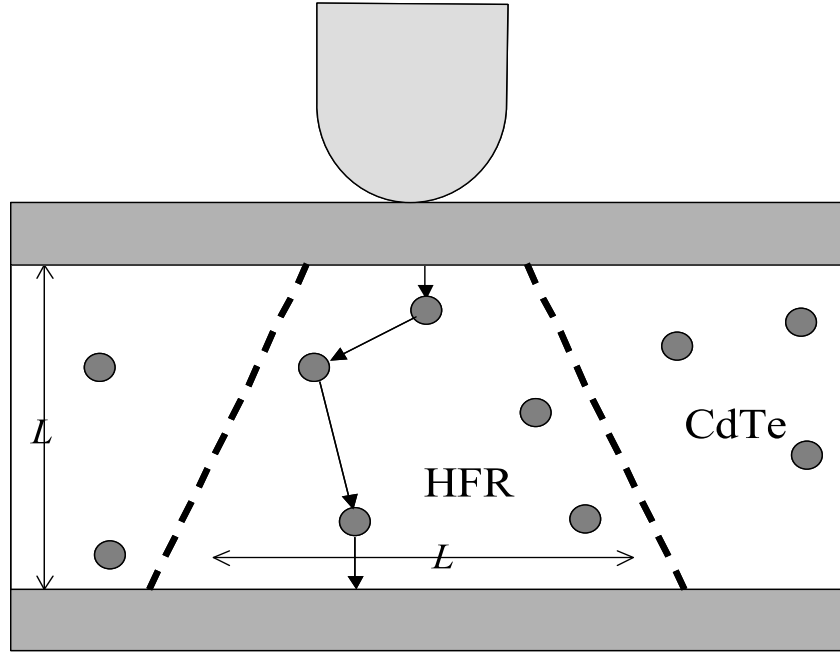


Figure 2.15: Sketch of the electric field distribution and corresponding hopping conduction through the sample. High field region (HFR) is confined between the two dashed lines. Gray circles represent the defects; arrows show the electron hopping.

valence band, resulting in the corresponding super-linear I-V. In the terms of the above equivalent circuit, its constituting two diodes become leaky due to tunneling under reverse bias, which explains the super-linear I-V.

Moreover, the diagram of Fig. 2.16 predicts more or less symmetric micro IVs and yet preserves the possibility of significantly asymmetric macro-IVs when the barrier transparency strongly fluctuates in the lateral directions as explained in what follows.

Activation transport

Even though a purely activation mechanism fails to explain our experimental results, we find it appropriate to discuss it in a bit more of detail so that to establish links with the existing theories of nonuniform Schottky barrier transport. According to the latter, spatial variations in the electric current are due to the local doping concentration fluctuations affecting the Schottky barrier height⁴⁰. This might offer at least a qualitative explanation for the observed spatial variations in the AFM current.

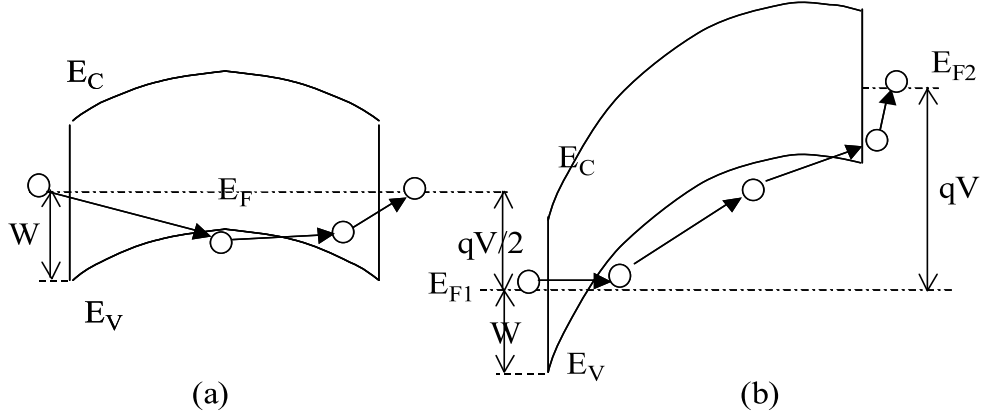


Figure 2.16: Sketch of hole hopping transport through two barriers in the sandwiched structure Cr-CdTe-Cr used in our experiments under external bias $U = E_{F1} - E_{F2}$; dot-dashed lines show the Fermi levels in the metal contacts

To discuss the corresponding temporal fluctuations, we note that because of the large depletion width, the structure thickness L remains the only characteristic length in the system. In particular, local electrostatic perturbations will be screened over the distance L in both the lateral and transversal directions due to the image charges in metal electrodes. Hence, for a qualitative electrostatic analysis, the system can be represented as a set of mutually independent 'elemental' volumes of linear size L .

The electric charge fluctuation δQ changes the energy by $\delta W \sim Q\delta Q/(\epsilon L)$, where ϵ is the dielectric permittivity, $Q \sim qnL^3$ is the total electric charge in the volume L^3 , q is the electron charge, and n is the doping concentration. The corresponding fluctuation in the barrier height is estimated as $\delta V_B \sim q\delta Q/(\epsilon L) \sim \delta W/(nL^3)$ and can be either positive or negative.

These fluctuations occur with the probability $p \propto \exp(-\delta W/kT)$. Taking into account that the electric current $J \propto \exp(-\delta V/kT)$ where δV is positive, one gets

$$p(J) \propto J^{-\alpha}, \quad \alpha \sim nL^3 \gg 1. \quad (2.25)$$

The latter inequality is based on the actual $L \sim 1 \mu\text{m}$, $\epsilon \sim 10$ and $n \gtrsim 10^{14} \text{ cm}^{-3}$ and is inconsistent with the observed flicker noise spectrum ($\alpha \sim 1$).

Overall, we conclude that activation fails to explain the observed temporal fluctuations

in the microscopic current and the super-linear IV characteristics observed in this work.

Direct tunneling Direct tunneling through the semiconductor layer cannot explain the observed current either. Indeed, regardless of the details of the barrier shape, the tunneling probability can be roughly estimated as $\nu_F \exp(-S)$ with $S \sim 2\sqrt{mV_B L^2/\hbar^2} \equiv 2L/a$ where $\nu_F \sim 10^{15} \text{ s}^{-1}$ is the characteristic electron frequency at the Fermi level. With $L \sim 1 \text{ }\mu\text{m}$ and $V_B \sim 1 \text{ eV}$, this gives $S \sim 1000$ even when m is taken to be 0.1 of the electron mass. Such high values of S rule out the direct tunneling as a significant transport mechanism in our systems.

While inefficient here, the direct tunneling may become important for thinner structures or higher voltages (beyond the present setup), for which the effective tunneling distance significantly decreases (see Fig. 2.16). When relevant, this mechanism predicts strong lateral fluctuations in transversal current due to fluctuations in doping concentration and related barrier shape⁴².

Defect assisted tunneling

The idea of defect assisted tunneling (see the review in Ref. 42) is that setting $N \gg 1$ almost equidistant defect states along the rectilinear electron path will result in the much easier electron transport in the form of a sequence of inter-defect transitions. At each step the electron with comparable probabilities ($\sim 1/2$) tunnels forth or back across the distance $L/(N+1) \ll L$. This suppresses the tunneling exponent, and makes the transport much more effective as illustrated in Fig. 2.17.

In applying the above philosophy to our systems, we note that polycrystalline films have high concentration of defects whose energy spectra form bands with the density of states⁴⁸ $g \sim 10^{15} - 10^{17} \text{ cm}^{-3}\text{eV}^{-1}$. Because of the energy dispersion, the inter-defect tunneling includes activation and can be regarded as the hopping transport mechanism. The hopping transversal conduction appears strongly nonuniform in the lateral directions due to local fluctuations in defect concentration that do not average out across the thin film (L is smaller than the correlation radius of hopping percolation cluster⁴⁷).

Because the approach of Ref. 42 remains overlooked in the device physics community, we briefly introduce it in the next subsection.

Optimum paths and fluctuations

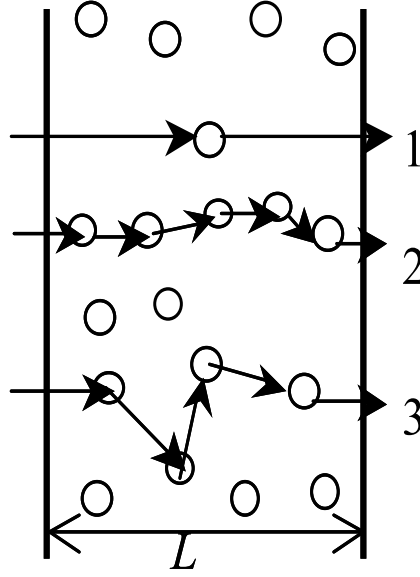


Figure 2.17: Different cases of defect assisted tunneling. Pathways 1, 2, and 3 correspond to the regions of abnormally low, high, and average transparency respectively.

A path of N equidistant defects (Fig. 2.17) has a conductance $R_N^{-1} \propto \exp(-2L/aN)$ where a is the radius of the electron wave function and L/N is the effective tunneling distance. Because R_N exponentially decreases with N , the untypical paths containing abnormally high number of defects become important.

However, the probability of finding such abnormal paths, p_N exponentially decreases with N . Indeed, let p be the probability of finding just one defect in a close proximity of the electron trajectory. The probability to find a trajectory with N defects can then expressed as $p_N = p^N = \exp(-\mathcal{L}N)$ where $\mathcal{L} = \ln(1/p)$.

The competition between R_N and p_N resolves in the optimum paths that maximize the partial conductance,

$$p_N R_N^{-1} \propto \exp\left(-N\mathcal{L} - \frac{2L}{aN}\right), \quad \mathcal{L} \equiv \ln(1/p). \quad (2.26)$$

A straightforward maximization gives the optimum path parameters,

$$N_{\text{opt}} = \sqrt{\frac{2L}{\mathcal{L}a}}, \quad R_{N_{\text{opt}}}^{-1} \propto \exp(-2\mathcal{L}N_{\text{opt}}). \quad (2.27)$$

Eq. (2.27) represents the gain due to defects: reduction of the direct tunneling exponent from $S = 2L/a$ to, roughly, $S \sim 2\sqrt{\mathcal{L}L/a} \ll 2L/a$.

Even though p has not been exactly defined in the above discussion, its related uncertainty appears insignificant under the logarithm in the final result of Eq. (2.27). The probability p can be specified through a more comprehensive analysis taking into account thermal activation⁴², which shows that the electron paths are confined into cylindrical regions of radius $\rho \approx \sqrt{La}$ and that \mathcal{L} is defined through the equation,

$$\mathcal{L} = \ln \left(\frac{\mathcal{L}}{gkTaL^2} \right) \approx \ln \left(\frac{1}{gkTaL^2} \right). \quad (2.28)$$

The realistic \mathcal{L} s are of the order of several units.

The optimum paths will determine the transversal conductance of large area samples, $A \gg A_c$ where the critical area $A_c = 1/n_0$, n_0 being the optimum path surface concentration. Such 'large' systems appear macroscopically uniform showing almost no variations in transversal conductance between nominally identical samples. On the contrary, 'small' samples of area $A \ll A_c$ normally have no optimum paths. Their transversal conductances will appear random (with strong variations between nominally identical devices) as determined by a random most conductive path in each given sample.

The critical area A_c can be macroscopically large. Indeed, dividing the entire film volume into a set of perpendicular cylinders of base area ρ^2 and noting that the probability for a cylinder to contain an optimum path is $p_{\text{Nopt}} = \exp(-N_0\mathcal{L})$, one gets

$$A_c = La \exp \left(\sqrt{2\mathcal{L} \frac{L}{a}} \right). \quad (2.29)$$

For example, $A_c \sim 1000 \text{ cm}^2$ for realistic $L \sim 1 \text{ }\mu\text{m}$, $a \sim 10 \text{ }\text{\AA}$, and $2\mathcal{L} \sim 10$.

Current-voltage characteristics

To describe the JV characteristics of defect assisted tunneling, we follow Refs. 49,50, according to which N-defect chain is represented by $N + 1 (\approx N)$ exponentially different resistors in series, whose resistances $R_i = R_0 \exp(\xi_i)$ depends on random quantities

$$\xi_i = \frac{w_i}{kT} + \frac{2r_i}{a}$$

where w_i and r_i represent the activation energy and distance of the i th pair of centers respectively. In the simplest approximation, random parameters ξ_i are uniformly distributed in some interval $0 < \xi \leq \xi_{\text{max}}$.

Because w_i is the change in *free energy*, it includes the difference between the effective chemical potentials (μ) of the centers defined through their occupation numbers $n = [1 +$

$\exp(\mu - E)/kT]$. This definition enables one to introduce the inter-center electric potential equal to the difference between the center chemical potentials, $\delta V_i = \delta \mu_i$ and $\sum_i \delta V_i = V$.

In the above chain of resistors, the largest voltage drop is across the strongest resistor, i. e. in the pair with the highest available ξ_i . This voltage drop will equalize the chemical potentials of the two defects by altering their occupation numbers and thereby decreasing the pair resistance down to the level of the next large resistor in the chain. Such equalization will sequentially take place in a number of resistors having ξ_i from the maximum one (ξ_{\max}) down to $\xi_0(U)$ defined by the condition

$$\sum_{\xi_0}^{\xi_{\max}} \xi_i = \frac{qV}{kT}.$$

ξ_0 determines the value of the highest resistance $R(V) = R_0 \exp(\xi_0)$ in the chain under bias V . Approximating the sum by the integral gives $(\xi_{\max} - \xi_0)^2/2\xi_{\max} = qV/kT$. As a result the current through the chain is described by

$$J(V) = J_0 \exp \left(-\frac{2L}{Na} + \eta \sqrt{\frac{qV}{kT}} \right) \quad (2.30)$$

where J_0 is the preexponential factor. The numerical coefficient (generally, of the order of the unity) $\eta \approx 1.26$ has been estimated in Ref. 49 for the case of optimum chains in thin amorphous films.

2.4.4. *Fitting the data*

Shown in Fig. 2.18 are several examples of fitting our JV data with Eq. (2.30). Each fit is restricted to one polarity (either positive or negative), since changing the polarity would entail switching between the two Schottky barriers. In fitting a fan of JV curves for a given sample we set the parameter $\eta = 1.26$ equal to its predicted value⁴⁹ and determined $P1 = J_0 \exp(2L/Na)$ as the only best fit parameter varying between different curves.

We emphasize that the predicted shape of the functional dependence $J(V)$ does not contain any fitting parameters at all. In other words, the fitting parameter $J_0 \exp(2L/Na)$ was used to scale the absolute value of $J(V)$ without any effect on its shape.

We have tried a large number of JV curves for the samples of different thicknesses and at different temperatures. In general, Eq. (2.30) describes the $J(V)$ dependencies remarkably

well; quite a unique situation where rather imperfect polycrystalline films are described by a theory without fitting parameters.

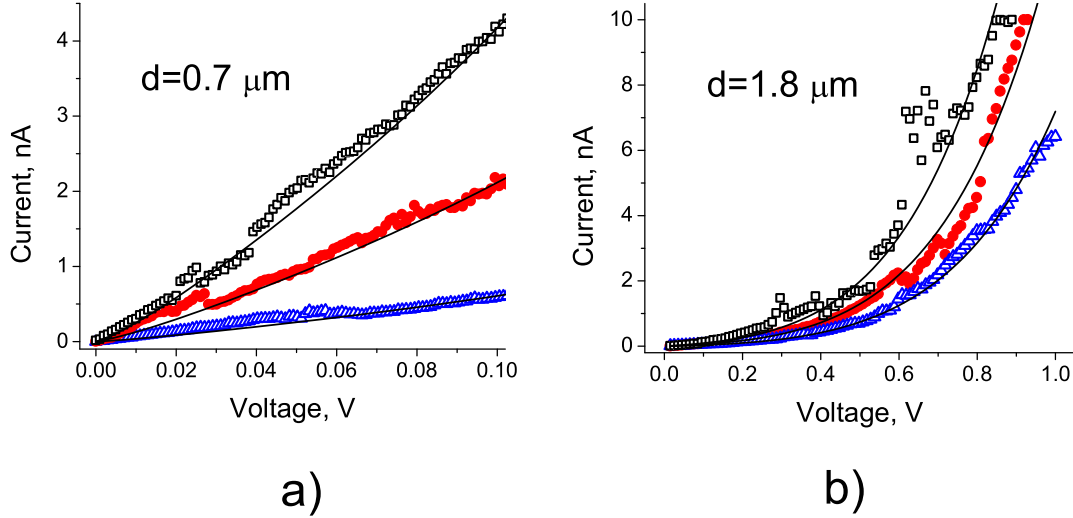


Figure 2.18: Theoretical fits of the measured current-voltage characteristics for structures with different CdTe layer thickness: (a) $0.7 \mu\text{m}$, (b) $1.8 \mu\text{m}$

The best fit parameter $P1$ was found fluctuating between different curves in the range of 10^{-4} to 1 nA . To estimate the corresponding random quantity $2L/Na$ we used the simplest rough approximation for the preexponential factor $J_0 \sim q\nu$ where $\nu \sim 10^{14} \text{ s}^{-1}$ is the hopping frequency of attempt³⁸. This leads to $2L/Na$ in the range of 10 - 20.

Assuming an order of magnitude estimate $2L/a = 10^3$ the latter translates into $N = 50 - 100$. Furthermore, these defects confined in the above described cylinder region of radius $\rho = \sqrt{La}$ and length L are characterized by concentration of the order of $3 \cdot 10^{16} \text{ cm}^{-3}$, in the ballpark of the generally assumed defect concentrations in polycrystalline thin films.

2.4.5. Temporal fluctuations

The observed temporal fluctuations of AFM current cannot be explained by the conventional theory of hopping conduction noise⁵⁵. We have to assume that a pathway configuration considerably varies over time, which has exponentially strong effect on the current. Following the existing interpretation of the conduction flicker noise⁵², we attribute such variations

to defect diffusion.

One subtlety here (emphasized in Refs. 42,49,50) is that at each instance, the defect chain resistance is dominated by its *hardest link*. The current through it is proportional to $\exp(-\xi_0)$ where ξ_0 is a random quantity more or less uniformly distributed within some interval $\sim \sqrt{L/a}$. Corresponding to such a uniform distribution will be the distribution $p(J) \propto J^{-1}$ qualitatively consistent with the observed flicker noise⁵².

The hypothesis of defect mobility underlying the observed flicker noise is consistent with the typical diffusion parameters. Indeed, the order of magnitude current change requires the diffusion over distance $\sim a$, and the corresponding diffusion time can be estimated as $t_D \sim (a/a_0)^2 \nu^{-1} \exp(V_D/kT)$. Here $a_0 \sim 2\text{\AA}$ and $\nu \sim 10^{13} \text{ s}^{-1}$ are the characteristic diffusion step length and phonon frequency, and V_D is the diffusion barrier. Setting $t_D = 1 \text{ s}$ (our sampling time in Fig. 2.10) gives $V_D \sim 1 \text{ eV}$, well in the range of typical V_D in solids.

The next observed feature, that the macroscopic current fluctuations were relatively small, can be explained by the long RC time constant $t_{RC} = RC$ needed to propagate the signal across the entire device. Indeed, in a very rough approximation, the characteristic resistance of individual microscopic pathways can be estimated from the typical AFM JV curve slopes as $R \sim 10 \text{ G}\Omega$. Using our sample geometrical capacitance $C \sim 100 \text{ nF}$ gives $t_{RC} \sim 10^3 \text{ s}$. One can say that the AFM observed microscopic fluctuations average out in such RC time scale.

2.4.6. Conclusion

In brief, a significant experimental finding of this work is that the electron transport in polycrystalline thin-film Schottky barrier exhibit strong spatial and temporal fluctuations. This takes place in both the artificial sandwich structures and finished solar cells. In addition to the main observations listed in the abstract, we would like to emphasize a new physical picture of microscopic time dependent pathways. Our limited AFM experiments on different barrier structures have revealed similar temporal fluctuations, which therefore may be a general feature of the Schottky barrier transport. More work is needed to further clarify this issue.

Our theoretical interpretation is based on the concept of defect assisted tunneling through the Schottky barrier. Remarkably, this interpretation describes the observed J-V shapes

without any fitting parameters for different sample thickness and temperatures. Also, assuming reasonable defect diffusivity, it explains the observed flicker type temporal current fluctuations.

We note certain similarity between here observed gigantic fluctuations and those observed in the gate currents preceding a soft breakdown in ultra-thin dielectrics of modern electronics⁵⁷. Similar transients preceding the device shunting have been observed in CdTe PV.⁵⁸

2.5. Piezo-photovoltaic effect in thin-film CdS-based solar cells

In the third quarter report we have discussed our recently discovered pressure dependence of PV parameters in CdTe solar cells consistent with piezoelectric constants of CdS. At that time we applied pressure perpendicular to the device surface, leading to occasional contact damage. To avoid this problem we have developed new setup which allows us to apply stress in lateral direction via bending the cells.

2.5.1. Introduction

High efficiency CdTe-based solar cells make use of a CdS layer as an absorber junction partner. In the standard p-n junction device model, the CdS layer, while absorbing light, does not contribute to the carrier collection. The role of this material remains poorly understood, and the known attempts to eliminate or replace it have not been very successful. One unique feature of CdS largely overlooked in photovoltaic applications is its strong piezoelectricity, studied extensively in the 1960's.⁶⁰ Taking this feature into account may help to improve the understanding of the CdTe/CdS solar cell, from the device band diagram to the peculiar sensitivity of CdS layer to substrate surface properties, deposition techniques, etc.⁶¹ The question of whether or not CdS retains its piezoelectric properties in PV applications was studied briefly in the 1980's on CdS/Cu₂S devices with null results⁶² and the issue has been largely neglected since then. However, using a pressure application setup similar to that of⁶² we have found that CdS does retain its piezo-properties when used in thin film PV⁵⁹. In our cells CdS film has predominantly wurtzite crystal structure with preferential orientation of the c-axis perpendicular to the film plane. The microscopic origin of the

piezoelectric effect is the displacement of ionic charges within the crystal. The direction of polarization points from S (anion) terminated to Cd (cation) terminated sides of the film along the c-axis depending upon crystal growth direction. Polarization in this type of crystal is related to stress through the piezoelectric tensor

$$P_i = d_{ij}T_j$$

where T_j is the applied stress vector and d_{ij} are the piezoelectric constants (IEEE standard notation⁶³). For CdS, the nonzero constants are $d_{31} = -5.8 \times 10^{-12}$ C/N and $d_{33} = 10.32 \times 10^{-12}$ C/N.⁶⁴ In our experiment the d_{31} corresponds to stress applied perpendicular to c-axis (in plane) and the polarization changes along the c-axis. d_{33} constant corresponds to stress applied parallel to the c-axis and the polarization changes along that same c-axis. When pressure is applied perpendicular to the plane of the material, V_{oc} , J_{sc} , R_s and R_{sh} all undergo changes. These changes are reversible with increasing, then decreasing, pressure⁵⁹. In previous experiments, pressure was applied directly to the contact with a metal-tipped plunger, allowing for current-voltage (J-V) characteristics reading through the same tip. It resulted in occasional damage to the contact. In this work we apply pressure parallel to the plane of the material via bending. This lateral force is in the direction of a "natural" thin-film CdS layer stress, built-in as a result of solar cell fabrication. We examine two types of cells: deposited on glass superstrate and flexible molybdenum substrate. Two corresponding setups, shown in Fig. 2.19 and Fig. 2.20, were used for device bending and J-V data collection.

2.5.2. Experimental

Fabrication of the CdS/CdTe devices We used CdS/CdTe solar cells deposited by rf-sputtering as well as some CSS deposited cells on glass in the superstrate configuration; glass/SnO₂:F/CdS/CdTe. All the devices had standard finishing recipes including CdCl₂ treatment and Au as the back contact with no post-metal heat treatment. Overall, the cells had efficiencies in the range of 8-12%. Also included in this experiment were CdTe/CdS solar cells deposited on flexible molybdenum foil in the substrate configuration; Mo foil/CdTe/CdS/ZnO:Al. These cells were somewhat lower in initial efficiency than those on glass superstrates.

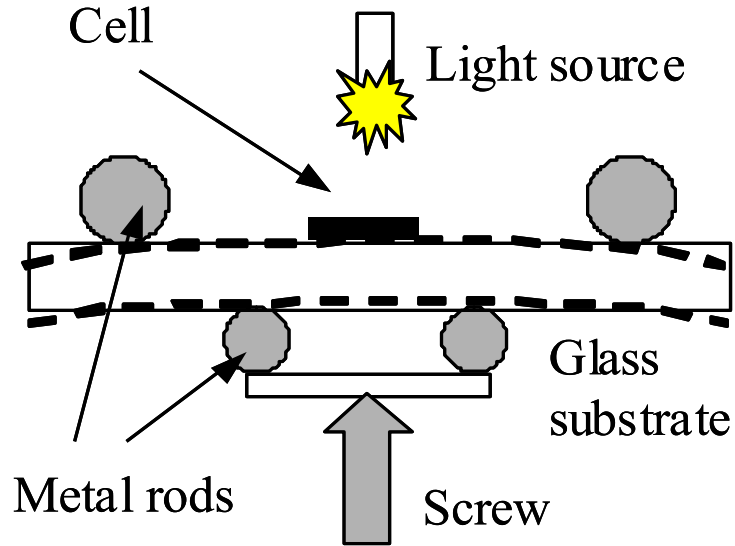


Figure 2.19: Modulus of rupture (MOR) type of bending set-up for devices prepared on glass superstrates.

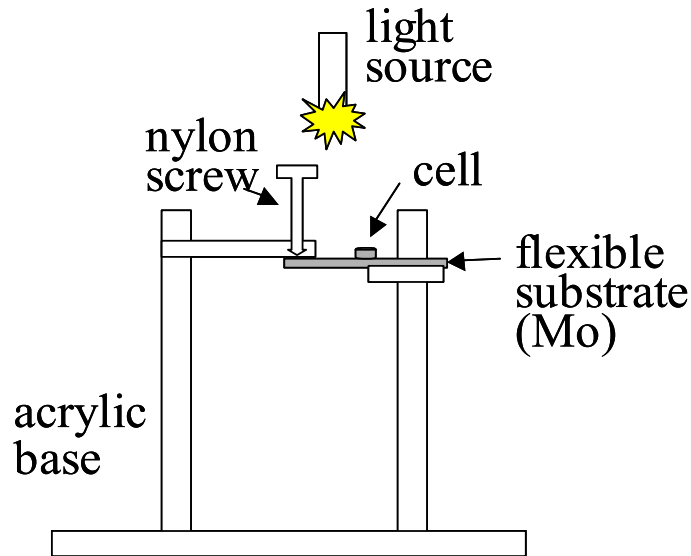


Figure 2.20: Bending setup for solar cells on flexible molybdenum substrates.

Bending setups Our testing set up for solar cells on glass is designed after the 4-point modulus of rupture (MOR) test, Fig. 2.19. Two smooth rods push up from below as two other smooth rods push down from above, holding the solar cell. The screw is tightened slowly pushing the bottom rods up and bending the cell. Light is directed through the glass substrate and J-V measurements are made at different glass edge deflection positions.

Since the pressure is not applied directly to the contact, this method is not destructive to the contact itself. The stress is estimated based on the deflection of the glass measured with high-precision digital micrometer. The solar cell can face down, resulting in lateral compression of the cell, or up (as shown in Fig. 2.19), resulting in the lateral stretching, effectively similar to the pressure perpendicular to the cell as an outcome of the bending of the superstrate.

For solar cells on flexible molybdenum substrates we used setup schematically shown in Fig. 2.20. Since Mo foil is the electrically conductive back contact to the solar cell in this configuration, the apparatus was constructed out of acrylic blocks. The cell is held between the two pieces of acrylic on the right; the nylon screw on the left bends the cell as light is directed from above. A microscope slide positioned on top of the cell fixes the area of the substrate that is bent. J-V readings were taken at different deflections and the stress calculated from the measured deflection caused by the screw. In both cases the stress developed in CdS film was the result of change in its linear dimension $\Delta l/l$ (stretching or compression) due to the corresponding change in the linear dimension of the underlying substrate. This the stress can be expressed as

$$s = E_{CdS} \frac{\Delta l}{l} \quad (2.31)$$

, where E_{CdS} is Young's modulus of CdS. The value of $\Delta l/l$ can be estimated, based on the standard consideration of beam bending for each configuration⁶⁵.

2.5.3. Results and discussion

When the device on a glass superstrate is bent with film (cell) side up, as in Fig. 2.19, the CdS layer becomes stretched, developing stress similar to the case of pressure applied in direction perpendicular to the film surface⁵⁹. For this arrangement we observe the same trend as in our previous experiment. Fig. 2.21 shows typical for this configuration reversible decrease in V_{oc} and relatively small increase in J_{sc} with increasing stress. Some J-V characteristics corresponding to the data in Fig. 2.21 are shown in Fig. 2.22 for the first part of cycle.

As in previous experiments, the amount of stress we apply to CdS is limited by glass breakage. One noticeable difference is that here the range of stresses developing in CdS

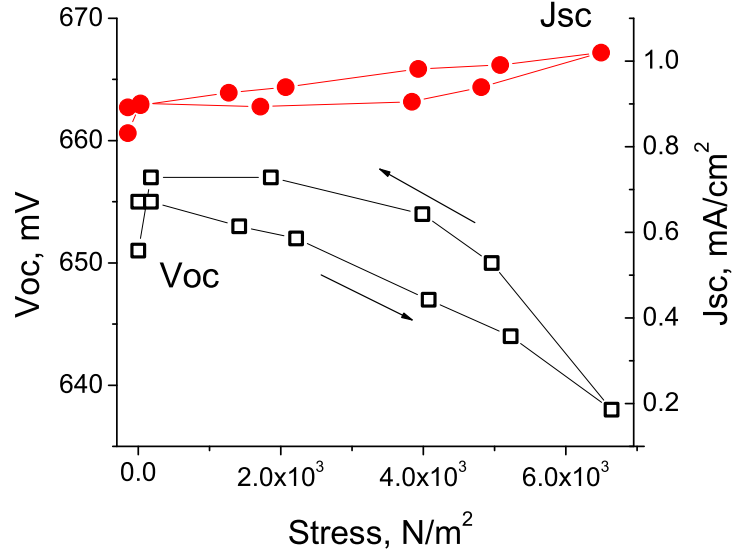


Figure 2.21: Changes in V_{oc} and J_{sc} as a function of stress in CdS film for a device on glass. Cell is facing upward, light intensity is ~ 0.05 sun.

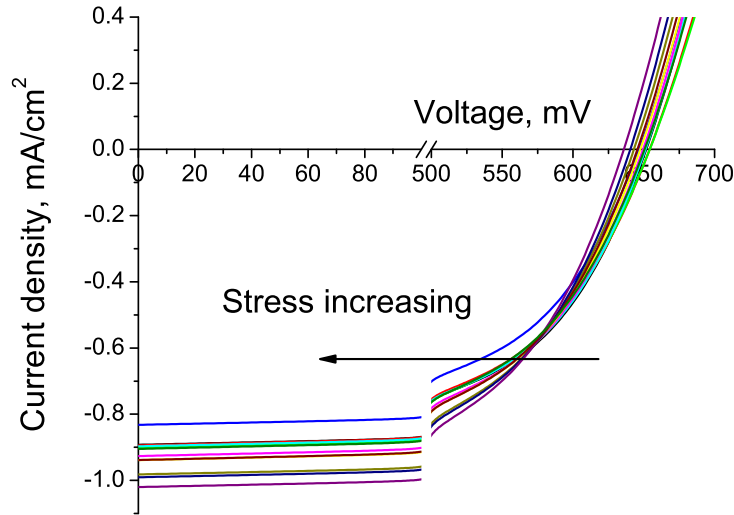


Figure 2.22: J-V curves for a cell on glass measured with increasing pressure and light intensity of ~ 0.05 sun.

film, is about 3 orders of magnitude lower than in our previous experiments. This difference reflects the fact that the glass superstrate is much more brittle when subjected to bending. The stress developing in the glass is estimated to be of an order of 10^5 N/m². In the meantime the amount of stress necessary to break 50 % of glass is defined by its modulus of rupture. For 3 mm soda-lime glass used in our devices this value is of the order of 10^7 N/m², much

higher than our attained values. The abnormal fragility of glass in our experiments is caused by the process of solar cell fabrication involving heating and cooling steps. For example, when a piece of the superstrate with only TCO on it was put in our bending apparatus, we were able to increase the stress in glass by more than an order of magnitude. In addition, due to cutting sides of the glass develop rough spots, which promote crack formation and glass rupture. The main advantage of this new bending setup is that, unlike our previous experiment, the cell under investigation is not in a direct contact with pressure applicator. Therefore the possibility of shunting through the applicator, which was a major concern with the earlier set-up, is no longer an issue. We conclude that the data in Figures 2.21 and 2.22 confirm our previous normal pressure application results as related to piezo-effect in CdS.

Unfortunately, in the film-side-down configuration experiments the glass superstrates broke even easier and cells did not show the expected effect of the V_{oc} increase, opposite to what had been observed in the stretched (film-side-up) cells. In fact, in most cases, the glass broke before the significant change in PV parameters was observed.

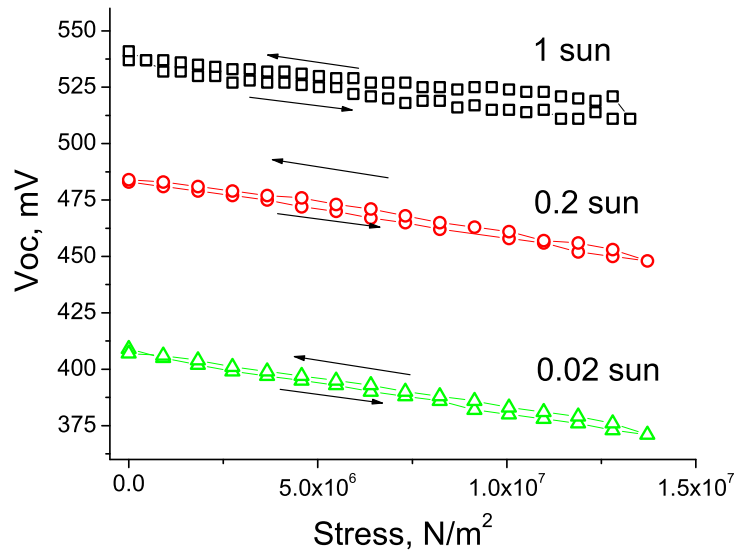


Figure 2.23: Changes in V_{oc} as a function of applied pressure perpendicular to the cell surface at different light intensities.

Solar cells on flexible molybdenum substrates with the film side (contacts) up showed similar changes in V_{oc} and J_{sc} as those cells on glass. J-V data were acquired for complete cycles at three different light intensities, 0.02, 0.2, and 1 sun. Figures 2.23 and 2.24 show the

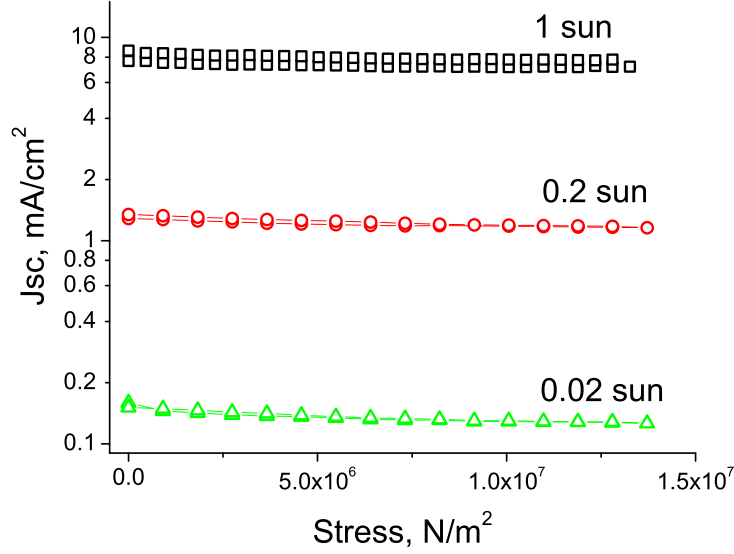


Figure 2.24: Changes in J_{sc} as a function of applied pressure perpendicular to the cell surface at different light intensities.

resulting dependencies on stress for V_{oc} and J_{sc} . Corresponding set of J-V curves measured under 0.02 sun light intensity is shown in Figure 2.25 for increasing stress. As with cells on glass, the effect is more pronounced with lower light intensity. In particular, the V_{oc} decreased as a result of bending by 4.8% at 1 sun, 7.2% at 0.2 sun, and 9.3% at 0.02 sun. This dependence on light intensity may be due to piezo-effect screening by the photo-generated carriers.

While solar cells on flexible substrates represent the most convenient subject for our bending studies, their efficiencies are substantially lower, possibly due to shunting and high back barrier. These factors may reduce the influence of piezoelectricity on PV parameters of the device. In addition, after several bending cycles they tend to undergo inelastic changes probably due to film cracking. As a remarkable example, on fresh cells we observed increase in V_{oc} under stress in the direction of CdS film compression, but this effect became almost undetectable after several flexing sequences.

2.5.4. Conclusions

The change in V_{oc} as a result of lateral stretching (compressive stress applied perpendicular to the film surface) is in agreement with our previous findings, confirming the piezoelectric

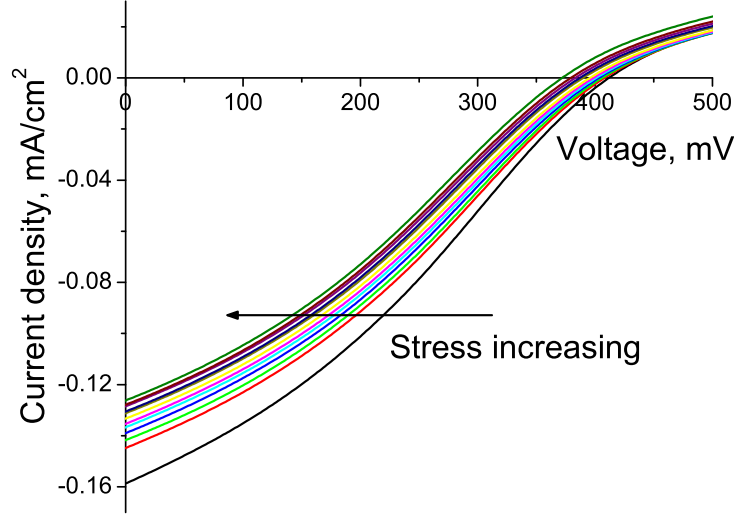


Figure 2.25: J-V curves for a flexible cell showing decreasing PV parameters with increasing pressure. Light intensity ~ 0.02 sun.

properties of the CdS layer in thin film PV. The changes in V_{oc} and J_{sc} were observed in both the substrate and superstrate configurations of CdTe-based cells. In addition, we point out that we have also observed this effect in CIGS cells⁶⁶.

We emphasize that the internal pressure induced static piezo voltage in a device may be very significant, reaching several tenths of a Volt. This results from the intrinsic stress thin films always contain.

Unfortunately, the overlap between the amount of applied stress necessary to clearly see the expected piezo-effect as a result of lateral compression (stress is applied parallel to the film surface) and the amount of stress which the glass superstrates can withstand without breaking makes observation of changes in J-V parameters difficult in devices on glass. For solar cells on flexible substrates the effect was partially masked by initial poorer performance as well as film cracking after several bending cycles.

Practical implications of the piezo-photovoltaic coupling discussed in our work concern the role of device internal pressure accumulated in the process of deposition due to lattice mismatches, substrate or superstrate morphology, CdS dilation and internal pressure due to its doping, and role of atomic diffusion and heat treatments in CdS grain electric dipole orientation.

2.6. Synchrotron X-ray Absorption Fine Structure (XAFS) and X-ray Emission Spectroscopy (XES) Studies on Copper-diffused CdS

X-ray absorption fine structure (XAFS) is a powerful technique in materials science research for understanding the lattice environment around designated element atoms. By using the fine structure in the Cu K-edge x-ray absorption spectrum we elucidate the lattice location of Cu in polycrystalline, thin-film CdS. In particular, during this Phase, we have studied how the typical CdCl₂ vapor treatment in dry air changes the local environment of the Cu in CdS.

To study the Cu K-edge XAFS in CdS film, we prepared thicker layers of approximately 1.8 μm rather than 0.13 μm as in our standard sputtered CdS/CdTe solar cells. The attenuation of x-ray photons through CdS in the photon range from 8800 to 9800 eV, which is the typical range we scan for Cu K-edge XAFS, is estimated to be in a range from 14 to 20 μm .⁶⁷ However, 1.8 μm thick CdS can absorb more than 10% of the x-ray beam and is still within the capability of our sputtering deposition chambers. Fused silica slides are chosen as the substrate to avoid any heavy element contamination as in regular glass, particularly Cu impurities. The surface of fused silica slides were roughened with 0.5 μm Al₂O₃ powder before CdS deposition to improve adhesion between the CdS layer and substrates in order to prevent delamination of CdS under the extremely intensive synchrotron x-ray beam. After CdS deposition, a standard chloride treatment was performed on half of the film, which is annealed at 387 °C for 30 minutes with flowing dry air. Then a 30 Å Cu layer was evaporated and diffused into both the as-grown and chloride-treated CdS films simultaneously. The diffusion was carried out in a quartz tube furnace at 150 °C for 45 minutes flowing with Ar at 45 mL/minute. The XAFS spectra of both copper-diffused as-grown and chloride-treated CdS film were collected at MRCAT in the Advanced Photon Source, Argonne, IL, in a fluorescence geometry. Standard spectra extraction were performed as described in our previous publications.^{68–70} For a qualitative analysis, both magnitude and the real part of phase-uncorrected radial distribution functions $\chi(R)$ of EXAFS spectra after Fourier transform are plotted in Fig. 2.26 and Fig. 2.27. The significance of the real part of $\chi(R)$ function has been discussed in Xiangxin Liu’s Ph.D. thesis⁷⁰ and is briefly described below.

The Fourier transformed EXAFS data actually consists of a complex function, which has real and imaginary parts, or alternatively a modulus and phase. The modulus is the most

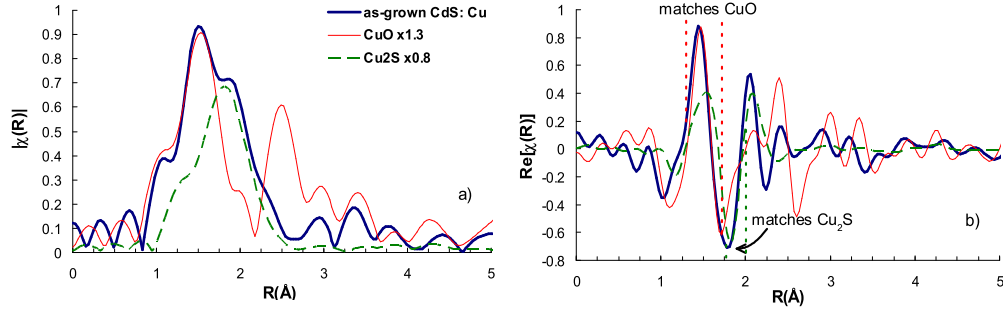


Figure 2.26: Qualitative analysis on $\chi(R)$ of Cu-diffused as-grown CdS film. a) The magnitude of $\chi(R)$, the shortest peak of which matches the 1st primary peak of CuO at ~ 1.56 Å and the shoulder at around 1.87 Å matches the 1st primary peak of Cu₂S; b) The real part of $\chi(R)$ function, which confirms the matches to CuO and Cu₂S in the same region.

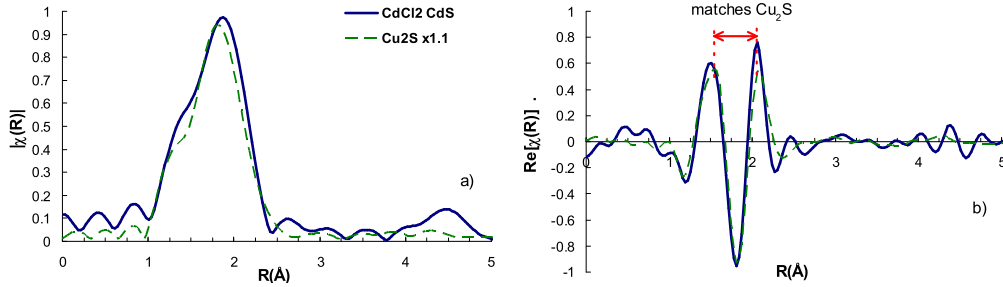


Figure 2.27: Qualitative analysis on $\chi(R)$ of Cu-diffused, chloride-treated CdS film. a) The magnitude of $\chi(R)$, the primary peak of which at around 1.87 Å matches the one of Cu₂S, except for a little distortion of peak shape; b) The real part of $\chi(R)$ function, which confirms the match to Cu₂S in the radial range from 1.5 to 2.1 Å.

frequently used quantity, but the real and imaginary parts are also useful. They exhibit significantly more structure than the modulus and do not suffer from nonlinear interference. The Fourier transform is a linear operation, that is, the Fourier transform of a sum of sine waves in k -space is also just the sum of the Fourier transforms of the different contributions. Calculation of the modulus, however, is a nonlinear operation. Therefore adjacent peaks can interfere with each other in the "transformed" function, rather than superimpose on each

other.

The qualitative analysis with the magnitudes and real parts of $\chi(R)$ (Fig. 2.26 and Fig. 2.27) indicates that there are comparable amounts of CuO and Cu₂S existing in CdS films without prior CdCl₂ treatment, but only Cu₂S in the film with CdCl₂ treatment prior to the Cu deposition and diffusion. Our theoretical fitting by the *ab initio* multiple scattering modeling code of FEFF 8.20⁷¹, shown in Fig. 2.28 also confirms the existence of CuO and Cu₂S in as-grown CdS and Cu₂S in the chloride-treated CdS. Through the theoretical fitting we found that a small portion of elemental copper also exists in the as-grown CdS, which contributes to the small shoulder at around 2.3 Å in the $|\chi(R)|$ spectrum (Figure 2.26a). We suggest the existence of CuO and elemental Cu in the as-grown CdS film indicates some remaining Cu on the surface of CdS after the 45 minutes' diffusion in flowing Ar. The oxidization of Cu may be due to residual O₂ in the quartz tube. However, since the CdCl₂-treated CdS film was heated simultaneously with the as-grown one and there is no obvious existence of either copper oxide or metallic copper in this film (Figure 2.27a and Table 2.1), this may indicate faster diffusion of Cu atoms in the chloride-treated CdS films than in the as-grown one, which may lead to no residual Cu layer remaining on the CdS surface in our sample. However, more investigation is necessary in order to explain the absence of CuO and metallic Cu in the chloride-treated CdS film.

bond scattering	N	R(Å)	dR(Å)	$\sigma^2(10^{-3} \text{ Å})$	ΔE_0
Cu-diffused CdS without CdCl ₂ treatment					
Cu-O (CuO)	1.30 ± 0.33	1.94 ± 0.08	-0.01	4.22 (fixed)	6.3 ± 8.8
Cu-S (Cu ₂ S)	1.20 ± 0.30	2.14 ± 0.05	-0.15	0.05 (fixed)	
Cu-Cu (Cu ₂ S)	0.84 ± 0.21	2.16 ± 0.04	-0.12	0.13 (fixed)	
Cu-Cu (Cu)	0.55 ± 0.14	2.53 ± 0.07	-0.02	8.25 (fixed)	
Cu-diffused CdS <i>with</i> prior CdCl ₂ treatment					
Cu-S (Cu ₂ S)	2.17 ± 0.55	2.17 ± 0.06	-0.11	0.05 (fixed)	3.6 ± 4.6
Cu-Cu (Cu ₂ S)	1.21 ± 0.31	2.18 ± 0.05	-0.11	0.13 (fixed)	

Table 2.1: Theoretical FEFF fitting parameters to the CdS with and without prior chloride treatment. Note: $dR = R_{fit} - R_{ref}$ is the path-lengths shift relative to the reference.

It is also worth pointing out that we observed similar Cu K-edge EXAFS spectra on the

as-grown and chloride-treated before. However, due to x-ray beam damage, some of the CdS films always delaminate from the smooth substrates during the long period of data collection and make the spectra not analyzable. In the run of Oct. 2005, we improved the adhesion between the CdS and substrate by roughening the quartz slide surface and found no evidence of delamination of CdS layer under the high intensity synchrotron beam.

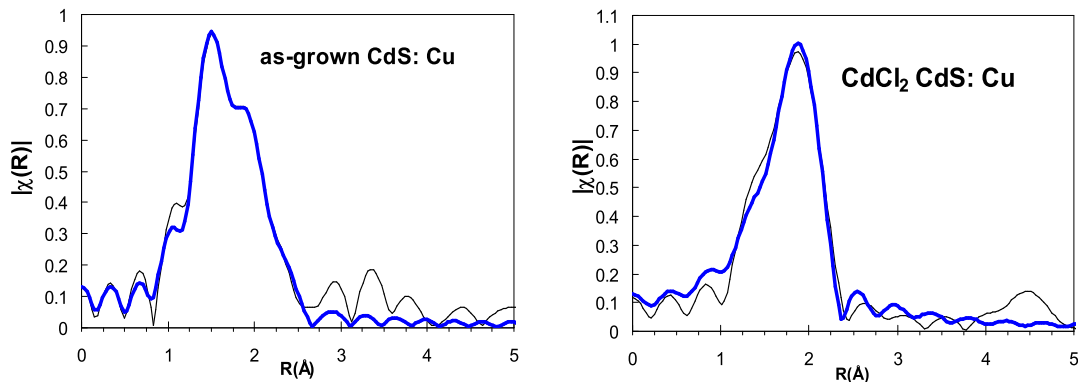


Figure 2.28: Theoretical FEFF fitting to the $\chi(R)$ functions of the copper-diffused, as-grown and chloride-treated CdS films. Fine lines: experimental spectra; thick lines: theoretical fits.

To understand the oxidization of the as-grown CdS film, we sent the same samples with and without the evaporated Cu layer, along with a CdCl₂ treated film with no intentional Cu, to Lothar Weinhardt working with Professor Clemens Heske at the University of Nevada, Las Vegas. They performed X-ray Emission Spectroscopy (XES) at the Advanced Light Source, Lawrence Berkeley National Lab. In most experiments, Sulfur 2p core holes were generated by an x-ray beam with energy of 200 eV. For the three samples and a CdS reference, the fluorescence spectra decaying from the valence band were then collected as plotted in Figure 2.29a. The typical signature of a CdS S L_{2,3} XES spectrum is found in all samples, namely a dominant peak from S 3s states at approximately 148 eV, two sharp peaks just above 150 eV, corresponding to the Cd 4d-derived bands, and the upper valence band of CdS above 154 eV. The difference spectra between the different samples show a significant deviation only in the case of the Cu-diffused sample. As shown in Figure 2.29b, the difference between the Cu-diffused and the as-grown sample indicates a loss in intensity at the S 3s main peak (for a sulfide) and the Cd 4d-derived bands. In contrast, an intensity increase appears around 155 eV and above 160 eV, which is indicative of sulfate formation. This can be

seen by comparing the difference spectrum with a CdSO_4 reference. The sulfate spectrum is markedly different due to a large chemical shift of the S 2p core levels and the (partial) occupation of S 3d-derived states.

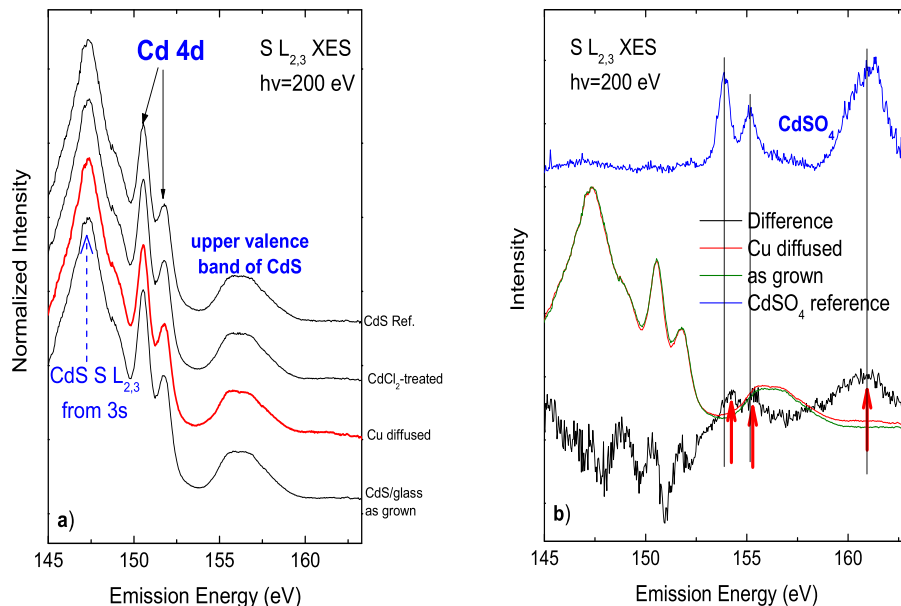


Figure 2.29: a) Sulfur $L_{2,3}$ XES spectra of CdS reference, CdCl_2 treated CdS, as-grown CdS and Cu-diffused as-grown CdS films. b) Sulfur $L_{2,3}$ XES spectra of as-grown CdS and the Cu-diffused CdS film, along with their difference spectrum and a CdSO_4 reference. The Intensity increase around 155 eV and above 160 eV in the difference spectrum indicates CdSO_4 formation.

An interesting feature observed in XAFS is that the as-grown film and the Cu-diffused as-grown film are distinguished only by being from different areas on the same sample. They experienced exactly same treatment and history such as heating in the quartz tube at 150 °C for 45 minutes. However, only the area with intentional Cu forms sulfate. We also observed copper oxide in XAFS spectra from the same sample. All these may suggest that Cu in CdS without prior chloride-treatment not only is oxidized readily by itself but also enhances the oxidization of sulfur. The same CuO and Cu_2S were also observed and reported by Takashi Abe et al.⁷² on their Cu doped as-grown CdS films which were diffused in vacuum. All these results suggest a strong tendency for copper to be oxidized by ambient oxygen.

Another remarkable result of the theoretical fitting to the XAFS spectra of CdS films is path-length shifts (Table 2.1) of Cu-Cu and Cu-S bonds to shorter distances in both CdS

films than the ones in the Cu_2S reference. An XAFS spectrum of Cu_2S reference powder, which was spread uniformly between two polymer tapes, was collected in transmission geometry.⁶⁹ The XAFS of Cu_2S reference was fitted with a known Cu_2S structure to obtain the path-lengths - R and mean square fluctuation factors due to thermal vibration - σ^2 in the reference crystal. The path-lengths - R of Cu-S and Cu-Cu bonds in the proposed model structure employed in the fitting are both 2.27 Å. The ones of Cu-S and Cu-Cu bonds obtained in fitting for the Cu_2S reference are both found to shift only -0.03 Å within fitting error compared to the ones in the proposed structure, which are ignorable (details of fitting results are not shown in this report). However, the same paths in our copper-diffused CdS films, either with or without prior chloride treatment, are found to shift (Table 2.1) more than 0.1 Å to shorter distances compared to the ones in reference. All the shifts are larger than fitting errors and not ignorable.

We suggest this can be explained by the model proposed by Takashi Abe et al.⁷² which suggests that Cd^{2+} are substitute by Cu^+ in CdS lattice base upon their XPS and HRTEM-EDX. In the hexagonal CdS structure, one Cd^{2+} binds with four S^{2-} three of which on the same (002) lattice plane as shown in Figure 2.30. When Cu^+ substitute the Cd^{2+} , two or more Cu^+ may fill in the Cd vacancy defect which will lead to compression on the Cu-S and Cu-Cu bonds from CdS lattice due to limited space.

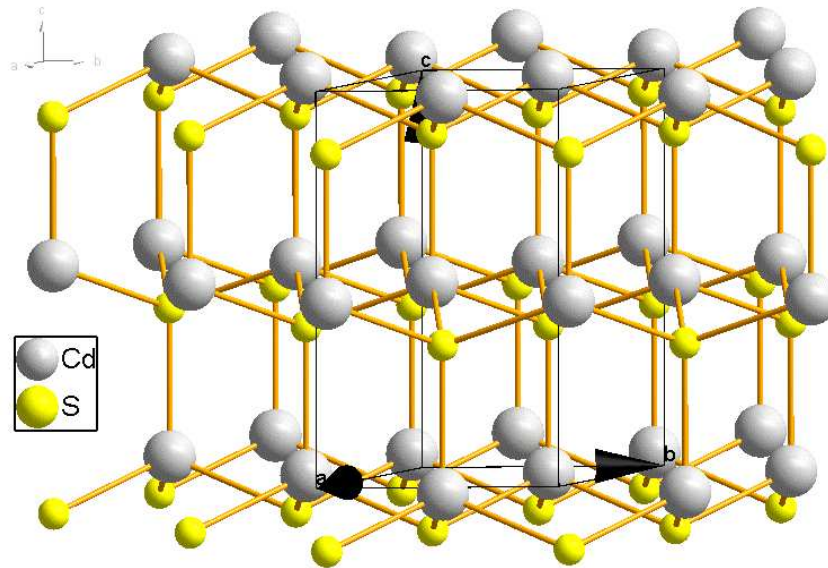


Figure 2.30: Atomic structure of hexagonal CdS, space group $P 6_3 m c$, $a = 4.1348$ Å, $c = 6.7490$ Å.

In conclusion, through our XAFS experiment and data analysis in this phase, we observed that Cu diffused into sputtered CdS films mostly bind with S as a similar chemical state in Cu₂S either with or without the prior chloride-treatment on the CdS films. We also found the path lengths of Cu-S and Cu-Cu bonds of the structure similar to Cu₂S in the films is more than 0.1 Å shorter than the ones in Cu₂S reference. One possible explanation is that Cu diffuses into CdS crystal and substitutes Cd²⁺ in the chemical state of Cu⁺. We also found CuO in the CdS film without prior chloride-treatment, which is absent in the film with chloride-treatment. More investigations are necessary to explain this phenomenon.

References

- ¹ B. von Roedern, K. Zweibel, and H. S. Ullal, *Proceedings 31th IEEE Photovoltaic Specialists Conference*, Coronado Springs, FL, January 3-7, 2005; IEEE, Piscataway, NJ (2005), p. 183.
- ² W. N. Shafarman and L. Stolt, in *Handbook of Photovoltaic Science and Engineering*, p. 567, Edited by A. Lique and S. Hegedus, Wiley, Chichester, 2003; B. E. McCandless and J. R. Sites, *ibid.*, p. 617.
- ³ M. Gloeckler, A. L. Fahrenbruch, and J. R. Sites, *Proceedings of the 3rd World Conference on Photovoltaic Energy Conversion*, Osaka, Japan, 11-18 May 2003, p. 491, IEEE, Piscataway, NJ (2003).
- ⁴ AMPS is a software package developed by Penn State University and aimed at simulating semiconductor multilayer devices; available at <http://www.psu.edu/dept/AMPS>.
- ⁵ D. Shvydka, J. Drayton, A. D. Compaan, and V. G. Karpov, *Appl. Phys. Lett.* **87**, 123505 (2005)
- ⁶ Y. Roussillon, D. Giolando, D. Shvydka, A. D. Compaan, and V. G. Karpov, *Appl. Phys. Lett.* **84**, 616 (2004).
- ⁷ C. Ferekides, private communication; see: www.nrel.gov/ncpv/thinfilm/docs/DevPhys-Ferekides.ppt.
- ⁸ S. Hegedus, private communication and *National CdTe R&D Team Meeting Minutes*, Editors P. V. Meyers and H. S. Ullal, NREL Golden, CO, January 27-28 (2000), Appendix 12.
- ⁹ S. Hegedus, D. Ryan, K. Dobson, B. McCandless, and D. Desai, *Mater. Res. Soc. Symp. Proc.*

- 763**, B9.5.1 (2005).
- ¹⁰ Based on different argument, the concept of CdS related barrier was suggested in: G. Agostinelli, D. L. Bätzner, M. Burgelman, *Thin Solid Films*, **431-432**, 407 (2003).
 - ¹¹ S. M. Sze, *Physics of Semiconductor Devices* (Willey & Sons, New York, 1981).
 - ¹² Y. Roussillon, V. G. Karpov, D. Shvydka, J. Drayton, and A. D. Compaan, *J. Appl. Phys.*, **96**, 7283 (2004).
 - ¹³ D. Liao and A. Rockett, *Proc. 28th IEEE Photovoltaic Specialists Conference*, Anchorage, AL, September 15-22, 2000; IEEE, Piscataway, NJ (2000) p. 446.
 - ¹⁴ X. Li, D. W. Niles, F. S. Hasoon, R. J. Matson, and P. Sheldon, *J. Vac. Sci. Tech. A* **17(3)**, 805 (1999).
 - ¹⁵ V. G. Karpov, A. D. Compaan, and Diana Shvydka, *Phys. Rev. B* **69**, 045325 (2004).
 - ¹⁶ S. Lombardo, J. H. Stathis and B. P. Linder, *Phys. Rev. Lett.* **90**, 167601 (2003).
 - ¹⁷ M. A. Alam, R. K. Smith, B. E. Weir, and P. J. Silverman, *Nature* **420**, 378 (2002).
 - ¹⁸ A. I. Kingon, J-P. Maria and S. Streiffer, *Nature*, **406**, 1032 (2000).
 - ¹⁹ P. A. Pacan, *Science* **285**, 2079 (1999).
 - ²⁰ B. T. Kolomiets and E. A. Lebedev, *Radiotekh. Electron.* **8**, 2037 (1963). E. A. Lebedev and K. A. Tsendin, *Semiconductors* **32** 838 (1998).
 - ²¹ S. R. Ovshinsky, *Phys. Rev. Lett.* **21**, 1450 (1968).
 - ²² D. V. Lang, J. D. Cohen, and J. P. Harbison, *Phys. Rev. Lett.* **48**, 421 (1982).
 - ²³ I. Pelant, *et. al.*, *Thin Solid Films* **383**, 101 (2001).
 - ²⁴ E. Hartmann, R. J. Behm, G. Krotz, G. Muller, F. Koch, *Appl. Phys. Lett.* **59**, 2136 (1991).
 - ²⁵ K. Gartsman, D. Cahen, and R. Scheer, *Appl. Phys. Lett.* **79**, 2919 (2001)
 - ²⁶ T. J. McMahon, M. S. Bennet, *Solar Energy Mater. Solar Cells* **41/42**, 465 (1996).
 - ²⁷ V. G. Karpov and D. W. Oxtoby, *Phys. Rev. B* **54** 9734 (1996).
 - ²⁸ M. Pollak and J. J. Hauser, *Phys. Rev. Lett.*, **31**, p. 1304 (1973).
 - ²⁹ M. E. Raikh and I. M. Ruzin, in *Mesosocopic Phenomena in Solids*, Edited by B. L. Altshuller, P. A. Lee and R. A. Webb, Elsevier, 1991, p. 315.
 - ³⁰ V. G. Karpov, G. Rich, A. V. Subashiev, and G. Dorer, *J. Appl. Phys.* **89**, 4975 (2001).
 - ³¹ Y. Taguchi, T. Matsumoto, and Y. Tokura, *Phys. Rev. B*, **62**, 7015 (2001).
 - ³² J. W. McPherson, R. B. Khamankar, and S. Shanware, *J. Appl. Phys.* **88**, 5351 (2000).
 - ³³ B. E. Weir *et. al.*, *Solid State Electronics*, **46**, 321 (2002).

- ³⁴ R. Degraeve, B. Kaczer and G. Groeseneken, *Semicond. Sci. Technol.* **15**, 436 (2000).
- ³⁵ D. Albin, *private communication*. D.S. Albin, T.J. Berniard, S. H. Demtsu, and T.J. McMahon, to appear in *Prog. Photovolt: Res. Appl.* (2004).
- ³⁶ J. W. Cahn, *Transaction of Metallurgical Society of AIME*, **242**, 166 (1968).
- ³⁷ U. V. Desnica, *Prog. Cryst. Growth Charact. Mater.* **36**, 291 (1998); S.C. Erwin and A.G. Petukhov, *Phys. Rev. Lett.*, **89**, 227201 (2002); J. D. Chadi, *Jpn. J. Appl. Phys., Part 1*, **38**, 2617 (1999).
- ³⁸ N. F. Mott and A. Davis, *Electronic Processes in noncrystalline materials*, Clarendon, Oxford (1971); N. T. Bagraev, L. N. Blinov, and V. V. Romanov, *Physics of the Solid State*, **44**, 816, (2002) [*Fizika Tverdogo Tela*, **44**, 785 (2002)].
- ³⁹ Experimental evidence of Schottky barrier suppression was recently found for the case of CdS thin film (Y. Roussillon, V. G. Karpov, Diana Shvydka, A. D. Compaan, and D. M. Giolando, to appear in *Appl. Phys. Lett.* (2004)).
- ⁴⁰ R. T. Tung, *Appl. Phys. Lett.* **58**, 2821 (1991).
- ⁴¹ L. E. Calvet, R. G. Wheeler, and M. A. Reed, *J. Appl. Phys.*, **80**, 1761 (2002); H.-J. Im, Y. Ding, and J. P. Pelz, W. J. Choyke, *Phys. Rev. B*, **64**, 075310 (2001).
- ⁴² M. E. Raikh and I. M. Ruzin, in *Mesoscopic Phenomena in Solids*, eds B. L. Altshuller, P. A. Lee, and R. A. Webb, Elsevier, (1991), p.315.
- ⁴³ E. J. Miller and E. T. Y., P. Waltereit and J. S. Speck, *Appl. Phys. Lett.*, **84**, 535 (2004).
- ⁴⁴ B. Grandidier, X. de la Broise, D. Stievenard, M. Lanoo, M. Stellmacher, J. Bourgoin, *Appl. Phys. Lett.*, **76**, 3142 (2000).
- ⁴⁵ Y. Roussillon, V. G. Karpov, D. Shvydka, et.al., *J. Appl. Phys.* **96**, 7283 (2004).
- ⁴⁶ [http: //www.molec.com](http://www.molec.com)
- ⁴⁷ A. L. Efros and B. I. Shklovskii, *Electronic properties of doped semiconductors*, Springer-Verlag (1992).
- ⁴⁸ Reference on defect density of states in polycr. films.
- ⁴⁹ E. I. Levin, I. M. Ruzin, and B. I. Shklovskii. *Fiz. Tekh. Poluprovodn.* **22**, 642 (1988) [*Sov. Phys. Semicond.* **22**, 401 (1998)].
- ⁵⁰ B. I. Shklovskii, *Fiz. Techn. Poluprovodn.* **6**, 2355 (1972) [*Sov. Phys. Semicond.* **6**, 1964 (1972)].
- ⁵¹ reference describing rf sputtered cell recipe
- ⁵² Sh. Kogan, *Electronic Noise and Fluctuations in Solids*, Cambridge University Press, London

- 1996.
- ⁵³ W.Jaegermann, A.Klein, J.Fritsche, D.Kraft, B.Spth, Mater. Res. Soc. Symp. Proc., **865**, F6.1.1 (2005).
 - ⁵⁴ A.Y.Shik, Electronic Properties of Inhomogeneous Semiconductors, Gordon&Breach 1995
 - ⁵⁵ B. I. Shklovskii, Phys. Rev. B **67**, 045201 (2003).
 - ⁵⁶ V. I. Kozub, Solid State Commun. **97**, 843 (1996).
 - ⁵⁷ S. Lombardo, J. H. Stathis, and B. P. Linder, Phys. Rev. Lett., **90**, 167601 (2003).
 - ⁵⁸ T. J. McMahon, T. J. Berniard, and D. S. Albin, J. Appl. Phys., **97**, 054503 (2005).
 - ⁵⁹ Diana Shvydka, J. Drayton, A.D. Compaan, V.G. Karpov, "Piezo-effect and Physics of CdS-based Thin-film Photovoltaics", Appl. Phys. Lett. **87**, 123505 (2005).
 - ⁶⁰ F.A. Pizzarello, J. Appl. Phys. **38**, Issue 4, 1967, pp.1752-1755.
 - ⁶¹ M. L. C. Cooray and V. G. Karpov, Appl. Phys. Lett., **88**, 2005, pp. 093508-1-3.
 - ⁶² Murray S. Bennett and John J. Kramer, J. Appl. Phys. **54**, 1983, pp.7159-7165.
 - ⁶³ C.Z. Rosen, B.V. Hiremath and R .Newnham ed., "Piezoelectricity", AIP, New York, 1992.
 - ⁶⁴ D. Berlincourt, H. Jaffe and L.R. Shiozawa, Phys. Rev. **129**,1963, pp. 1009-1017.
 - ⁶⁵ L.D. Landau and E.M. Lifshitz, "Theory of Elasticity (course of theoretical physics; vol.7)", Butterworth-Heinemann, 1986.
 - ⁶⁶ Diana Shvydka, J. Drayton, M. Mitra, S.X. Marsillac, and F. Jacob, 2nd World PVSC proceedings, Hawaii, 2006.
 - ⁶⁷ Computational model provided by The Center for X-Ray Optics at Lawrence Berkeley National Laboratory, <http://www-cxro.lbl.gov>.
 - ⁶⁸ Xiangxin Liu, A.D. Compaan, N.Leyarovska, and J. Terry, Mat. Res. Soc. Symp. Proc. **763**, B3.5.1, (2003).
 - ⁶⁹ Xiangxin Liu, A.D. Compaan, Jeff Terry. , 2004 European MRS meeting, Strasbourg, Thin Solid Films **480-481**, pp. 95-98 (2005).
 - ⁷⁰ Xiangxin Liu, Ph.D. Thesis: "Photoluminescence and Extended X-ray Absorption Fine Structure Studies on CdTe Material", The University of Toledo, 2006.
 - ⁷¹ A. Ankudinov, B. Ravel, and J.J. Rehr, FEFF8, Version 8.20 (2002), The FEFF Project, Department of Physics, University of Washington.
 - ⁷² Takashi Abe, Yasube Kashiwaba, Mamoru Baba, Jun Imai, Hideyuki Sasaki, App. Surf. Sci., **175-176**, pp. 549-54 (2001).

⁷³ Ralph W. G. Wyckoff, *Crystal Structures* (John Wiley & Sons, New York, 1963), vol. 1, IV, pp. 333-334.

3. DEPOSITION RATE OF CDTE MAGNETRON SPUTTERING

3.1. Overview

Deposition rate is known to be a function of several variables (i. e. deposition pressure, substrate temperature, magnetron configuration, applied RF power, frequency, and signal shape, type of sputtering gas, etc.) in a multi-dimensional parameter space. As a consequence, a variety of material and cell properties such as film density, morphology, uniformity, cell performance and requirements for different types of post-deposition treatments may vary a great deal. In this study we kept all the variables but deposition pressure as tightly fixed as possible, focusing on pressure dependence of deposition rate, film structure and cell performance.

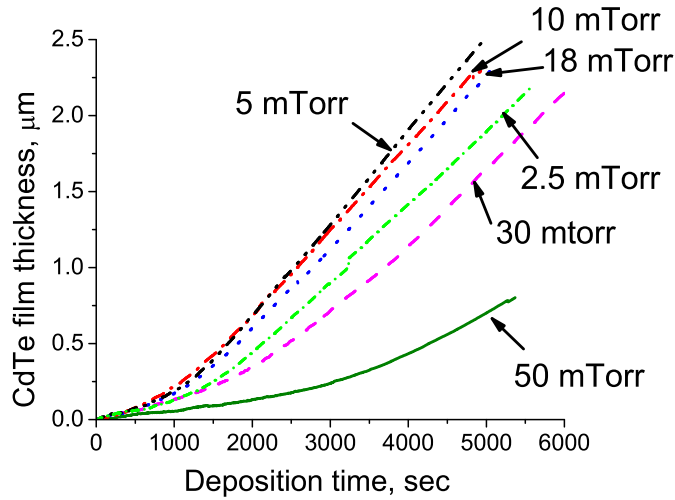


Figure 3.31: Nucleation and growth kinetics for CdTe films grown at different pressures.

3.2. Deposition rate vs. sputtering gas pressure

The deposition was done in a magnetron sputtering chamber, on a TEC-7 glass substrate at a temperature of about 250 °C, 20 W of power delivered to a CdTe target, with Ar as the sputtering gas at pressures ranging from 2.5 to 50 mTorr. A majority of the CdTe films were grown to the thickness in the range of 2 to 2.5 microns as a part of our standard TEC-7/CdS/CdTe/Au/Cu cell structure. CdTe film thickness was controlled in-situ by a

transmission monitor with He-Ne laser as a light source and Si photodiode as a detector. Typical nucleation and growth kinetics curves for different pressures are shown in Fig. 3.31.

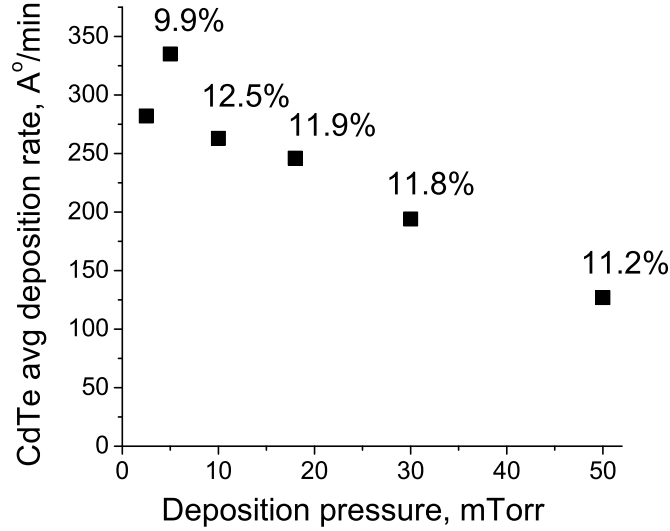


Figure 3.32: Average CdTe deposition rate and the corresponding highest cell efficiency at different pressures.

Deposition pressure, mTorr	Average deposition rate, Å/min	Best cell efficiency, %
50	127	11.2
30	194	11.8
18	246	11.9
10	263	12.5
5	335	9.9
2.5	282	N/A

Table 3.2: Average CdTe deposition rate and corresponding highest cell efficiency at different pressures.

The traces of Fig. 3.31 show a nonlinear slope vs. time but this does not necessarily indicate nonlinear growth kinetics since below about $0.2 \mu\text{m}$ the transmission depends on the multilayer interferences in the stack of thin CdTe/CdS/TCO layers. The nucleation and coalescence phase certainly dominates the initial stage of the deposition, and spectroscopic

ellipsometry provides detailed information on this aspect of growth. (See Section 5 of this report).

The final thickness of the each film grown was measured independently with a DEKTAK profilometer and was found to be in a good agreement with the transmission monitor data. The results of these measurements are summarized in the Fig. 3.32 and Table 3.2. The average growth rate was estimated for the film thickness of 2.3 microns at each pressure. The general trend here is that the deposition rate increases when pressure decreases allowing a greater mean free path. This remains until pressure reaches its lowest limit for the system when plasma becomes somewhat unstable. Thus the datum point for 2.5 mT may be low because of some instability in the plasma power.

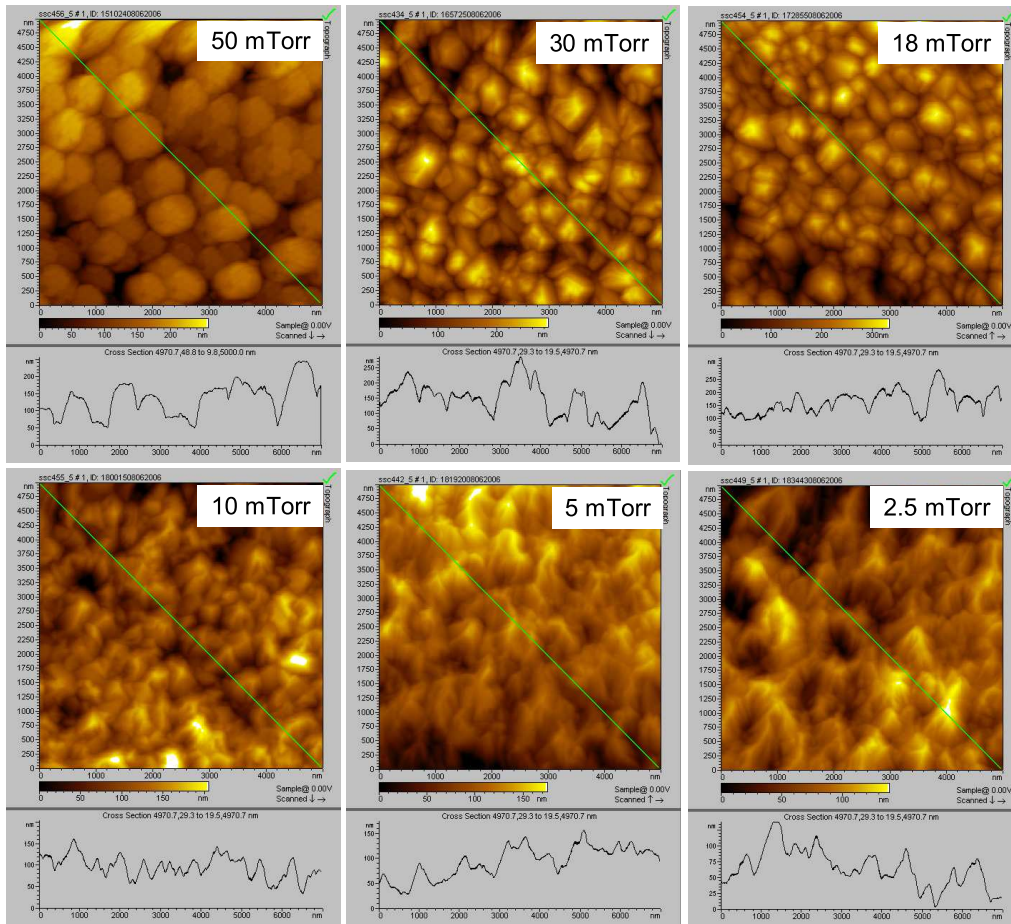


Figure 3.33: In-plane AFM images and corresponding cross sections of as-grown CdTe films deposited at different pressures.

The highest cell efficiency obtained for each gas pressure is also shown in the Fig. 3.32

and Table 3.2. At this stage our highest deposition rate pressure (5 mTorr) differs from the value at which we obtained the best cell efficiency (10 mTorr). However, so far we have not done any optimization of post-deposition treatment parameters, such as, for example, CdCl_2 treatment time and temperature. The necessity of this optimization is supported by the AFM images of the films, shown on Fig. 3.33. It is clear that films undergo a significant morphology change as the pressure varies from 50 to 2.5 mTorr. In particular, we observe a reduction of the grain size as the pressure goes down and deposition rates increases. Therefore the optimum post-deposition treatment parameters may vary for the films of the same thickness but grown at different pressures. We believe that films grown at lower pressure and correspondingly higher deposition rate may achieve the efficiency comparable to our conventional devices, typically grown at pressure of 30 or 18 mTorr.

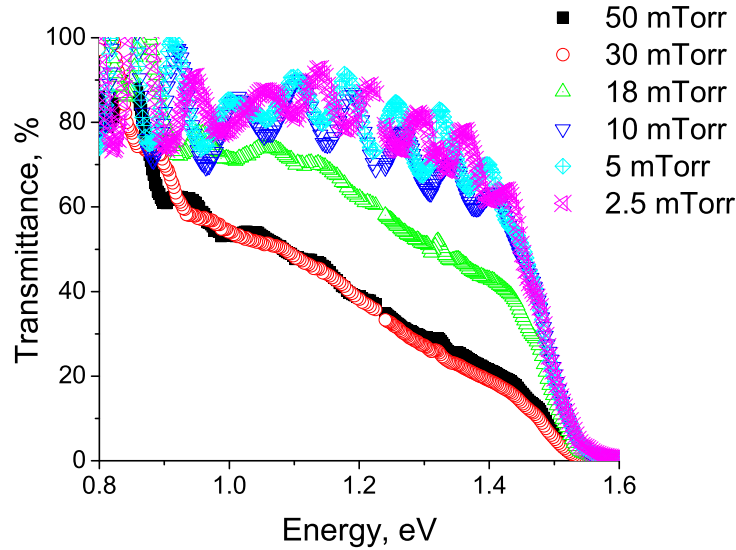


Figure 3.34: Transmittance of CdTe films grown at different pressures.

Reduction in grain size and surface roughness for the films grown at lower pressures (Fig. 3.33) is in a good agreement with the general physical appearance of the films (dull if grown at pressure higher than 18 mTorr and very shiny, almost mirror-like otherwise) as well as the transmission data, shown in Fig. 3.34. In this figure a higher transmission of the films grown at a reduced pressure is due to the smoother surface that such deposition conditions imply, which is clear from AFM cross sections above, and corresponding lowering of the scattering losses on these interface, which can be also concluded from the presence or absence of the interference fringes from the films of roughly the same thickness (about

2.3 micron) in the Fig. 3.34. It seems that there is a transition region in pressure of about 15-20 mTorr when thin film morphology undergoes a significant change which influences some of its optical and, possibly, electrical properties, but does not dramatically affect the performance of the completed cell as follows from the Table 3.2. We should note, that improved transmission of such films can be utilized in a tandem cell devices if the film serves as an absorber of the top cell, allowing more light to penetrate to the bottom cell.

Another possible application of this study, currently being investigated, is for ultrathin (less than 1 micron CdTe) CdS/CdTe cell structures which may benefit from better micro-scale uniformity of films deposited at lower pressure (see Fig. 3.33). We found no evidence of changes in thickness uniformity on a macro-scale that depend on rf power. Shown in Fig. 3.35 are thickness maps, obtained with DEKTAK profilometer, that confirm that films grown at different pressure are almost equivalent in terms of thickness uniformity.

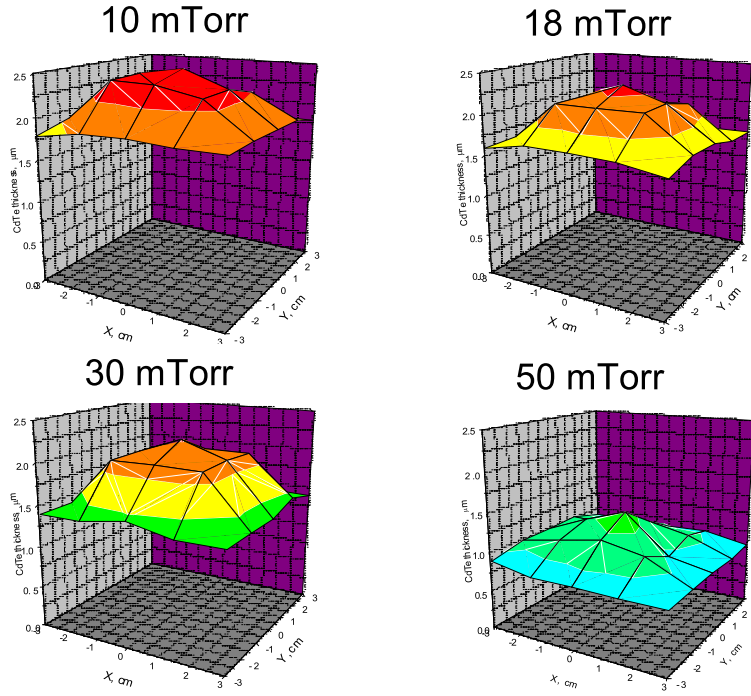


Figure 3.35: Film thickness map measured by DEKTAK profilometer.

3.3. Conclusions

We have investigated the dependence of sputtering gas pressure on the deposition rate and found that the average CdTe deposition rate increases by about a factor of 2.5 as pressure decreases from 50 mTorr to 2.5 mTorr. Increase in the deposition rate results in change of film surface morphology, as well as some of the optical properties. However, it has been demonstrated that reasonably high efficiency cells can be fabricated over a broad range of pressure even without optimizing a post-deposition treatment conditions. During the next phase of the contract we will continue this work and study the deposition rate dependence on other parameters, such as substrate temperature, delivered RF power and magnetron configuration.

4. THIN CDTE DEVICES

4.1. Overview

The main purpose of this activity is to investigate the limits of thickness reduction of CdTe using rf magnetron sputtering in order to reduce Te shortage issues and add to the economic attractiveness of the sputtering method. In addition, thin CdTe devices offer significant above-band gap transparency and therefore could be used in tandem structures as the top cells.

4.2. Device fabrication and J-V analysis

During the first year of the contract we have fabricated a set of CdS/CdTe devices with CdTe thickness varying from $0.45\ \mu\text{m}$ up to $2.4\ \mu\text{m}$, on 3mm thick $\text{SnO}_2\text{:F}$ coated soda-lime glass. These devices were fabricated at deposition pressure of 30 mtorr in Ar gas, using RF power of 35 watts for CdS and 20 watts for CdTe. Depositions were carried out at substrate temperature of $\sim 250\ ^\circ\text{C}$. As the next step in cell fabrication we carried out vapor CdCl_2 treatment at $387\ ^\circ\text{C}$. To avoid over-treatment of thinner devices we had to optimize (reduce) the treatment time, keeping the temperature fixed. Cells were finished with evaporated Cu-Au back contacts, followed by heat treatment at $150\ ^\circ\text{C}$ in air. At this stage we also had to reduce the treatment time for thinner devices in order to prevent diffusion of excessive amount of Cu into the device. We summarize post-deposition treatment parameters in Table 4.3 for devices with varying CdTe layer thickness.

We performed optical characterization of samples (Tec7/CdS/CdTe) with different thickness of CdTe by measuring the line of sight transmission with a uv-visible spectrophotometer before and after the CdCl_2 treatment (Fig. 4.36(a) and (b)). CdCl_2 treated structures show a sharpening of absorption edge indicating a well-defined band gap for the absorber layer.

Current-voltage (J-V) measurements on these cells were carried out with an AM 1.5 spectrum under one sun illumination. Table 4.4 shows average J-V parameters for cells with different thickness of CdTe. Here the yield was calculated as a ratio of the number of cells with non-zero efficiency (not shunted) to the total number of cells on a substrate. Table 4.5 shows the performance of the best cell for each of those thicknesses. (This extends an earlier study by A. Gupta¹). We have achieved more than 10% efficiency for cells with only

Thickness of CdTe (sample ID)	CdCl ₂ tr. Time (mins)	Thickness of Cu (Å)	Diff. time (min)
0.45 (340)	7	30	5
0.69 (341)	10	20	5
0.90 (351)	15	18	15
1.56 (343)	22	22	35
2.40 (344)	30	40	45

Table 4.3: Variation in post-deposition treatment parameters for devices of varying CdTe thickness. Numbers in the parenthesis in the first column are the sample ID's. Less Cu was used with thinner CdTe, but fluctuations occurred due to slow response of evaporator boat temperature.

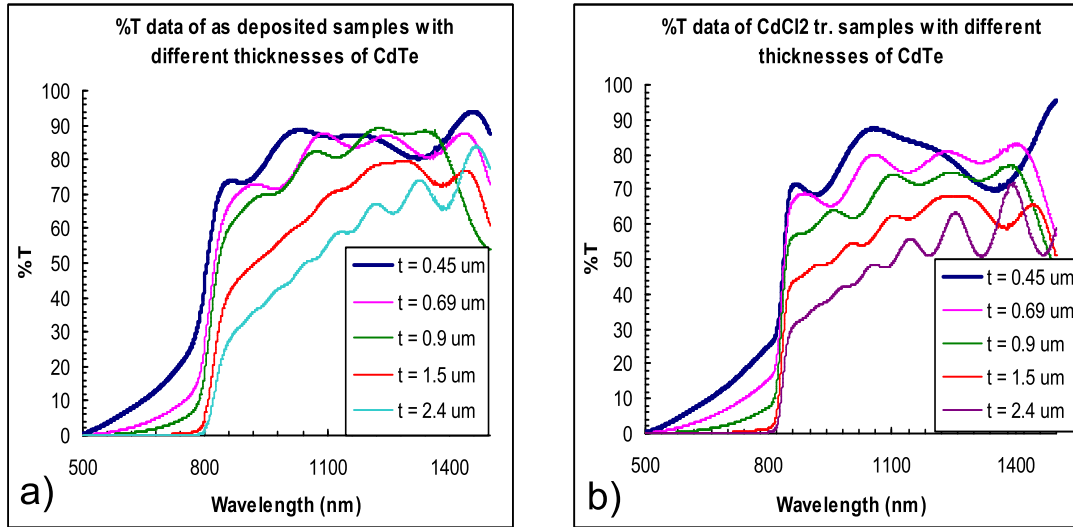


Figure 4.36: Line of sight transmission data of samples (Tec7/CdS/CdTe) with varying thickness of CdTe before (a) and after (b) CdCl₂ treatment. Thickness of CdS is kept the same.

0.69 μm thick CdTe and above 12% for cells with CdTe thickness less than 1 μm . The drop in efficiency with decrease in thickness is mainly due to the decrease in open-circuit voltage. Short-circuit current and fill factor does not seem to change much with thickness.

One of the important points worth noting is that the percentage yield does not change significantly even for samples with thinner CdTe. This shows that the rf sputtering technique is well suited for fabrication of CdS/CdTe solar cells with thinner absorber layer.

Numbers of cells (sample ID)	Thickness (μm)	Ave. V_{oc} (mV)	Ave. J_{sc} (mA/cm ²)	Ave. FF (%)	Ave. Eff. (%)	Yield (%)
22 of 24 cells (340)	0.45	476 \pm 147	17.4 \pm 1.5	45 \pm 13	4.2 \pm 2.5	91
25 of 30 cells (341)	0.69	607 \pm 107	19.8 \pm 1.5	60 \pm 12	7.6 \pm 2.6	83
29 of 42 cells (351)	0.90	675 \pm 89	22.0 \pm 1.0	62 \pm 13	9.6 \pm 2.6	69
23 of 32 cells (343)	1.56	742 \pm 155	21.9 \pm 2.2	63 \pm 15	10.8 \pm 3.0	71
32 of 36 cells (344)	2.04	794 \pm 54	21.5 \pm 2.3	64 \pm 9	11.1 \pm 2.4	88

Table 4.4: Average J-V parameters for devices with different CdTe layer thickness.

Thickness (μm)	V_{oc} (mV)	J_{sc} (mA/cm ²)	FF (%)	Eff. (%)
0.45	655	19.66	62.37	8.03
0.69	702	21.04	69.85	10.32
0.90	758	22.58	70.98	12.15
1.56	797	22.50	68.84	12.34
2.40	825	22.58	66.37	12.36

Table 4.5: Best cell performance for each CdTe thickness.

4.3. SEM studies of CdTe devices with varying absorber thickness

Fig. 4.38 shows the comparison between SEM micrographs of Tec7/CdS/CdTe structure before (upper row) and after the CdCl₂ treatment (lower row) for devices of three different absorber thickness. Both CdS and CdTe are grown at deposition pressure of 30 mtorr and substrate temperature of ~ 250 °C. Calculation of grain size for as deposited sample shows that samples with thinner CdTe exhibit smaller grain size, while the samples with thicker CdTe exhibit a larger grain size (table 4.6). Grain size is calculated by dividing the length of the line drawn across the SEM micrograph by the number of grains intersected by the line and is averaged over 3 measurements.

SEM micrographs of the CdCl₂ treated samples show areas with higher secondary electron emissivity which typically indicate chlorine containing compounds that seems to have been left after the treatment. We have not done any surface conditioning to remove the residual

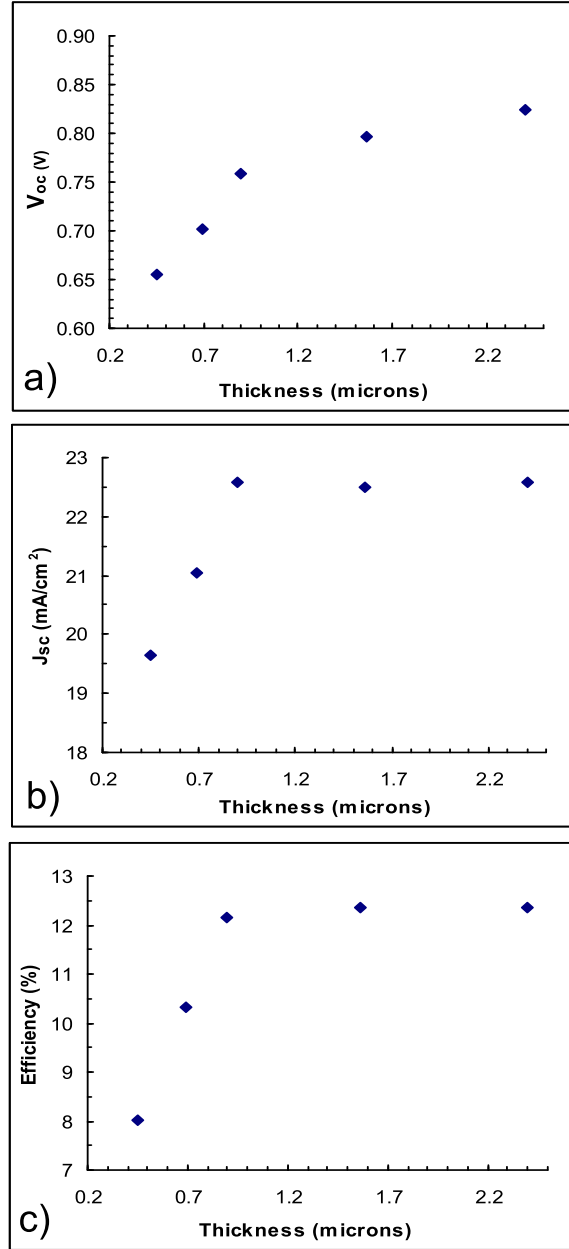


Figure 4.37: Graphical representation of the J-V parameters for the best cells.

CdCl_2 before depositing the Cu-Au back contact. Comparison of SEM images of as-deposited versus CdCl_2 treated samples shows a clear evidence of recrystallization of CdTe in the CdCl_2 treated samples. In particular, table 4.6 shows that the average grain size increases for as-deposited thicker CdTe films. At the same time after CdCl_2 treatment samples seem to be hardly distinguishable from each other, suggesting that we should not anticipate problems with thinner CdTe devices, directly related to the absorber film quality.

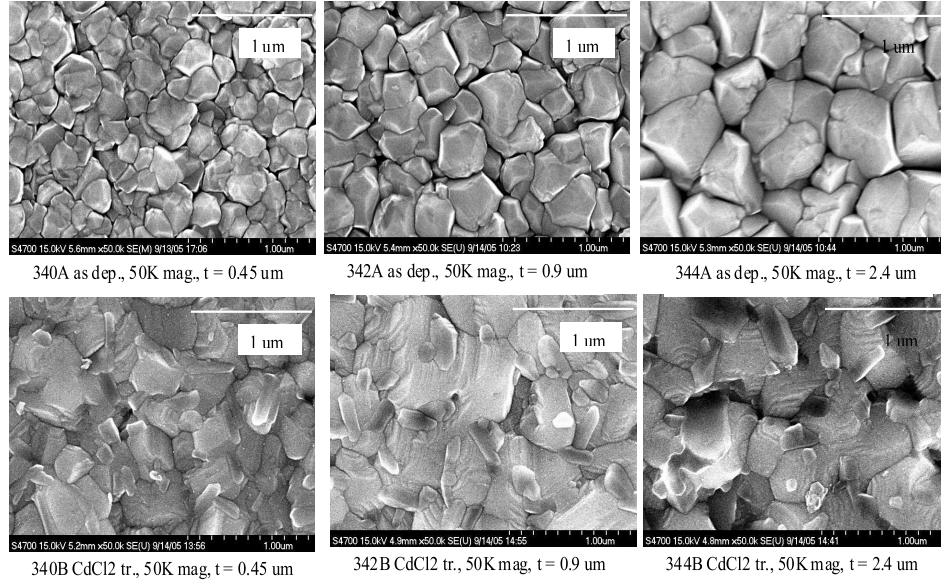


Figure 4.38: SEM micrographs of Tec7/CdS/CdTe surface before and after the CdCl_2 treatment for devices of 3 different absorber thickness.

Thickness of CdTe (μm)	Grain size before CdCl_2 (nm)	Grain size after CdCl_2 (nm)
0.45	194	360
0.69	194	500
0.90	253	500
1.56	316	500
2.40	361	500

Table 4.6: Grain size distribution for samples with different thickness of CdTe before and after CdCl_2 treatment.

In conclusion, we have obtained very encouraging results for solar cells fabricated with CdTe absorber layer as thin as $0.5 \mu\text{m}$. However, more work needs to be done to ensure good reproducibility for thinner devices.

References

- ¹ A.Gupta, V. Parikh, A.D. Compaan, Solar Energy Materials and Solar Cells, **90**, 2263-2271 (2006).

5. REAL TIME SPECTROSCOPIC ELLIPSOMETRY (RTSE) OF CDTE MATERIALS AND SOLAR CELLS

5.1. Overview

In the development of RTSE as probe for CdTe solar cell optimization, a step-by-step research program is being undertaken in order to separate out the complexities that occur in the fabrication process and appear in the experimental RTSE data. It is important to characterize these complexities first under ideal conditions chosen for high sensitivity. In this way, dielectric function databases can be established that enable a complete real time analysis in the actual solar cell structure – which may be less than ideal in terms of sensitivity, typically due to substrate surface roughness that propagates throughout the structure. The results of such analyses can then be applied to optimize solar cell performance based on a better understanding of the overall fabrication process including both deposition and post-deposition treatments. The following lists the strategy being applied:

(1) CdTe growth on ultrasmooth c-Si substrates held at different temperatures. Such depositions avoid substrate-induced roughness, and as a result, the smoothest film surfaces occur after the nucleation and coalescence processes. Under these circumstances, the dielectric functions of the growing CdTe film can be determined with the greatest accuracy and precision. From the dielectric functions, characteristics of the film can be extracted such as temperature, film stress, and grain size or defect density.

(2) CdS growth on ultrasmooth c-Si substrates held at different temperatures. The motivation for these studies is the same as that for CdTe growth. Again, the goal is to extract the dielectric functions of the CdS with the greatest confidence. The added feature that may be possible to determine from the dielectric function of CdS is the degree of preferential orientation of the c-axis relative to the film normal. This can be obtained because the stable phase of CdS is hexagonal, and thus optically uniaxial with different dielectric functions for optical electric field directions parallel (extraordinary) and perpendicular (ordinary) to the c-axis.

(3) CdS/CdTe growth on ultrasmooth c-Si with film thickness and temperature control. The motivation for these studies is to develop a dielectric function database versus measurement temperature for the full metastable compositional range of $\text{CdTe}_{1-x}\text{S}_x$, as well as for

the equilibrium compositions achieved by annealing the deposited sample to a temperature within the range up to the CdCl_2 treatment temperature. By controlling the ratio of the CdS:CdTe thicknesses as well as the processing temperature profile, single phase films of the desired composition can be obtained. The ultimate goal is to establish the compositional evolution during interface formation in the solar cell configuration using the dielectric function database obtained in this study.

(4) CdS/CdTe growth on ZnO-coated alumino-silicate glass under different deposition conditions for the CdS and CdTe. This structure includes the complication of substrate-induced surface roughness that is to be avoided in studies (1)-(3). This roughness propagates throughout the entire structure, weakening sensitivity to interface effects. The motivation for this set of studies is to correlate the process conditions, e.g., substrate temperature, Ar pressure, plasma power, dc substrate bias, with the RTSE-deduced structural evolution and optical properties as well as with the ultimate solar cell performance. The final goal is to use this information to optimize the solar cell fabrication process based on an improved understanding of the process, rather than by trial and error.

(5) Post process treatments of films and device structures. At each step (1)-(4), it is important to establish the effects of post-deposition treatments including both thermal annealing and CdCl_2 treatments on the thin film or device structures. Post-processing can influence both the film structure and optical properties, and the goal is to explore the role of the key parameters of process temperature and time. Real time studies of these post-processing treatments are of interest; however, due to the complexity of the final film or device to be studied, a more effective approach is a bromine-methanol etch-back procedure that enables depth profiling. This procedure allows one to perform (real time)-reversed spectroscopic ellipsometry while maintaining a smooth surface as the layers of the structure are etched away.

In research undertaken thus far, the experiments have been completed for Steps (1)-(3), data analysis has been completed for Step (1), and data analysis is in progress for steps (2) and (3). In addition, upon development of the time-reversed measurement approach, initial studies in Step (5) have been performed as well. This review reports results for Step (1) and progress made so far in Steps (2) and (5).^{1,2}

5.2. Experimental Details

The polycrystalline CdTe and CdS films of this study were magnetron sputtered under conditions similar to those yielding 14%-efficient solar cells.³ The CdTe depositions were performed on native oxide-covered c-Si wafers using 60 W rf power at the target, 18 mTorr Ar pressure, 23 sccm Ar flow, and 10 cm target-substrate distance. The CdS depositions were performed similarly with the exception of a rf power level of 50 W and an Ar pressure of 10 mTorr. Si substrates were used in both cases due to their consistency and smoothness; thus, complications in optical analysis arising from substrate-induced surface roughness are avoided as described in the previous section. Deposition temperature T was the key process variable, but calibration was difficult due to the substrate holder geometry. Because the substrate holder was designed to rotate, the thermocouple for substrate temperature measurement was located in the heating assembly well away from the substrate (see Fig. 5.39). As a result, it was necessary to calibrate substrate temperature from RTSE. This was done using the CdTe E_0 band gap shifts that occur upon cooling the deposited film to 15°C (and also reheating to T as a check). For accuracy, this sequence was performed upon suspending the deposition after ~ 1000 Å. At this thickness, the film is relatively uniform and smooth, and thus, the optical properties can be extracted with high accuracy. The details of the substrate temperature calibration appear below.

The rotating-compensator multichannel ellipsometer used here is similar to that developed to study Si:H-based solar cells.^{4,5} The instrument provides spectra (0.75 to 6.5 eV) in (ψ, Δ) as an average over a minimum of two optical cycles each lasting 32 ms. Here, the spectra were collected in times from 1 to 3 s, as averages over ~ 30 to 90 optical cycle pairs. During the maximum acquisition time for one set of (ψ, Δ) spectra, effective CdTe and CdS thicknesses of less than a monolayer (i.e., < 3 Å) accumulate at the typical deposition rates (~ 0.9 and 0.7 Å/s, resp.). The angle of incidence for these depositions was in the range of 65.3-65.9°. Analyses of all spectra apply numerical inversion and least-squares regression algorithms.

5.3. Results and Discussion: RTSE Studies of CdTe Deposition

Surface roughness evolution

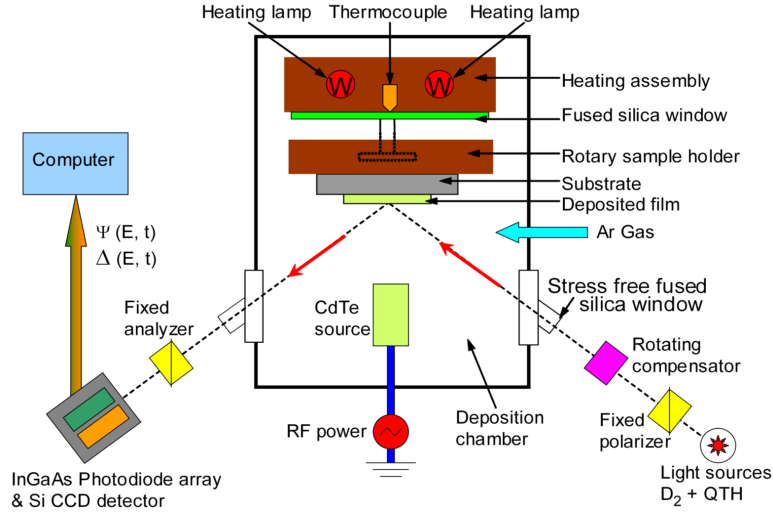


Figure 5.39: Schematic of deposition system and associated instrumentation for RTSE studies of CdTe and CdS growth by magnetron sputtering.

Figure 5.40 depicts the time evolution of the surface roughness layer thickness d_s for a series of five CdTe films magnetron sputtered at $T=188, 215, 237, 267$, and 304°C , under otherwise identical conditions. For the roughness layer thickness d_s in the initial 500 \AA of bulk layer thickness d_b in Fig. 5.40, (ψ, Δ) spectra were analyzed over their full range ($0.75 - 6.5 \text{ eV}$) using a two-layer [bulk/roughness] model for the CdTe film.⁶ For $500 < d_b < 1000 \text{ \AA}$, a second bulk layer with increased void volume fraction was added on top of the denser underlying bulk layer ($\sim 500 \text{ \AA}$ thick) in order to maintain the quality of the fit to the RTSE data close to that achieved when $d_b < 500 \text{ \AA}$. For the evolution of d_s when $d_b > 1100 \text{ \AA}$ in the right side of Fig. 5.40, the (ψ, Δ) spectra were analyzed from 3.5 to 6.5 eV where the CdTe film is opaque and high surface sensitivity is attained. This latter analysis uses a one-layer model [(semi-infinite bulk)/roughness] that avoids the complicated underlying structure. Plotted along the abscissa, d_b is obtained in an analysis that uses the full multilayer model (see next sub-section).

A closer look at the initial nucleation stages is provided in Figure 5.41. Considering the results for $T=188, 215$, and 237°C , the surface roughness thickness in this case describes the nuclei height above the substrate⁶. This thickness increases to $18\text{-}22 \text{ \AA}$ before the first bulk monolayer forms, an indication of clustering from the outset, or the Vollmer-Weber (V-W)

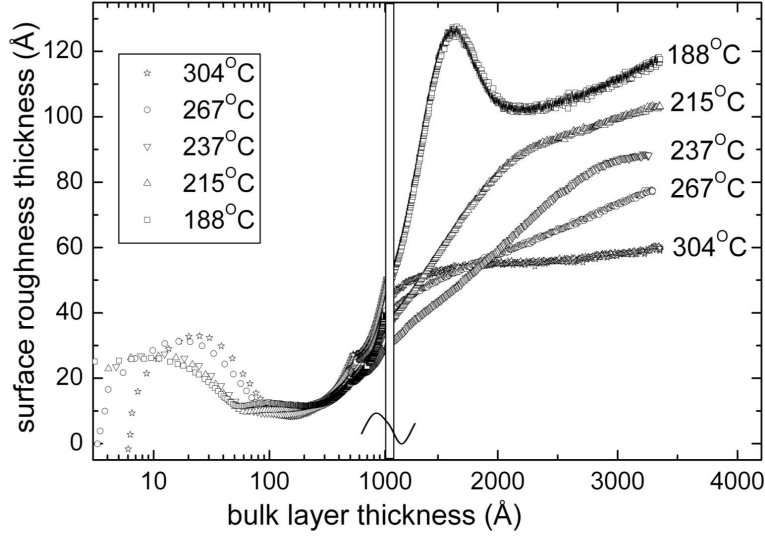


Figure 5.40: Evolution of the surface roughness layer thickness versus the bulk layer thickness deduced from RTSE data acquired during the growth of CdTe films on native oxide covered c-Si substrates at different temperatures. The results at the left ($d_b < 1000$ Å) and right ($d_b > 1100$ Å) were obtained from analyses of the full spectra (0.75 - 6.5 eV) and the high energy range (3.5 - 6.5 eV), respectively. The nucleation regime for these films is highlighted in Fig. 5.41.

growth mode. For the two higher temperatures of 267 and 304°C, bulk layers of 3 and 6 Å (1 and 2 monolayers) form on the substrate before the onset of clustering; then clustering occurs abruptly leading to roughness layer thicknesses as large as 33 Å. Such behavior is clear evidence of the Stranski-Krastanov (S-K) growth mode in which case $\gamma_f + \gamma^*$, the sum of the free energies of the film surface and substrate/film interface increases from a value slightly less than γ_s , the substrate surface free energy, to a value greater than γ_s upon growth of one or two monolayers.⁶ This change may be due to the build-up of strain in the monolayer(s). Figure 5.42 shows the cluster parameters as a function of substrate temperature. These include the surface roughness thickness at its maximum (top curve), which is interpreted as the height of the clusters at the onset of coalescence. The increased nuclei height with increasing temperature is attributed to a decreased density of clusters on the surface; thus, clusters reach a larger size before contact and coalescence. The decreased cluster nucleation density is attributed to a longer diffusion length of film precursor atoms

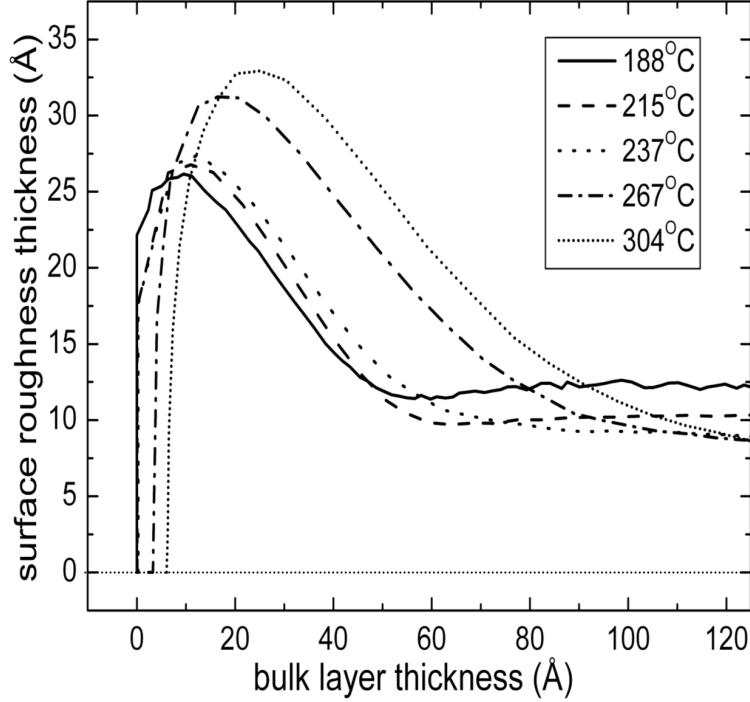


Figure 5.41: The nucleation and coalescence stages of CdTe deposition at different temperatures (T). When $T \leq 237^\circ\text{C}$, clusters reach $\sim 18\text{--}22$ Å in height before the first bulk layer forms; thus, growth follows the Volmer-Weber mode. When $T \geq 267^\circ\text{C}$, the bulk layer grows by one or two monolayers before clustering occurs; thus, growth follows the Stranski-Krastanov mode. Both the peak height of the clusters and the bulk layer thickness at this peak increase monotonically with increasing T . (See Fig. 5.42 for these trends.).

and molecules on the substrate (lower T) and film (higher T) surfaces which, in turn, leads to a larger capture radius for critical nuclei. The second parameter shown in Fig. 5.42 is the bulk layer thickness at the surface roughness maximum. The results in this case indicate a trend from V-W type growth to S-K type growth with increasing temperature.

After reaching peak thicknesses of $26\text{--}33$ Å, the clusters in both the immediate (V-W) and delayed (S-K) nucleation processes coalesce, leaving stable surface roughness layers $\sim 9\text{--}12$ Å thick. After a bulk layer thickness of ~ 200 Å, a roughening transition is observed with the strongest effect for the lowest deposition temperatures (see Fig. 5.40). At the end of the deposition at $d_b \sim 3300$ Å, the surface roughness layer thickness is observed

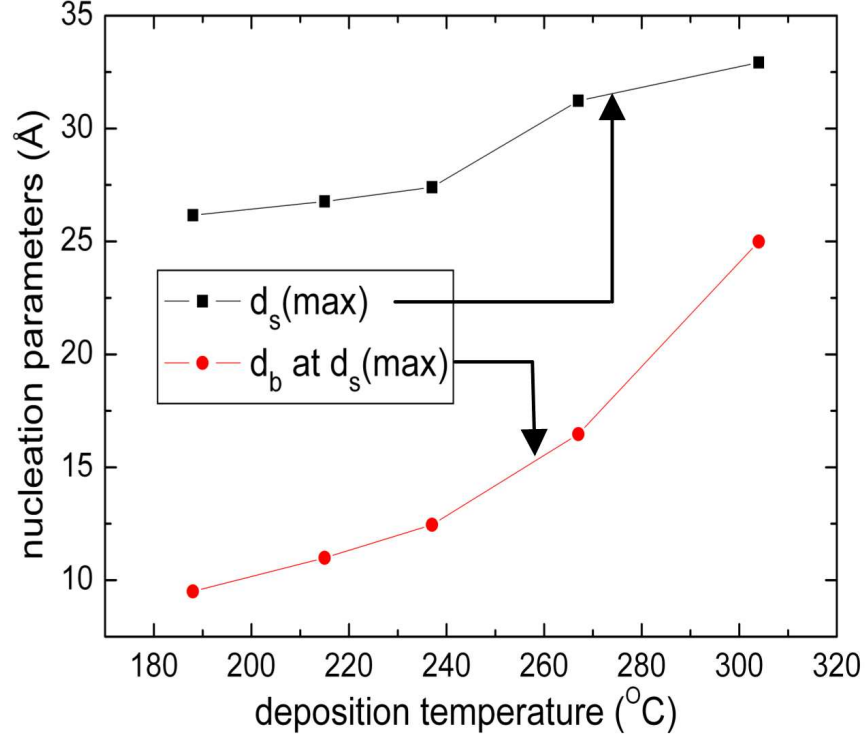


Figure 5.42: Parameters that describe the clustering in the initial stages of CdTe deposition. The quantity $d_s(\text{max})$ is the maximum value of the surface roughness layer thickness that describes the height of the initial clusters above the film surface. Also shown is the bulk layer thickness d_b obtained at the surface roughness maximum. This is a measure of the tendency toward S-K growth behavior over V-W behavior.

to decrease monotonically with increasing substrate temperature as shown in Fig. 5.43. This observation is likely due to enhanced diffusion of the film precursors on the surface at elevated temperatures. In fact, for the lowest temperature of $T=188^\circ\text{C}$, the roughness passes through an instability near 1500 \AA that is correlated with the rapid development of voids. Thus, as strain is relieved through void formation, the surface passes through a smoothening transition (see Fig. 5.40). Further discussion of the void fraction and its correlation with surface roughness evolution appears in the next sub-section.

Void volume fraction evolution

Depth profiles in the void volume fraction f_v are shown in Fig. 5.44 for the films of Figs.

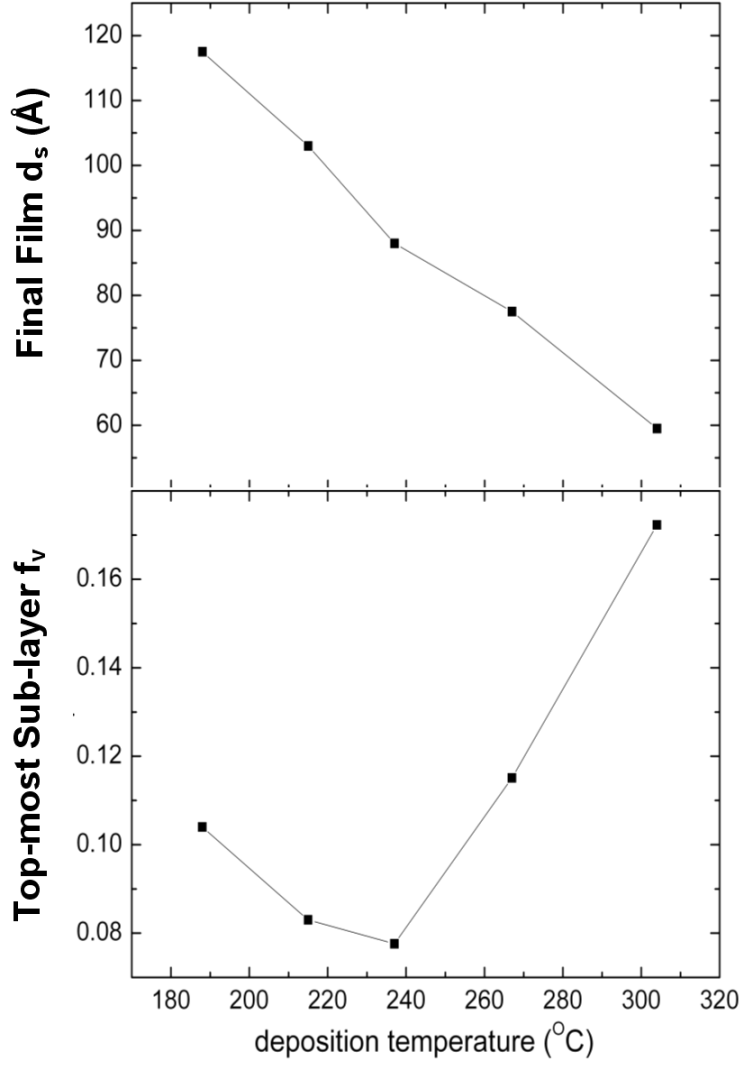


Figure 5.43: Surface roughness layer thickness at the end of CdTe film deposition to a bulk layer thickness of ~ 3300 Å, plotted as a function of the deposition temperature (top); also shown is the void volume fraction in the top-most sub-(bulk layer) of the final film (bottom).

5.40-5.43. These results are deduced from n-bulk layer optical models in which each sub-(bulk layer) thickness d_i ($i=1, \dots, n$), void volume fraction $f_{v,i}$, and surface roughness layer thickness d_s are chosen to ensure a best fit of RTSE data versus photon energy (0.75 - 6.5 eV) and time. The dense CdTe reference dielectric function for each film is taken to be that of the first sub-(bulk layer). Then the void fraction for that dense phase is scaled relative to the highest density sample prepared at 188°C. Figure 5.45 exemplifies the model used

to analyze the RTSE data for the film deposited at $T=215^\circ\text{C}$, spanning the full bulk layer thickness range of $1100 < d_b < 2100 \text{ \AA}$ [see Fig. 5.44(left)]. Here all parameters associated with the first and second sub-(bulk layers) are fixed to previously-determined values; only the third such layer parameters are free in the fitting routine, including the time-dependent sub-(bulk layer) and surface roughness thicknesses d_3 and d_s , and the time-independent sub-(bulk layer) void volume fraction $f_{v,3}$. As the film evolves, up to $n=6$ sub-(bulk layers) are needed to maintain a suitable fit to the RTSE data. For all deposition temperatures, f_v increases monotonically with increasing bulk layer thickness.

The evolution of f_v in Fig. 5.44 is found to exhibit interesting trends with T . Within the thin film regime ($d_b < 500 \text{ \AA}$), f_v increases monotonically with increasing temperature. The lowest T film having the lowest f_v value in the initial stages, however, exhibits an abrupt structural transition for $d_b > 1300 \text{ \AA}$; this yields a final film with near-surface $f_v \sim 0.10$. This transition is suppressed with increasing T (in conjunction with the incorporation of voids in the thin film regime). For CdTe films deposited at $T > 267^\circ\text{C}$, the depth profiles of f_v are nearly linear. The low temperature structural transition is attributed to the relaxation of strain; the strain appears to be enhanced under low surface diffusion, low f_v conditions. The void volume fraction in the top-most layer of the final film is shown as a function of the deposition temperature in Fig. 5.43. The highest density in the near-surface region of the final film ($\sim 3300 \text{ \AA}$) is obtained at $T \sim 230^\circ\text{C}$. Here the structural transition is avoided, while f_v induced in the thin film regime with increasing T is minimized in a trade-off. The deposition temperature yielding the minimum void fraction in the final film surface approximates that for optimum solar cell performance.

As noted in the previous section, there is a clear correlation between the surface roughness thickness and void fraction evolution. It is reasonable that both surface roughness and voids provide means for strain relief in the films. For the lower T films of lowest void fraction in the thin film regime, the roughening transition starting near $d_b \sim 200 \text{ \AA}$ is enhanced, leading to significant roughness thicknesses in the thick film regime. As these films undergo their structural transitions to higher void fraction (which are centered near $d_b=1500 \text{ \AA}$ for $T=188^\circ\text{C}$, $d_b=2700 \text{ \AA}$ for $T=215^\circ\text{C}$, and $d_b \sim 3000 \text{ \AA}$ for $T=237^\circ\text{C}$), the roughness layer thicknesses begin to stabilize. In fact, for the $T=188^\circ\text{C}$ film, the structural transition is accompanied by a surface smoothening effect (Fig. 5.40); clearly higher bulk layer void fractions permit smoother surfaces.

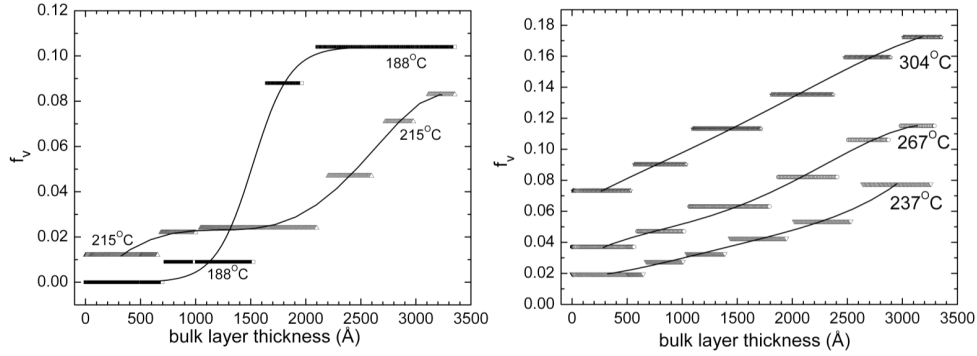


Figure 5.44: Stepwise depth profiles in the relative void volume fraction for five depositions of CdTe prepared by magnetron sputtering onto native oxide covered c-Si substrates at temperatures of 188 and 215°C (left), and 237, 267, and 304°C (right).

Deposition rate

Once the complete structural evolution is obtained, combining both the surface roughness and void fraction evolution, different measures of the deposition rate can be determined and compared. The effective thickness is defined as the product of the CdTe volume fraction and film thickness summed over the multiple layers of the structure. The volume fraction is scaled to unity for the lowest void fraction CdTe thin film material – which is the material obtained in the thin film regime ($d_b < 500$ Å) at the lowest deposition temperature of $T=188^\circ\text{C}$ (see Fig. 5.44). Thus, the effective thickness is the thickness obtained if all the material within the film were compressed into a single smooth layer with the same void fraction as this highest density material (which in fact could be higher in density than the single crystal due to strain). Then the effective deposition rate is obtained as a linear fit of the effective thickness versus time over the entire deposition. It should be noted that if one were to multiply the effective deposition rate by the mass density of the densest material, the result would be mass per (area x time), the same result that would be returned if thickness monitoring were performed with a crystal quartz oscillator.

Figure 5.46 depicts the effective deposition rate for the series of five CdTe films magnetron sputtered at $T=188, 215, 237, 267,$ and 304°C , under otherwise identical conditions. The error bars result from the variations in rate measured over different time ranges during the

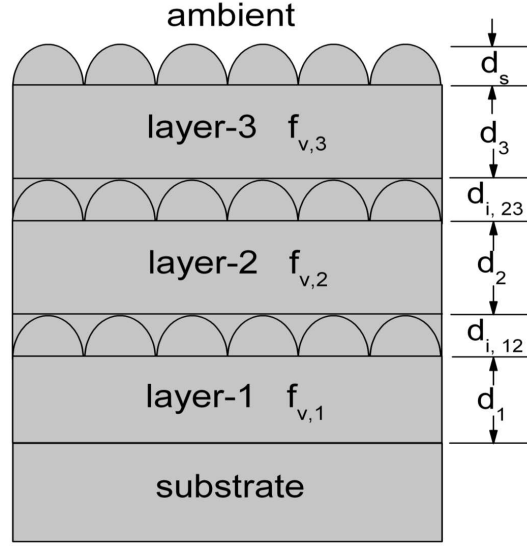


Figure 5.45: Optical model used to simulate the film structure for the CdTe film deposited at 215°C when $1100 < d_b < 2100$ Å. The best f_v value in the third layer (~ 0.025) was found so that the evolving values of d_3 and d_s generated the best fit within this range of thickness.

deposition process such as in Fig. 5.47. An increase in rate with increasing deposition temperature is apparent in Fig. 5.46, a trend that is outside the limits of the error bars. The increase in rate appears counterintuitive since the sticking probability – if it did vary with temperature – is expected to decrease with increasing T . The increase in rate, however, appears attributable to a reduction in Ar atom density with the increase in gas temperature at constant pressure and volume. A similar decrease in rate occurs with an increase in pressure at constant temperature. Figure 5.47 depicts the average rate at different stages of the growth process for the lowest temperature CdTe deposition, as an example, expressed in terms of the bulk layer thickness and effective deposition rates. The rapid increase in the bulk layer growth rate centered at $t=50$ min is attributed to the structural transition; when the void fraction in the growing bulk of the film increases, the physical thickness rate increases at constant incident flux of film precursors. It is clear that accounting for the development of voids, as is done by extracting the effective rate, suppresses the increase in growth rate; however, a weaker linear increase in effective rate remains. Such a trend is observed for the other depositions as well. The origin of this increase remains unclear; it may possibly be due to long-term thermal equilibration of the system.

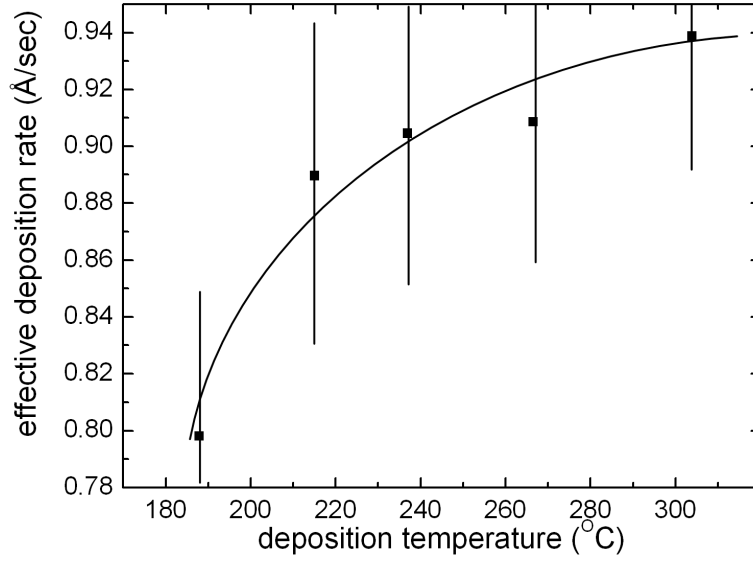


Figure 5.46: Effective deposition rate as a function of deposition temperature for five CdTe films prepared by magnetron sputtering onto native oxide covered c-Si substrates at temperatures of 188, 215, 237, 267, and 304°C. The effective deposition rate is the product of the layer thickness and the CdTe volume fraction ($1-f_v$) summed over all layers of the structure.

Optical functions: General discussion

In this study, (ψ, Δ) spectra were collected at 15°C for each sample after the cooling step of a cooling-reheating cycle that was performed upon suspending the deposition at $d_b \sim 1000$ Å. Thus, in the determination of the dielectric functions (ϵ_1, ϵ_2) of these films, the large variations in void fraction with depth throughout the films were avoided for the most part. Each (ψ, Δ) pair of spectra at 15°C can be inverted exactly to extract the dielectric function of each deposited CdTe film in a process that requires the known substrate ($\text{SiO}_2/\text{c-Si}$) properties and the CdTe film structural parameters (e.g., d_b, d_s). The latter parameters were determined accurately in the analysis of the RTSE data. Figure 5.48 shows the inverted (ϵ_1, ϵ_2) spectra for the lowest void volume fraction CdTe film deposited at 188°C, together with the dielectric function of single crystal CdTe,⁸ both measured at room temperature. The much broader critical point peaks in (ϵ_1, ϵ_2) for the deposited film can be seen clearly, in contrast to the sharp features for c-CdTe, and are attributed to excited carrier scattering at grain boundaries and defects associated with the fine-grained polycrystalline structure of

the films. Four critical points are evident, the fundamental gap E_0 , along with E_1 , E_1+D_1 , and E_2 , as indicated in Fig. 5.48. The E_0 band gap of the deposited film appears markedly higher than that of c-CdTe, as shown on the expanded scale of Fig. 5.49. The other critical points also appear shifted and these will be discussed in detail in a later sub-section.

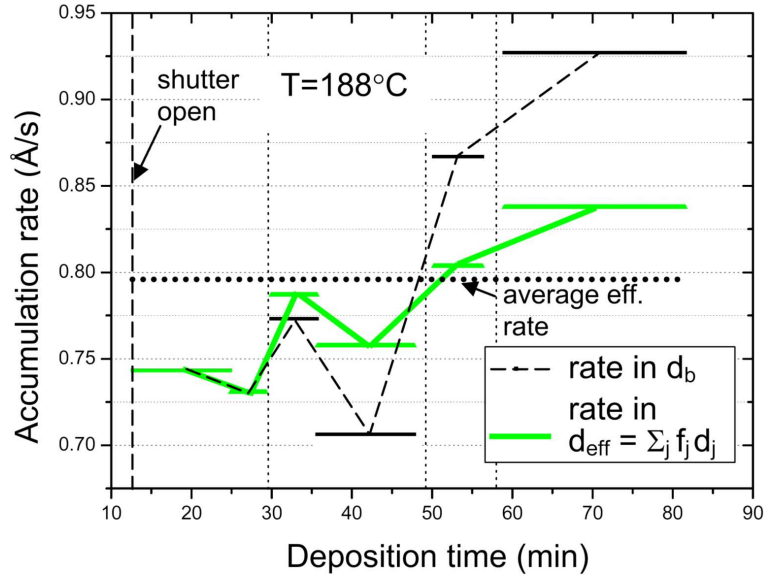


Figure 5.47: Deposition rate versus time obtained by two different ways: either from the bulk layer thickness (dashed line) or from the effective thickness (solid line) evolution in different stages of growth. The effective thickness is given by the product of the layer thickness and the material volume fraction summed over all layers in the stack. Also shown is the average effective deposition rate obtained from a linear fit of the effective thickness over the entire deposition.

Optical functions: Probe of temperature

The first step in determining the temperature dependence of the optical properties of the CdTe films is to establish a calibration for the true substrate temperature as a function of the nominal temperature. Because the energies of the critical points of single-crystal Si are well known, as are their variations with temperature,⁹ these characteristics can form the basis of the required calibration. In this calibration, the uncoated c-Si substrate just prior to CdTe deposition was first heated, and then stepwise cooled to room temperature while measuring by RTSE. The spectra collected during cooling were corrected to account for the native oxide

layer in order to extract the true c-Si dielectric functions. Two derivatives of each dielectric function were then taken, and the results were fit to standard critical point lineshapes¹⁰ in order to extract the E_1 and E_2 critical point energies versus nominal temperature. The energy shifts relative to values obtained at room temperature (actually 15°C due to water cooling of the substrate) provide two measurements of the true temperature which are in close agreement. The average of the two true temperature values can be related to the nominal temperature as shown in Fig. 5.50.

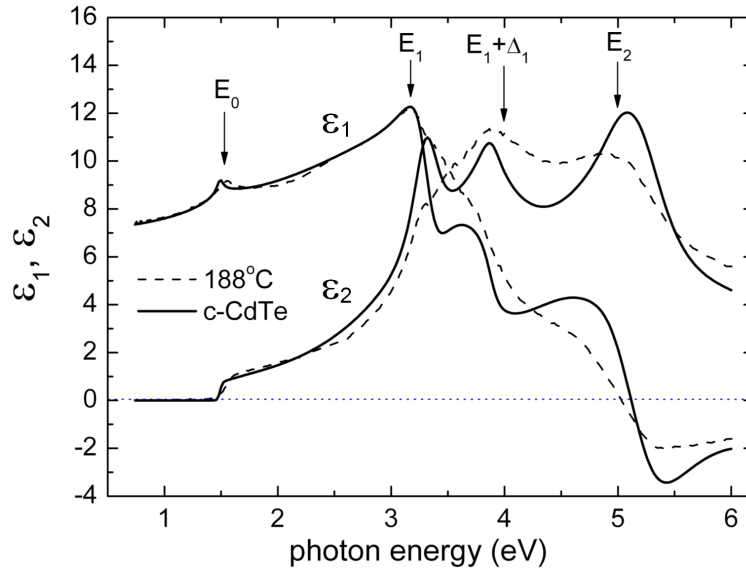


Figure 5.48: The room temperature dielectric functions of single crystal CdTe (solid lines) and the CdTe film deposited at 188°C (broken lines). The four downward arrows point to the energy values of the four critical point transitions E_0 , E_1 , $E_1 + D_1$, and E_2 for the film.

With the substrate temperature calibration of Fig. 5.50, optical data as a function of true temperature can be collected for the CdTe films. The parameter of greatest interest is the CdTe E_0 band gap energy which is desired as a secondary standard for temperature calibration that can be performed irrespective of the substrate on which the CdTe is deposited. The E_0 band gap of the CdTe film is obtained as a function of measurement temperature by temporarily suspending the deposition after a thickness of ~ 1000 Å, then stepwise cooling as measurements are taken, and finally reheating for continuation of the deposition. Figure 5.51 shows how this gap is extracted from the dielectric function spectra obtained for the

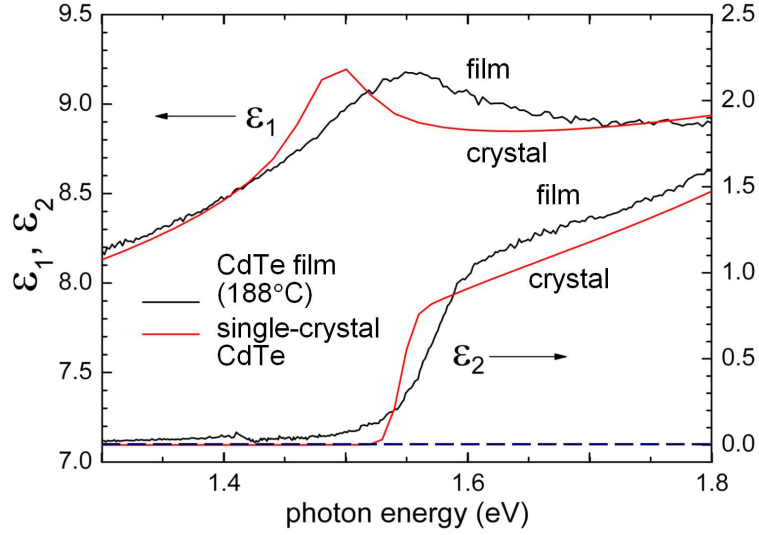


Figure 5.49: The room temperature dielectric functions of single crystal CdTe and the CdTe film deposited at 188°C in the vicinity of the band gap E_0 critical point. Note the significant shift to higher energy in the band gap of the film relative to that of the single crystal.

CdTe film deposited at 215°C and measured at 200°C and 15°C. As in the case of the c-Si dielectric function, two derivatives of the spectra are taken, and the results are fit to the standard Lorentzian-broadened lineshape function. Figure 5.52 shows the final results for the band gap energy as a function of measurement temperature for the CdTe film deposited at 304°C, starting at the deposition temperature and progressing to room temperature. A key parameter in this study is the slope of the linear change in band gap with temperature. The value obtained for this CdTe film is 3.71×10^{-4} eV/°C, a value within $\sim 1.5\%$ of that reported for single crystal CdTe.¹¹ Similar results are obtained for all five CdTe samples, as shown in the right side of Fig. 5.52. Averaging the slopes yields a value of 3.70×10^{-4} eV/°C. This provides a means for calibrating the substrate temperature for any deposited CdTe film – one simply measures the band gap shift between the process temperature and room temperature, and divides by the average temperature slope to obtain the process temperature. In spite of the nearly parallel data sets for the films and the single crystal in Fig. 5.52, the band gap energies are significantly shifted, by as much as 60 meV relative to the single crystal. This effect makes it impossible to calibrate substrate temperature based on

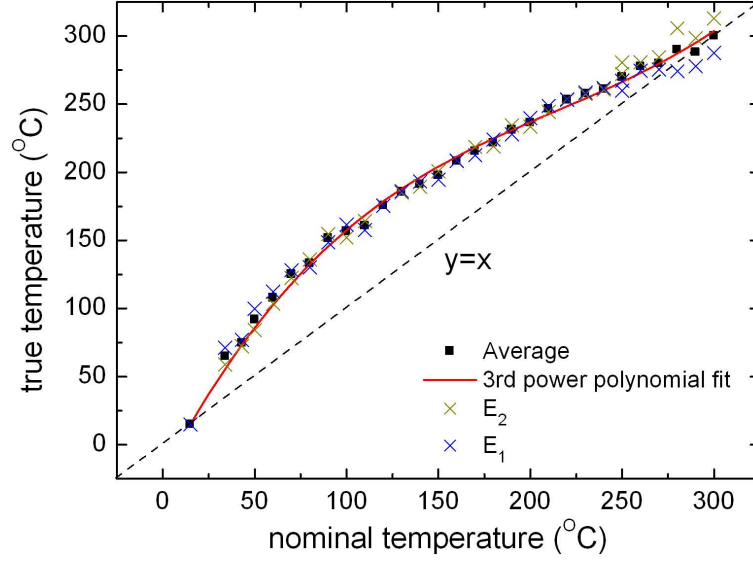


Figure 5.50: Substrate temperature calibration obtained by measuring the shifts relative to room temperature in the E_1 and E_2 critical point energies of the uncoated c-Si substrate as a function of nominal temperature measured by a thermocouple. Fig. 5.39 shows the configuration of the sample and the thermocouple.

a single measurement of band gap energy; energy differences are required. As described in greater detail in the next subsection, the variations in band gap among the different thin film samples at a fixed temperature are attributed to strain associated with compressive stress in the films.

Optical functions: Probe of film stress

Figure 5.53 shows the variation in the room temperature (15°C) E_0 band gap as a function of deposition temperature for the series of five CdTe films. It should be noted that these results were obtained for films deposited to thicknesses of ~ 1000 Å. Given the significant compressive stress observed in sputter-deposited thin films in general – up to the order of GPa¹², it is reasonable to attribute the band gap shifts in the CdTe films to the associated strain. A measure of the stress in these films can be obtained based on previous measurements that relate hydrostatic pressure to band gap in single crystal CdTe. These measurements have established a pressure coefficient of 65 meV/GPa.¹³ The right scale in

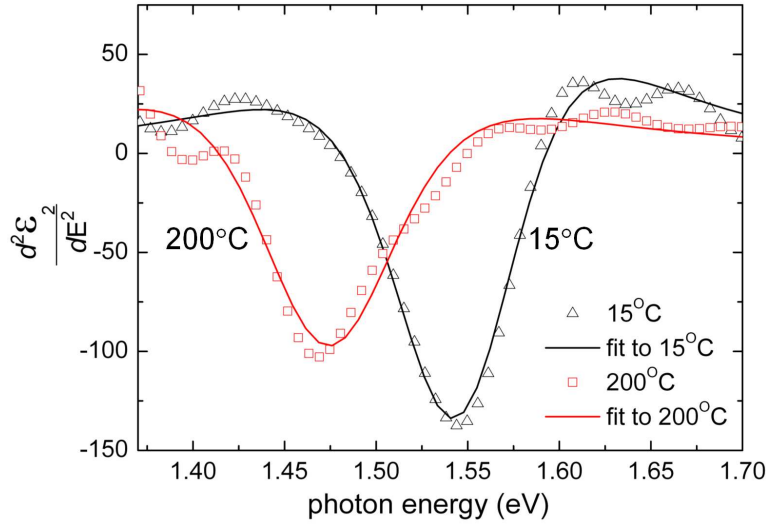


Figure 5.51: Second derivative of the dielectric functions for the CdTe film deposited at 215°C, as measured at true temperatures of 200°C and 15°C (room temperature) (points). Also shown is a fit to the second derivative of the dielectric function that provides the critical point energy.

Fig. 5.53 uses this linear relationship to estimate the compressive stress in the CdTe films; values from 0.4 to 0.9 GPa are obtained. In fact, for deposition temperatures above 220°C, the 1000 Å thick films pass through a stress transition whereby a factor of two decrease is observed over a $\sim 50^\circ\text{C}$ range. The very high stress levels in the two lowest temperature films are consistent with the void fraction evolution in Fig. 5.44. For thicknesses greater than 1000 Å, these films undergo abrupt structural transitions in which the void fractions increase significantly. For the two higher temperature films, the void fraction in the thin film regime is higher and no structural transition is observed. Thus a high initial stress in Fig. 5.53 is correlated with the appearance of a subsequent microstructural transition in the evolving film. Previous studies have indicated that for sputtered films deposited to similar thicknesses at different substrate temperatures, a transition to lower stress is observed at a substrate temperature equal to 1/3 the melting temperature of the sputtered material.¹² Presumably surface diffusion is the mechanism by which strain generated by ion bombardment is relaxed during the deposition process.

Optical properties: Probe of grain size and defect density

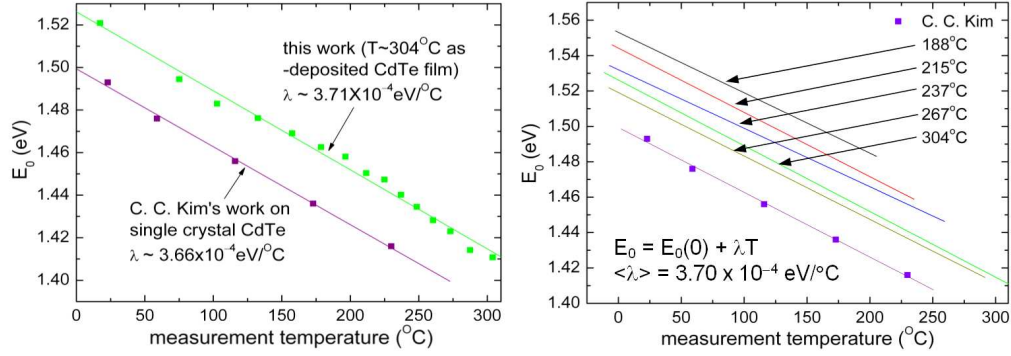


Figure 5.52: The E_0 critical point energy plotted as a function of true temperature obtained during cooling of a CdTe film from the deposition temperature of 304°C to room temperature (15°C) (left). Also shown are the linear variations in critical point energies for the set of five CdTe films prepared at different temperatures (right). Results for single-crystal CdTe are shown in both panels for comparison.

Figure 5.48 shows the significant difference between the dielectric function of thin film CdTe and that of the single crystal due to the fine-grained polycrystalline nature of the as-deposited film. Although energy shifts occur in the critical points of the thin film dielectric function due to strain, the primary difference arises from the broadening of the critical point structures due to scattering of optically excited carriers at grain boundaries and defects that reduce the lifetimes associated with the transitions. The room temperature dielectric functions for the five CdTe films have been compared in order to explore the effect of substrate temperature on the grain boundaries and defects that influence the optical properties. Figure 5.54 shows the room temperature dielectric functions for the CdTe films deposited at the lowest and highest substrate temperatures. These results were obtained after suspending each deposition at a thickness of 1000 \AA and cooling the film to 15°C . For the highest deposition temperature film, the dielectric function was scaled to the same void fraction as the low temperature one for ease of comparison. Relatively weak sharpening of the critical points occurs with increasing substrate temperature; however, even for the highest substrate temperature explored here, the critical point widths for the thin film are still much broader than those for the single crystal.

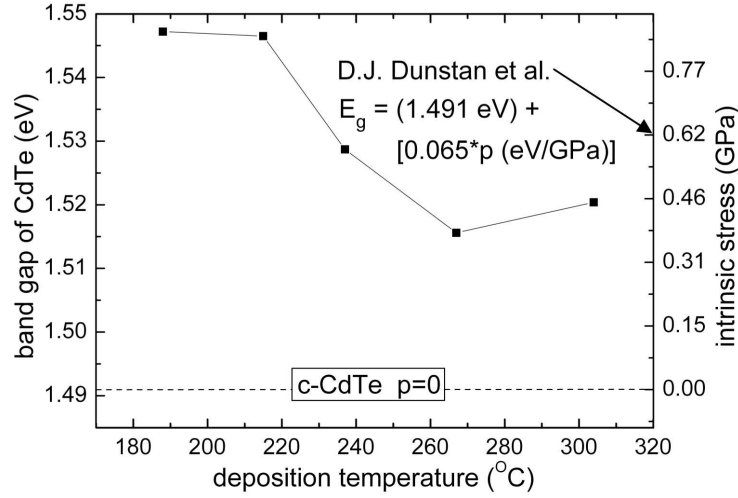


Figure 5.53: Room temperature (15°C) E_0 band gap for CdTe films obtained after a deposited thickness of 1000 Å, plotted as a function of the substrate temperature used in the deposition process. The right scale indicates the level of compressive stress in the film, assuming the linear relationship between the band gap and hydrostatic pressure as shown.

For each film, the dielectric function has been modeled using a sum of four critical point transitions E_0 , E_1 , $E_1 + D_1$, and E_2 ; along with a Tauc-Lorentz oscillator as broad background to represent transitions far away from the critical points.¹⁰ The critical point sum exhibits the following analytical form:

$$\varepsilon = \sum_n A_n \exp(i\varphi_n) (E_n - E - \Gamma_n)^{\mu_n} \quad (5.32)$$

Here the resonance energies E_n and broadening parameters Γ_n are of interest. The four best fit critical point energies and broadening parameters shown in Fig. 5.54 differ from those of single crystal CdTe (horizontal broken lines) possibly due to strain and to electron scattering at defects and grain boundaries, respectively. In fact, the upper part of Fig. 5.55 shows that for deposition temperatures above 220°C, all critical point energies shift toward the crystalline values. Further study of these higher energy transitions is warranted, in particular the effect of strain on the transition energies. In these studies, spectra in the strain-optic tensor will be determined for the single crystal in order to better understand

the shifts that occur in the thin films.¹⁴ The lower part of Fig. 5.55 shows weak tendencies in which the broadening parameters Γ_n decrease with increasing deposition temperature. This result indicates that higher deposition temperature yields larger grain size or lower defect densities in the films. The largest overall improvement occurs between 220 and 260°C where the stress transition occurs. Evidently the void development that relaxes the stress accompanies the formation of larger crystallites. Additional studies of the effect of defects on the critical point widths and energies are in progress using ion implantation of c-CdTe to generate controlled defect densities.

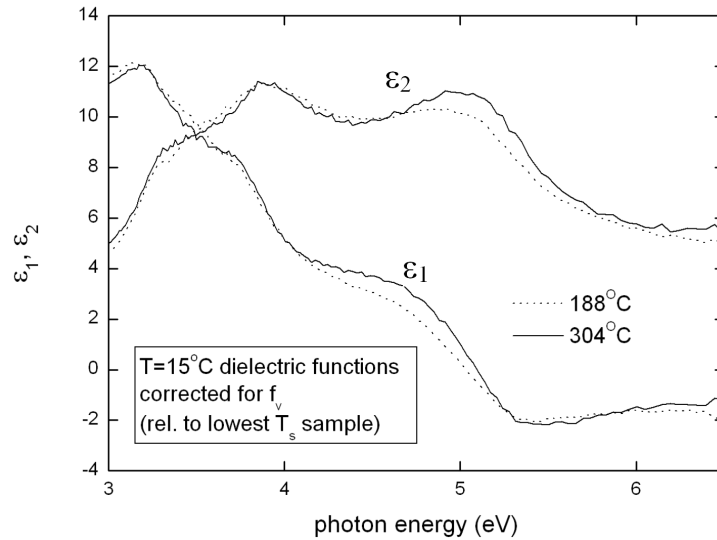


Figure 5.54: Room temperature dielectric functions of CdTe films deposited on c-Si substrates at the maximum (304°C) and minimum (188°C) temperatures used in this study. For ease of comparison, the void fraction of the film prepared at the highest temperature was scaled to the same value as that of the film prepared at the lowest temperature.

5.4. Results and Discussion: RTSE Studies Comparing CdS and CdTe Deposition

In this section, the various features of CdS deposition on c-Si will be compared to those of CdTe deposition. It should be kept in mind that the CdS is deposited to the typical thickness used in solar cells, 1300 Å, which is thinner than the final thickness of the CdTe films of

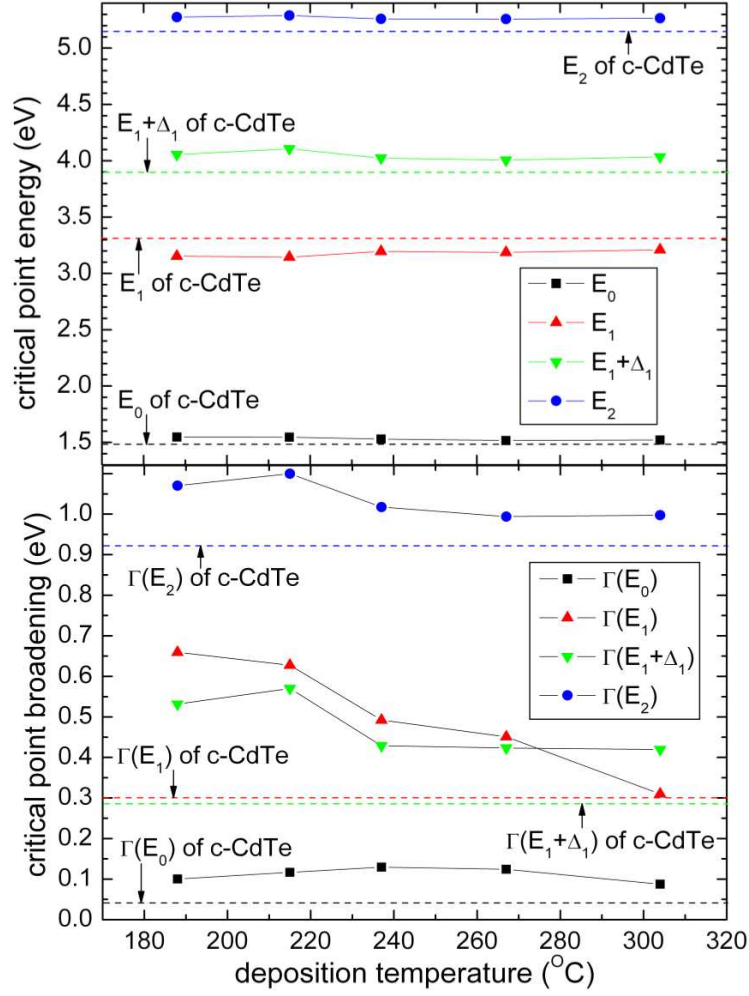


Figure 5.55: Resonance energies E_n (upper) and widths Γ_n (lower) of the critical point transitions in single crystal CdTe and in $d_b \sim 1000$ Å thick CdTe films sputter-deposited at different temperatures, all measured at 15°C.

this study, 3300 Å. The analysis of the RTSE data for CdS deposition is still in progress and certain features that have been treated in detail for the CdTe depositions remain to be studied for CdS. This effort will be completed in the next phase of this project.

Surface roughness evolution

Figure 5.56 shows the evolution of the surface roughness layer thickness with bulk layer thickness, comparing CdS and CdTe on the same bulk layer thickness scale. The nucleation behavior for the CdS is similar to that of CdTe to the extent that peak roughness

layer thickness increases monotonically with increasing deposition temperature, indicating enhanced diffusion of precursors on the film/substrate surface. In addition, the bulk layer thickness at which the peak roughness is observed (and at which the film begins to coalesce) shifts to increasing values with increasing temperature – again indicating a tendency toward S-K growth over V-W growth with increasing substrate temperature. Figure 5.57 shows the roughness thickness on the final film surface as a function of the deposition temperature for CdS in comparison with CdTe. In contrast to the results for CdTe, the final surface roughness thickness for CdS exhibits a broad minimum between 200 and 300°C. The decrease at low temperature can be attributed in both cases to an enhancement of surface diffusion that leads to a smoothening of nucleation generated surface structure. The roughening at high temperatures observed only for CdS may arise from enhanced crystalline grain growth.

Void volume fraction evolution

Figure 5.58 shows the step-wise depth profile in the relative void volume fraction for a CdS film deposited at 244°C. Only a slight increase in void fraction is observed with increasing distance from the substrate interface. The lower deposition temperature CdTe films exhibit similar behavior over the corresponding bulk layer thickness range (see Fig. 5.44). The inset in Fig. 5.58 shows continuous profiles in relative void volume fraction deduced from the high energy RTSE data for seven CdS films prepared at different substrate temperatures. For the CdS, the behavior of the near-surface relative void fraction with substrate temperature is significantly different than that of CdTe, as can be observed in Fig. 5.59. Here the relative void volume fraction near the surface of the film is shown as a function of deposition temperature, comparing CdS and CdTe for the same thickness of ~ 1300 Å, which for CdS is at the end of the deposition. Also shown are the results for CdTe at the end of the deposition (~ 3300 Å). It is evident that dense CdS films can be obtained over a wide range of substrate temperatures. The data show a weak decrease in void fraction over most of the temperature range with the minimum occurring at 310°C. At the highest temperature, the increase in void fraction may be related to the increase in surface roughness and associated grain growth processes that leave space between the crystallites.

Optical properties

Figure 5.60 shows the room temperature dielectric functions plotted together for the CdS films with the lowest and highest deposition temperatures. The sharpening of the critical

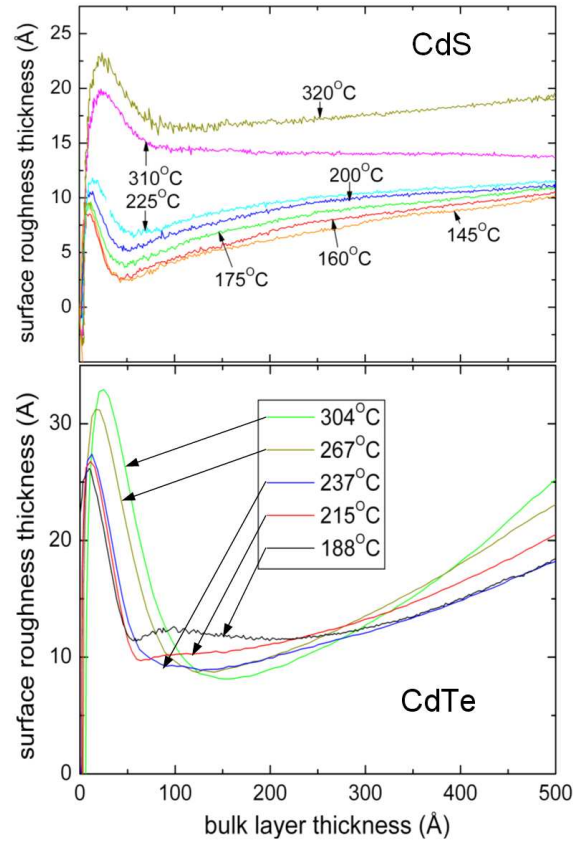


Figure 5.56: Surface roughness layer thickness versus bulk layer thickness during the initial nucleation and coalescence for CdS (top) and CdTe (bottom) as a function of deposition temperature.

points with the increase in deposition temperature is clear in this case, particularly through the improvement in the resolution of the so-called A and B transitions in the E_1 spectral region.¹⁵ Figure 5.61 provides a comparison of these two thin film dielectric functions with the room temperature ordinary and extraordinary wave pseudo-dielectric functions for the hexagonal form of single crystal CdS, which is optically uniaxial. The single crystal results were obtained in this study; however, no effort was taken to remove the native oxide from the single crystal. As a result, some distortions of the pseudo-dielectric functions $\langle \epsilon \rangle$ from the true dielectric functions ϵ occur; however, the key comparisons of the critical points for the thin film and crystal are not influenced by this distortion. The comparison in Fig. 5.61 (left) suggests that the broad asymmetric dielectric function peak in the E_1 region of

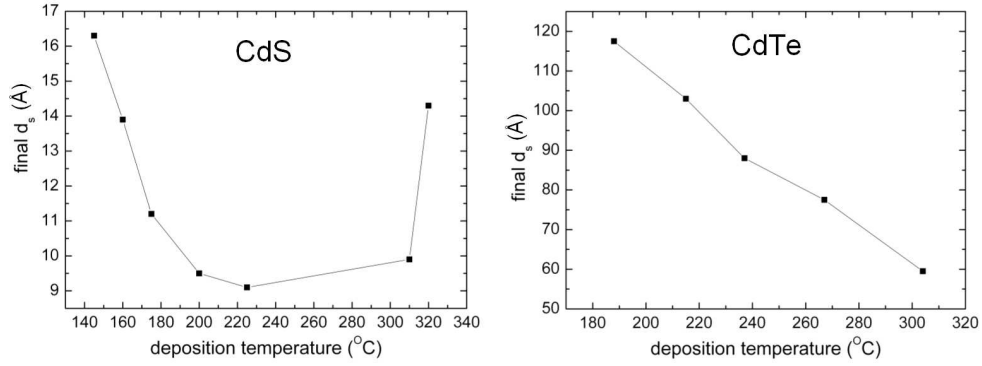


Figure 5.57: Surface roughness layer thickness at the end of the deposition for 1300 Å thick films of CdS (left) and 3300 Å thick films of CdTe (right), plotted as a function of deposition temperature.

the lowest temperature film is derived from the broadened E_1 -A and E_1 -B transitions in the ordinary dielectric function of the c-CdS. The resolved transitions in the E_1 region of the highest temperature film also appear to be derived from the E_1 -A and E_1 -B transitions in the ordinary dielectric function of c-CdS. In fact, the relative peak/shoulder heights in the film dielectric functions are consistent with those in the ordinary dielectric function of the hexagonal single crystal. In addition, the appearance of the E'_0 transition in the film dielectric functions is also common to the ordinary dielectric function.¹⁵ Neither the E_1 -A and E_1 -B doublet nor the E'_0 peak is observed in the extraordinary dielectric function of the hexagonal single crystal, or in the metastable cubic phase. The absence of influence of the extraordinary dielectric function of the single crystal on the thin film dielectric function suggests that the near-surface of the thin films is hexagonal and have c-axis orientation. Under these circumstances, the strongly refracted wave below the ambient/CdS interface lies predominantly within the film plane and samples only the ordinary dielectric function. However, further studies are needed to verify this conclusion.

Figure 5.62 shows the optical band gap measured at room temperature for the final CdS films plotted as a function of the deposition temperature. These data show an abrupt increase in gap within the temperature range from 150 to 200°C. The magnitude of the increase ~ 13 meV is not as large as that observed at higher substrate temperatures for

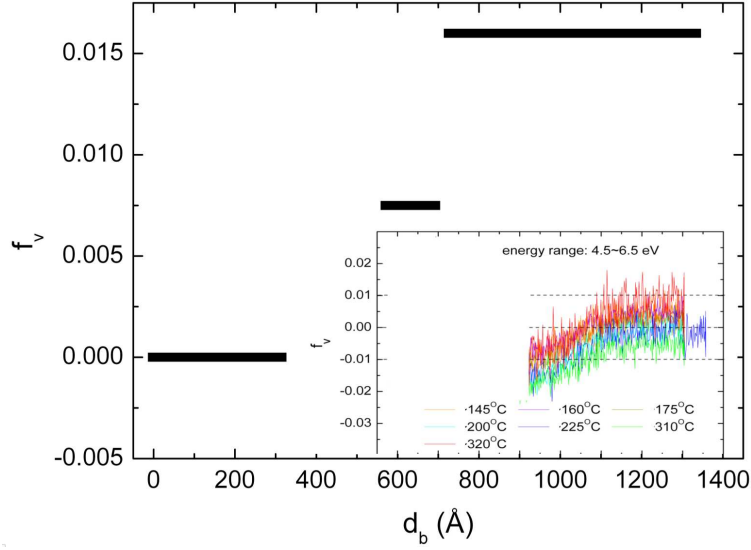


Figure 5.58: Step-wise depth profile in the void volume fraction for a CdS film fabricated at a temperature of 244°C. The void volume fraction is measured relative to the highest density layer at the substrate interface. Shown in the inset are continuous depth profiles in the relative void volume fraction for the entire series of CdS films fabricated as a function of substrate temperature. At the end of deposition, all void volume fraction values lie within ± 0.01 .

CdTe (32 meV; from 220 to 270°C; see Fig. 5.53). The band gap shift for CdS could be related to a stress transition as for CdTe, or it may be related to changes in crystallography of the film with substrate temperature. Further studies are required including measurement of the strain-optic tensor for the single crystal CdS. Figure 5.63 shows the variation in the E_0 , E_1 -A, and E_1 -B critical point widths measured at room temperature and plotted as a function of the substrate temperature of the CdS film. These results are compared with the corresponding data for E_0 , E_1 , and E_1+D_1 for CdTe. Continuous trends in the widths of the CdS critical point structures are even clearer than for the CdTe films. These trends suggest a continuous increase in grain size with substrate temperature, rather than changes in crystallography that would lead to the suppression or even disappearance of the E_1 -B transition, for example. Even the rate at which the CdS film critical points in Fig. 5.63 narrow with temperature shows a consistent trend. The rate of narrowing appears to reflect competition between intrinsic and extrinsic lifetime reducing effects such as phonon

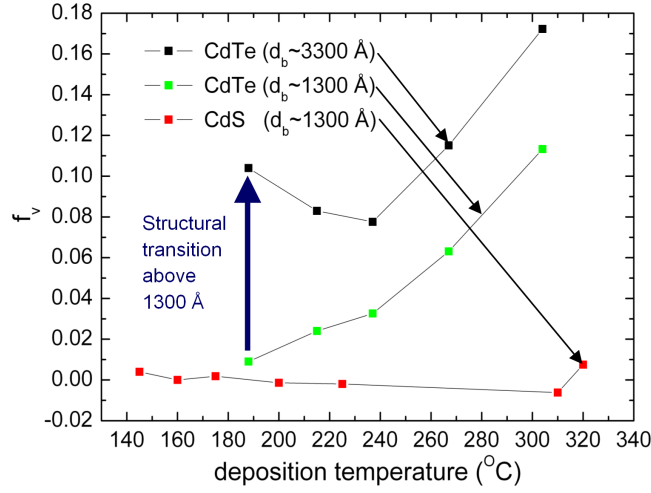


Figure 5.59: Relative void volume fraction variations with substrate temperature for the top-most sub-(bulk layer) of CdTe after thicknesses of 1300 and 3300 Å and for the top-most sub-(bulk layer) of CdS after a thickness of 1300 Å. The vertical line indicates the effect of the structural transition which occurs for CdTe at thicknesses above 1300 Å and for deposition temperatures below 240°C. Void variations with deposition temperature for the CdS are not significant.

scattering (which occurs at constant rate for all samples) and grain boundary scattering (which occurs at a rate of $\sim v/R$, where v is the electron velocity and R is the grain radius). For the higher energy critical points the width saturates at a lower substrate temperature suggesting a lower electron velocity. In future work the electronic transitions in the CdS will be related to the band structure so that a better understanding of information conveyed by these critical points is achieved.

A second trend that occurs clearly in the CdS, but much less so in the CdTe is the evolution with thickness in the critical point widths. Figure 5.63 shows an example in which a step-wise depth profile in the width of the band gap transition is extracted from real time data collected during film growth at a temperature at 244°C. The result suggests that the average grain size increases rapidly with thickness and the material nearest the substrate interface has a grain size characteristic of bulk material deposited at a much lower temperature of $\sim 120^\circ\text{C}$.

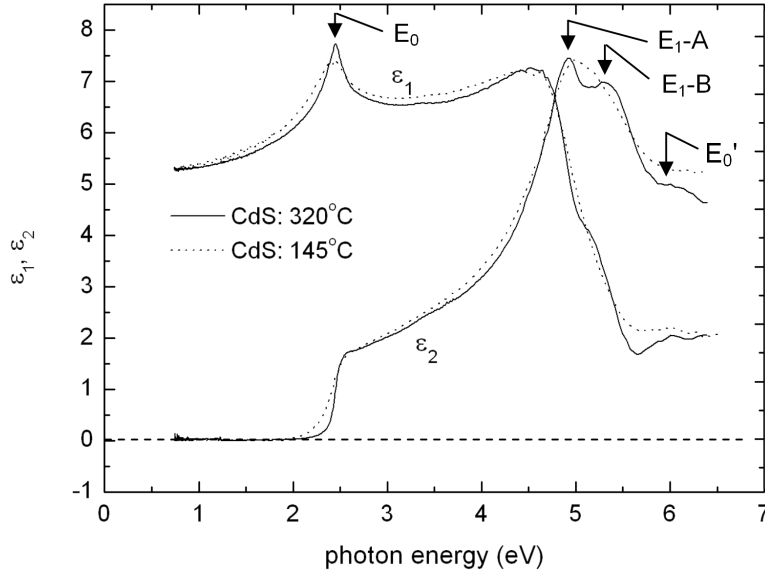


Figure 5.60: Room temperature dielectric functions of magnetron sputtered CdS films prepared at the lowest (145°C) and the highest (320°C) substrate temperatures used in this study. The arrows indicate the locations of the E_0 (fundamental band gap), E_{1-A} , E_{1-B} , and E'_0 critical point energies.

5.5. Results and Discussion: Studies of Post-Deposition Treatments

Analysis results have been obtained focusing on the effects of post-deposition processing for the CdTe films deposited on native oxide-covered c-Si substrates as presented in detail in a previous section. The experiment to be described applied the etch-back method to three ~ 3000 Å thick CdTe films co-deposited on c-Si substrates held at 188°C. These films were exposed to the following post-deposition processing conditions: (i) as-deposited (i.e., no treatments), (ii) thermally annealed at 387°C for 30 min, and (iii) CdCl₂ treated also at 387°C, but for 5 min. For each sample, the etch-back method was performed using successive immersion steps in Br₂+methanol, and each etch step led to a ~ 300 Å reduction in the bulk layer thickness. Because of the relative smoothness of the as-deposited CdTe (compared, for example, to depositions on TEC glasses), the successive etching treatments led to very smooth surfaces from which high accuracy dielectric functions are possible. In addition, the absence of an underlying CdS film in this case avoids the complication of alloying of CdTe

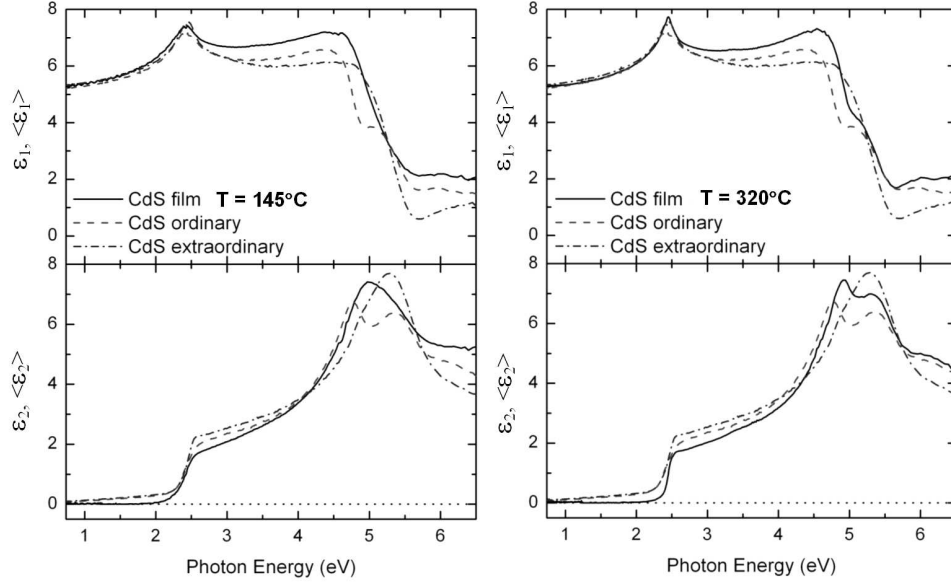


Figure 5.61: Room temperature dielectric functions ϵ of magnetron sputtered CdS films prepared at the lowest (145°C; left) and the highest (320°C; right) substrate temperatures used in this study. Shown for comparison are the ordinary and extra-ordinary wave pseudo-dielectric functions $\langle \epsilon \rangle$ of the hexagonal form of single crystal CdS.

due to S in-diffusion.

As an example of the key role of the CdCl_2 treatment, Fig. 5.65 shows best-fit analytical models for the room temperature dielectric functions of the as-deposited CdTe film and the film with the 5 min CdCl_2 -treatment. The spectra for the latter film was obtained after a sufficient number of etch cycles so that its thickness matched that at which the as-deposited film was measured (~ 1000 Å). As previously shown in Figs. 5.48 and 5.55, the dielectric function of the as-deposited film exhibits critical points that are significantly broadened compared to those of the single crystal. In contrast, for the film with the 5 min CdCl_2 treatment, the critical point characteristics are essentially the same as those of single-crystal CdTe. The primary difference between the dielectric function of the CdCl_2 -treated film and the single crystal is the presence of a small volume fraction of voids that reduce the dielectric function amplitude.

To expand on these observations, Figures 5.66 and 5.67 show depth profiles in the E1

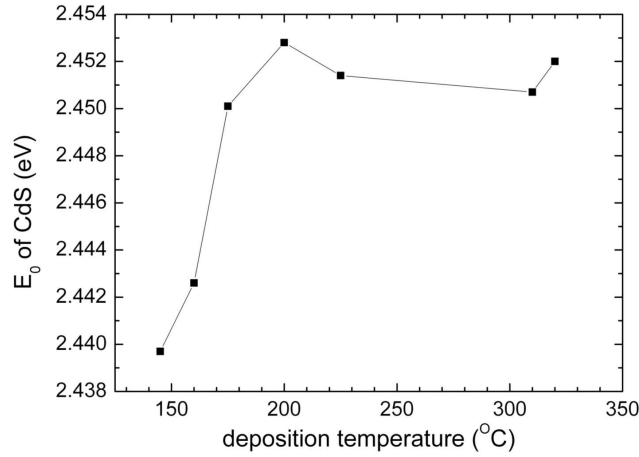


Figure 5.62: Room temperature dielectric functions of magnetron sputtered CdS films prepared at the lowest (145°C) and the highest (320°C) substrate temperatures used in this study. The arrows indicate the locations of the E_0 (fundamental band gap), E_1 -A, E_1 -B, and E'_0 critical point energies.

critical point transition energies and widths along with the relative void volume fractions obtained during etch-back analysis for the three differently-processed films. In Fig. 5.66, the E_1 transition results for the CdTe films (data points) are compared to the results for the single crystal (horizontal broken lines). For the as-deposited CdTe, the E_1 critical point energy starts from the single crystal CdTe value near the surface and shifts to much lower values as the substrate interface approached. This is attributed to higher strain in the material closest to the substrate interface, and is consistent with previous proposals that the structural transition centered near ~ 2000 Å serves to relax strain in the subsequently growing thin film. In fact, the E_1 energy for the as-deposited film of 3.2 eV at 1500 Å in Fig. 5.66 is similar to that at 1000 Å thickness in Fig. 5.55. The average E_1 width for the as-deposited film in Fig. 5.66 (~ 0.6 eV) is also consistent with the results in Fig. 5.55 for the 1000 Å thick film (~ 0.65 eV). These comparisons support the validity of the etch-back procedure.

Upon thermal annealing for 30 min, the following observations can be made from Fig. 5.66. First, the critical point energy becomes more uniform with depth within the film apparently due to the relaxation of strain nearest the substrate interface. Second, the

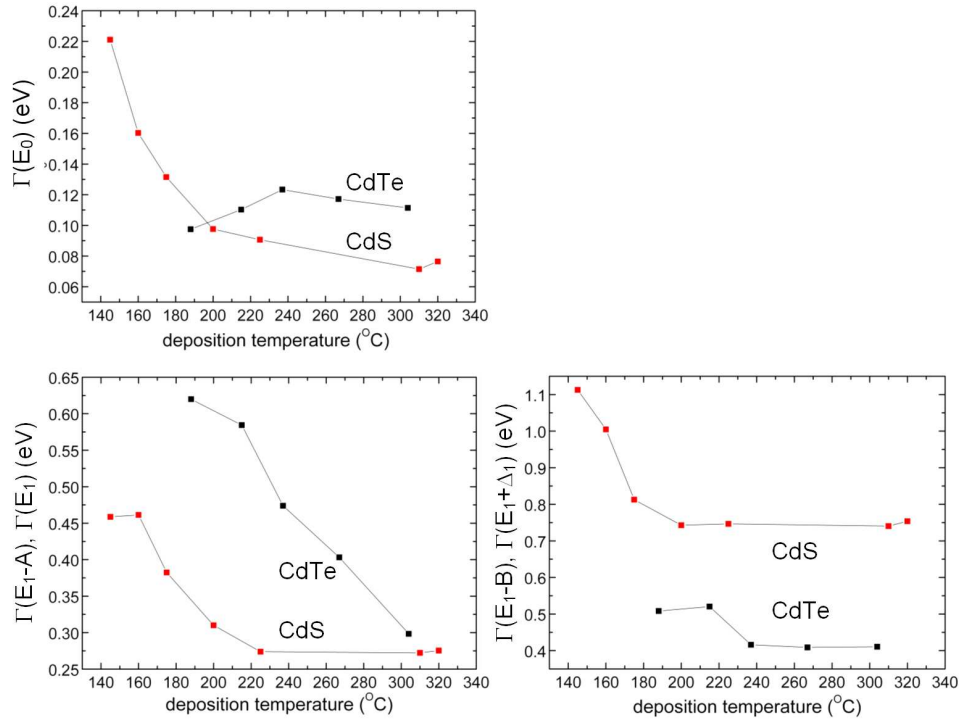


Figure 5.63: Room temperature dielectric functions ε of magnetron sputtered CdS films prepared at the lowest (145°C; left) and the highest (320°C; right) substrate temperatures used in this study. Shown for comparison are the ordinary and extra-ordinary wave pseudo-dielectric functions $\langle \varepsilon \rangle$ of the hexagonal form of single crystal CdS.

critical point narrows preferentially close to the substrate interface indicating significant grain growth in the 2000 Å nearest the substrate interface. Because the critical point width near the film surface remains unchanged, the grain size near the surface remains similar to that in the as-deposited film, possibly fixed by the presence of the oxide layer. Finally the large decrease in void fraction with depth into the as-deposited film due to the structural transition is suppressed in the annealed film (Fig. 5.67). Because these void fractions are scaled relative to the highest density in the individual profile, the relative scaling of the two data sets is arbitrary. Upon CdCl₂ treatment for 5 min, the behavior of the depth profiles is distinctly different in terms of grain size distribution. First, the critical point energy shifts even closer to the single crystal value and is independent of depth. Second, the critical point

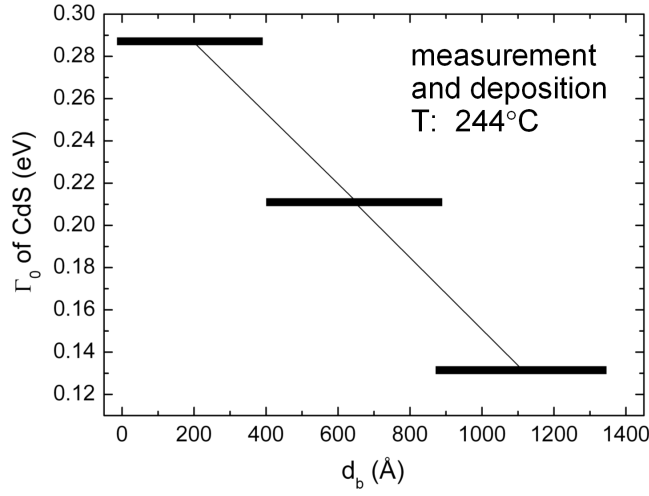


Figure 5.64: Step-wise depth profile in the width of the band gap critical point for CdS obtained from real time measurements obtained during deposition at a substrate temperature of 244°C. Because the measurements were performed in real time these widths are characteristic of a measurement temperature of 244°C as well.

width matches the single crystal value and is also constant with depth. This indicates that the grain size increases significantly throughout the entire depth of the film and is uniform from the substrate interface to the surface. Finally, the void volume fraction relative to the single crystal is uniform with depth compared with the as-deposited film at an average value of ~ 0.05 . It is likely that voids remain due to the microstructure of the as-deposited film. The next step in the study of CdTe post-processing is to deposit the CdTe film on CdS/c-Si which is closer to the actual device configuration, but maintains the advantage of smooth surfaces and interfaces.

It is more difficult to address the corresponding issue of post-process treatments for the CdS films, and such work is in progress. First, the effectiveness of the etch-back procedure has yet to be verified for CdS. Second, in order for post-deposition treatment studies to be relevant for device structures, the CdS must be capped with CdTe. However, this prevents light from the CdTe/ambient side of the CdS film from entering at photon energies above the band gap of the overlying CdTe. As a result, the use of a prism arrangement has been explored in which case the CdS is deposited directly on a fused silica prism held at 200°C,

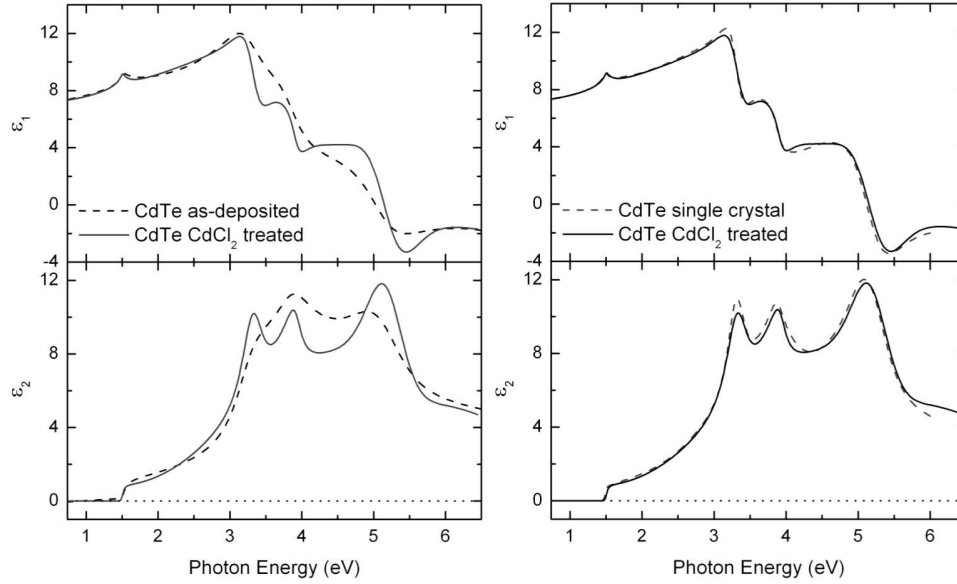


Figure 5.65: (left) Best fit analytical models of the room temperature dielectric functions for two CdTe films of thickness ~ 1000 Å, obtained from the same deposition but with different post-processing: as-deposited (no treatments; broken line) and CdCl₂-treated for 5 min at 387°C (solid line); (right) a comparison between the CdCl₂-treated CdTe film (solid line) and single crystal CdTe (broken line).

then over-deposited by CdTe, and finally measured by spectroscopic ellipsometry through the prism side before and after CdCl₂-treatment. Figure 5.68 (left) shows analytical dielectric functions of CdS as-deposited on such a prism, measured from the prism side, in comparison to CdS as-deposited on c-Si using the lowest deposition temperature of 145°C, measured from the ambient side as described in the previous section. The dielectric function of the CdS as-deposited on the prism is suppressed significantly in amplitude, particularly at the higher energies, and the critical point features are very broad. Because the light beam does not penetrate very deeply into the CdS at the higher energies, the high energy dielectric function results are characteristic of the near-interface CdS which is apparently of very low density (or a physical or chemical mixture of the substrate material). Furthermore the extensive broadening suggests a nanocrystal CdS phase at the interface. Figure 5.68 (right) shows that the CdCl₂ treatment appears to densify the CdS somewhat, but the material

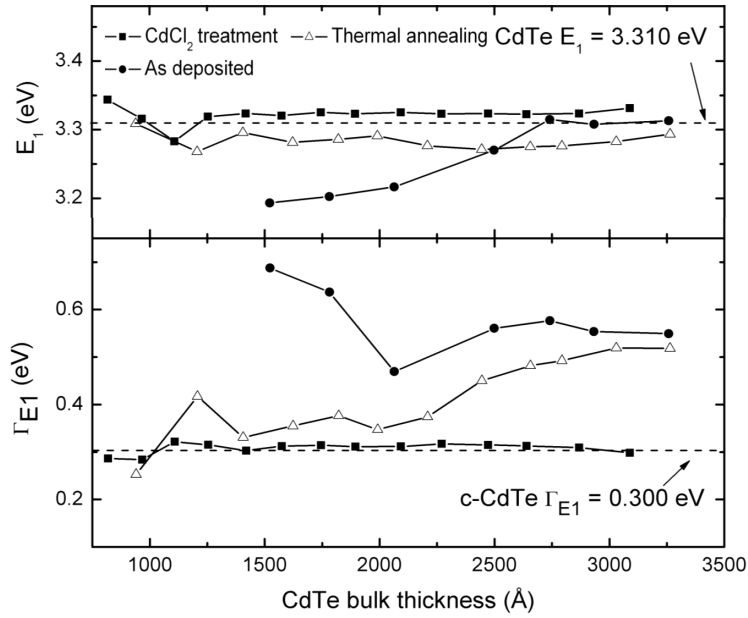


Figure 5.66: Critical point energies (top) and widths (bottom) as functions of CdTe bulk layer thickness during etching by Br₂+methanol for co-deposited CdTe films processed in three different ways: (i) as-deposited, (ii) thermally annealed for 30 min, and (iii) CdCl₂ treated for 5 min.

remains nanocrystalline.

5.6. Summary

Capabilities

Spectroscopic ellipsometry has been applied as a real time probe of as-deposited films of CdTe and CdS. In both studies performed to date, c-Si substrates have been used to avoid substrate-induced surface roughness which complicates data analysis. Once the various microstructural and optical features have been uncovered using the smooth, ideal substrates, application of similar approaches for the more difficult device-relevant substrates becomes possible. The following capabilities have been established so far:

- Time evolution of surface roughness layer thickness describing the initial clustering during nucleation and the structural evolution throughout growth;

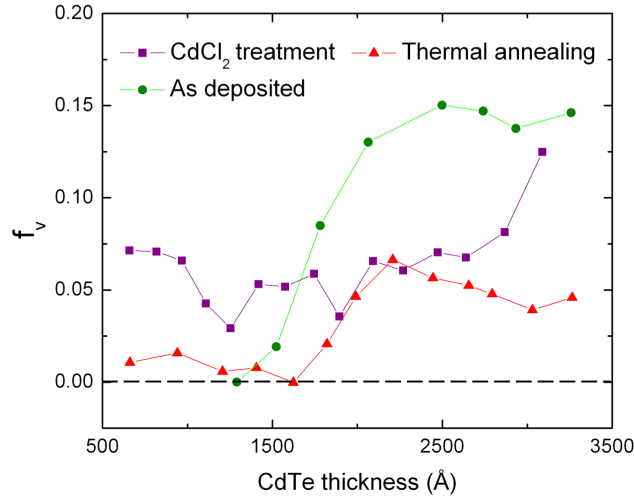


Figure 5.67: Relative void volume fractions as functions of CdTe bulk layer thickness during etching by Br₂+methanol for co-deposited CdTe films processed in three different ways: (i) as-deposited, (ii) thermally annealed for 30 min, and (iii) CdCl₂-treated for 5 min. For the as deposited and annealed films, the void fraction is scaled relative to the depth at which the highest density is observed. For the CdCl₂-treated film, the void volume fraction is scaled relative to single crystal CdTe.

- Time evolution of the bulk layer thickness describing the growth mode and the instantaneous deposition rate in terms of thickness;
- Time evolution of the void volume fraction which when combined with the time evolution of the bulk layer thickness gives a depth profile in the void volume fraction throughout the film;
- Depth profile in the void fraction for a previously deposited film via post-deposition etch-back processing;
- Effective deposition rate or volume of material per area per time describing mass accumulation during deposition;
- Fundamental band gap energy; the shift relative to room temperature provides the sample temperature, and the shift relative to the single crystal value provides the film stress;

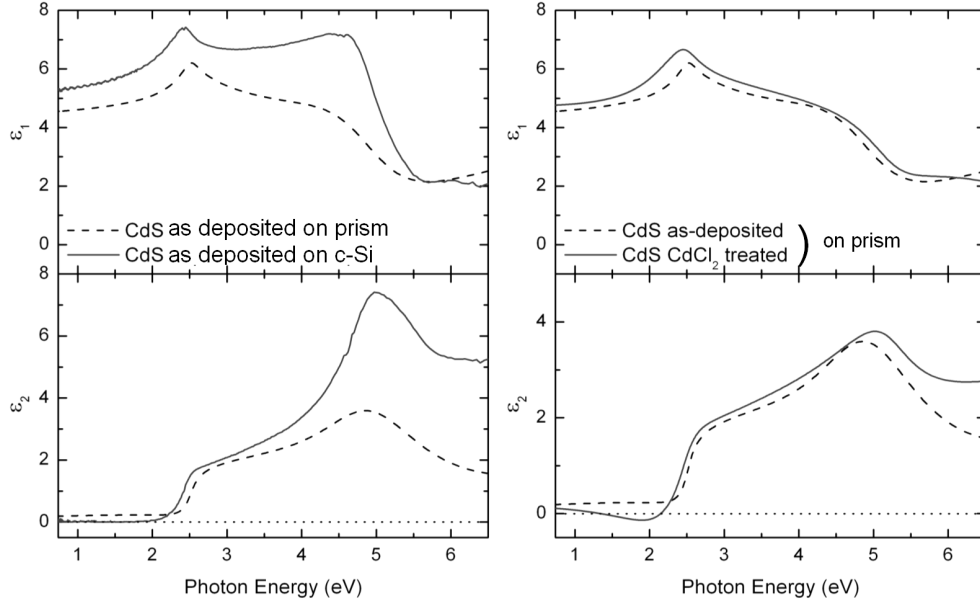


Figure 5.68: (left) Best fit analytical models to the room temperature dielectric functions of CdS films as-deposited on a fused silica prism measured from the prism side and on a c-Si wafer measured from the ambient side; (right) best fit analytical models to the room temperature dielectric functions of CdS measured from the prism side before and after a 30 min CdCl_2 treatment at 387°C .

- Critical point widths provide a measure of the grain size or defect density;
- Depth profiles in the higher critical point energies and widths (due to the shallow penetration depth of the light) which in turn provides measures of the depth distribution in the grain size and strain, via post-deposition etch-back processing;
- Dielectric function characteristics provide information on crystallography (crystalline phase and orientation) for a complex material such as CdS which is optically anisotropic in its stable phase and can assume a metastable phase in a different crystal system.

In the future, additional capabilities related to the interaction between the CdS and CdTe layers during interface formation will be established.

Results

Using the capabilities of the previous section, the following conclusions have been drawn from studies of the growth of CdTe and CdS on smooth c-Si substrates.

(1) CdTe films deposited at low temperatures ($<200^{\circ}\text{C}$) develop a relatively high density of clusters on the substrate surface in the initial nucleation stages due to limited diffusion of film precursors on the substrate/film surface. These clusters coalesce to form a high density film – in fact, comparable in density to single crystal CdTe – that is under high compressive stress (approaching 1 GPa) in the early stages of film growth (first ~ 1000 Å), as indicated by a blue-shifted band gap (by ~ 60 meV). This high density film undergoes a structural transition after a thickness of ~ 1500 Å whereby a relatively high volume fraction of voids (~ 0.10) develops in the films over a narrow range of thickness. These voids propagate throughout the film with continued growth, possibly due to shadowing effects typical of physical vapor deposition.

(2) CdTe films deposited at higher temperatures ($>250^{\circ}\text{C}$) develop a relatively low density of clusters on the substrate/film surface due to enhanced surface diffusion; however, the resulting larger clusters do not completely coalesce to a dense film. As much as 0.07 volume fraction of voids remain trapped in the initially growing film and this volume fraction is enhanced gradually with increasing thickness. Due to the initial void development, films deposited in this temperature range show a significantly lower compressive stress (<0.5 GPa) as indicated by band gaps that are closer to the single crystal (~ 25 meV blue-shifted).

(3) Due to the trade-off between the stress-induced structural transition at low temperature and the incomplete coalescence of nucleating clusters at high temperature, a CdTe film deposition temperature is found ($\sim 230^{\circ}\text{C}$) at which the void volume fraction is minimized in the top-most part of the film (i.e., for thicknesses greater than 2000 Å). This deposition temperature is close to that found to optimize solar cell performance in previous studies, and suggests possible approaches for improving the present optimum based on controlling void evolution through the appropriate combination of temperature and ion bombardment (i.e., gas pressure, dc substrate bias) in different growth stages of the film. It should be remembered however, that (a) these ellipsometric studies were done on Si wafers and our sputtered cells are typically grown on TEC-7 or aluminosilicate glass, which may affect grain nucleation and void fraction, and (b) other ellipsometric studies using etch-back techniques indicate that subsequent CdCl_2 treatment can reduce the void fraction accumulated during

the deposition. Studies are underway to determine how the final void fraction is affected by the substrate and the subsequent CdCl_2 processing.

(4) CdS film growth occurs at relatively high density throughout the temperature range explored ($\sim 140 - 320^\circ\text{C}$) and for the typical thicknesses used in the solar cell. In this case, the dominant effect with increasing temperature is an apparent increase in crystalline grain size as indicated by a reducing in the broadening parameter associated with the band gap transition near 2.45 eV. In fact, the broadening of this transition (assumed Lorentzian) decreases by a factor of three from 0.22 eV to 0.07 eV between deposition temperatures of 140 and 310°C . In addition, the broadening parameter increases significantly with accumulated thickness. Because one mechanism for optical transition broadening is grain boundary scattering, these observations suggested enhanced crystalline grain growth with increasing temperature and with increasing thickness along the growth direction.

(5) A double-peaked structure is prominent in the E_1 region near 5 eV for the dielectric function of CdS films prepared at the highest temperatures ($\sim 300^\circ\text{C}$). This characteristic is only observed in the ordinary wave response of the hexagonal single crystal (but not in the extraordinary wave response, nor in the metastable cubic phase). This suggests a c-axis alignment of the crystallites in the near-surface region of these films. The CdS near the interface to the substrate shows much broadened critical points compared to the near-surface material, both for depositions on c-Si and fused silica – a broadening effect not observed for CdTe films – indicating an unidentified nanocrystalline CdS phase in this region. The nanocrystalline region in the CdS near the substrate interface is not significantly changed by a standard CdCl_2 treatment.

(6) A 5-min CdCl_2 treatment of a thin (~ 3000 Å) CdTe film on a c-Si substrate is observed to narrow the high energy critical points in the dielectric function to width values very close to those of single crystal CdTe and to shift their energies closer to the single crystalline values, as well. These effects occur uniformly throughout the film as indicated by etch-back depth profiling analysis. Voids in the CdCl_2 -treated films are detected that are likely to originate from microstructure in the as-deposited film. In contrast to the CdCl_2 treatment effects, a 30-min thermal anneal of the CdTe led to crystalline grain growth near the substrate interface, but the same grain structure in the near surface region as the as-deposited film. Such conclusions are based on near-surface critical point widths that are the same before and after the annealing.

References

- ¹ J. Li, J. Chen, N. J. Podraza, and R. W. Collins, Proceedings of the 4th World Conference on Photovoltaic Energy Conversion, May 2006, Waikoloa, HI (IEEE, Piscataway, NJ, 2006) in press.
- ² J. Chen, J. Li, D. Sainju, K. D. Wells, N. J. Podraza, and R. W. Collins, Proceedings of the 4th World Conference on Photovoltaic Energy Conversion, May 2006, Waikoloa, HI (IEEE, Piscataway, NJ, 2006) in press.
- ³ A. Gupta and A.D. Compaan, Appl. Phys. Lett. 85, 684 (2004).
- ⁴ J. Lee, P. I. Rovira, I. An, and R. W. Collins, Rev. Sci. Instrum. 69, 1800 (1998); commercially-available instrument: M-2000; J. A. Woollam Co., Lincoln NE.
- ⁵ I. An, J.A. Zapien, C. Chen, A.S. Ferlauto, A.S. Lawrence, and R.W Collins, Thin Solid Films 455, 132 (2004).
- ⁶ H. Fujiwara, J. Koh, P. I. Rovira, and R. W. Collins, Phys. Rev. B 61, 10832 (2000).
- ⁷ J.A. Venables, G.T.D. Spiller, and M. Hanbucken, Rep. Prog. Phys. 47, 399 (1984).
- ⁸ B. Johs, C. Herzinger, J. Dinan, A. Cornfeld, J. Benson, Thin Solid Films 313, 137 (1998).
- ⁹ P. Lautenschlager, M. Garriga, L. Vina, and M. Cardona, Phys. Rev. B 36, 4821 (1987).
- ¹⁰ R.W. Collins and A.S. Ferlauto, in Handbook of Ellipsometry, (William Andrew, Norwich, NY, 2005), p.93.
- ¹¹ C.C. Kim, M. Daraselia, J.W. Garland, and S. Sivanathan, Phys. Rev. B 56, 4786 (1997).
- ¹² H. Windischmann, J. Vac. Sci. Technol. A 9, 2431 (1991).
- ¹³ D. Dunstan, B. Gil, C. Priester, K. Homewood, Semicond. Sci. Technol. 4, 241 (1989).
- ¹⁴ M. Cardona, Thin Solid Films 313-314, 10 (1998).
- ¹⁵ P. Hofmann, K. Horn, A.M. Bradshaw, R.L. Johnson, D. Fuchs, and M. Cardona, Phys. Rev. B 47, 1639 (1993).

6. PUBLICATIONS

6.1. Refereed papers published or in press (3/1/05 - 5/31/06)

1. "Piezo-effect and physics of CdS based thin-film photovoltaics", Diana Shvydka, J. Drayton, A. D. Compaan, and V. G. Karpov, Appl. Phys. Lett. **87**, pp. 123505-1-3 (2005).
2. "Physical model of CdS based thin-film photovoltaic junctions", M. L. C. Cooray and V. G. Karpov, Appl. Phys. Lett., **88**, p. 093508 (2005).
3. "Cu K-edge EXAFS Studies Of CdCl₂ Effect On CdTe Solar Cell", Xiangxin Liu, A. D. Compaan, and Jeff Terry, MRS Symp. Proc. **865**, edited by W. Shafarman, T. Gessert, S. Niki, S. Siebentritt, F4.2 (2005).
4. "Photoluminescence from Ion Implanted CdTe Crystals", Xiangxin Liu and Alvin D. Compaan, MRS Symp. Proc. **865**, edited by W. Shafarman, T. Gessert, S. Niki, S. Siebentritt, F5.25 (2005).
5. "Photoluminescence and Extended X-ray Absorption Fine Structure Studies on CdTe Material", Xiangxin Liu, Ph.D. Thesis: The University of Toledo, 2006 (unpublished, will be available at OhioLINK- Electronic Theses and Dissertations Center, <http://www.ohiolink.edu/etd/>).
6. "High efficiency ultra-thin sputtered CdTe solar cells" A. Gupta, V. Parikh, A.D. Compaan, Solar Energy Materials and Solar Cells, **90**, 2263-2271 (2006).
7. "Spatial and Temporal Variations in Electronic Transport Through a CdTe-Based Schottky Barrier", Diana Shvydka, V. Parikh, V.G. Karpov and A.D. Compaan, MRS Symp. Proc. **865**, edited by W. Shafarman, T. Gessert, S. Niki, S. Siebentritt, p. F12.2, (2005).
8. "Physics of CdTe Photovoltaics: From Front to Back", V.G. Karpov, Diana Shvydka, and Yann Roussillon, MRS Symposium Proceedings **865**, edited by W. Shafarman, T. Gessert, S. Niki, S. Siebentritt, p. F10.1, San Francisco, March 28-April 1 2005.

9. "Lateral Nonuniformity and Mesoscale Effects in Giant Area Electronics, V. G. Karpov, Diana Shvydka, and Yann Roussillon", MRS Symposium Proceedings **870E**, edited by M. S. Shur, P. Wilson, M. Stutzmann, p. H2.2, San Francisco, March 28-April 1 2005.
10. "Power generation in random diode arrays", Diana Shvydka and V. G. Karpov, Phys. Rev. B **71**, pp. 115314-1-5 (2005).
11. "Propagating Electric Impulses in Thin Film PV", T. K. Wilson, Diana Shvydka and V. G. Karpov, Proceedings of IEEE 4th World Conference on Photovoltaic Energy Conversion, Waikoloa, Hawaii May 7-12, 2006 (to be published).
12. "Phenomenological model of CdS based thin film photovoltaics", M. L. C. Cooray and V. G. Karpov, Proceedings of IEEE 4th World Conference on Photovoltaic Energy Conversion, Waikoloa, Hawaii May 7-12, 2006 (to be published).
13. "Piezo-photovoltaic coupling in thin-film CdS/CdTe solar cells", Jennifer Drayton, M. Mitra, and Diana Shvydka, Proceedings of IEEE 4th World Conference on Photovoltaic Energy Conversion, Waikoloa, Hawaii May 7-12, 2006 (to be published).
14. "Pressure dependence of photovoltaic parameters in thin film Cu(In,Ga)Se₂ solar cells", Diana Shvydka, J. Drayton¹, M. Mitra, S.X. Marsillac, F. Jacob, Proceedings of IEEE 4th World Conference on Photovoltaic Energy Conversion, Waikoloa, Hawaii May 7-12, 2006 (to be published).

6.2. Poster or oral presentations published on CDROM and the NREL Web site

1. "Understanding the Physics of CdS-based PV: Band Diagram, Interfaces, and Nonuniformities", V. G. Karpov, D. Shvydka, J. Drayton, M. L. C. Cooray, and A. D. Compaan, DOE Solar Energy Technologies Program Review Meeting, November 7-10, Denver, Colorado, DOE/GO-1020006-2245, March (2006).
2. "Piezo-effect in CdS-based solar cells", Diana Shvydka, Jennifer Drayton, Mukut Mitra, Proceedings of the 19th National CdTe R&D Meeting, Editors: H. S. Ullal, P. V. Meyers, and C. Ferekides, Golden, Colorado, March 9-10 (2006).

3. “Indicative facts and device model”, V. G. Karpov, D. Shvydka, J. Drayton, L. Cooray, and A. D. Compaan, Proceedings of the 19th National CdTe R&D Meeting, Editors: H. S. Ullal. P. V. Meyers, and C. Ferekides, Golden, Colorado, March 9-10 (2006).
4. “Back contact and nonuniformity”, V. G. Karpov, D. Shvydka, J. Drayton, Y. Rousillon, and A. D. Compaan, Proceedings of the 19th National CdTe R&D Meeting, Editors: H. S. Ullal. P. V. Meyers, and C. Ferekides, Golden, Colorado, March 9-10 (2006).
5. “Piezo-effect in CdS/CdTe solar cells”, Diana Shvydka, J. Drayton, V. G. Karpov and A.D. Compaan, National CdTe R&D Team Meeting; Golden, CO; May 5-6, 2005.

7. PROJECT PERSONNEL

7.1. Research professors

Akhlesh Gupta (Ph.D. Indian Institute of Technology, Delhi)(50% time, 9/1/01-9/1/05)

Diana Shvydka (Ph.D., U. of Toledo, 5/2002)(9/02–)

7.2. Postdoctoral Associate

Jennifer Drayton (Ph.D., U. of Toledo, 12/2005)(1/06–)

Xiangxin Liu (Ph.D., U. of Toledo, 5/2006)(5/06–)

7.3. Graduate Students (with Principal Advisor)

(Some students received support from other sources but made significant contributions to this work)

Lilani Cooray (Karpov)

Ph.D. in progress

Mikut Mitra (Karpov)

Ph.D. in progress

Yevgen Kryukov (Karpov)

Ph.D. in progress

Viral Parikh (Compaan)

M.S. and Ph.D. in progress

Victor Plotnikov (Compaan)

M.S. and Ph.D. in progress

Anthony Vasko (Compaan)

Ph.D. in progress

Trevor Wilson (Karpov)

M.S. in progress

7.4. Technical Assistants

Terry Kahle (3/03–)

Robert Burmeister (4/96–) (25% time)